Physics Reports 519 (2012) 51–96

Contents lists available at SciVerse ScienceDirect

Physics Reports

journal homepage: www.elsevier.com/locate/physrep

# Development and trends in synchrotron studies of ancient and historical materials

Loïc Bertrand [a,b,*], Marine Cotte [c,d], Marco Stampanoni [e,f], Mathieu Thoury [a], Federica Marone [e], Sebastian Schöder [b,a]

[a] *IPANEMA, USR 3461 CNRS/MCC, Synchrotron SOLEIL, BP48 Saint-Aubin, F-91192 Gif-sur-Yvette, France*

[b] *Synchrotron SOLEIL, BP48 Saint-Aubin, F-91192 Gif-sur-Yvette, France*

[c] *European Synchrotron Radiation Facility, Polygone Scientifique Louis Néel, 6 rue Jules Horowitz, F-38000 Grenoble, France*

[d] *Centre de Recherche et de Restauration des Musées de France, UMR 171 CNRS, Palais du Louvre, Porte des Lions, 14 Quai François Mitterrand, F-75001 Paris, France*

[e] *Swiss Light Source, Paul Scherrer Institut, CH-5232 Villigen, Switzerland*

[f] *Institute for Biomedical Engineering, University and Eidgenössische Technische Hochschule Zurich, 8092 Zurich, Switzerland*

ARTICLE INFO

*Article history:*
Accepted 2 March 2012
Available online 8 March 2012
editor: J. Eichler

*Keywords:*
Synchrotron
Ancient and historical materials
X-ray spectroscopy
X-ray imaging
Fourier-transform infrared spectroscopy
UV/visible luminescence spectroscopy

ABSTRACT

Synchrotron photon-based methods are increasingly being used for the physico-chemical study of ancient and historical materials (archaeology, palaeontology, conservation sciences, palaeo-environments). In particular, parameters such as the high photon flux, the small source size and the low divergence attained at the synchrotron make it a very efficient source for a range of advanced spectroscopy and imaging techniques, adapted to the heterogeneity and great complexity of the materials under study. The continuous *tunability* of the source — its very extended energy distribution over wide energy domains (meV to keV) with a high intensity — is an essential parameter for techniques based on a very fine tuning of the probing energy to reach high chemical sensitivity such as XANES, EXAFS, STXM, UV/VIS spectrometry, *etc.* The small source size attained (a few micrometres) at least in the vertical plane leads to spatial coherence of the photon beams, giving rise in turn to a series of imaging methods already crucial to the field. This review of the existing literature shows that microfocused hard X-ray spectroscopy (absorption, fluorescence, diffraction), full-field X-ray tomography and infrared spectroscopy are the leading synchrotron techniques in the field, and presents illustrative examples of the study of ancient and historical materials for the various methods. Fast developing analytical modalities in scanning spectroscopy (STXM, macro-XRF scanning) and novel analytical strategies regarding optics, detectors and other instrumental developments are expected to provide major contributions in the years to come. Other energy domains are increasingly being used or considered such as far-infrared and ultraviolet/visible for spectroscopy and imaging. We discuss the main instrumental developments and perspectives, and their impact for the science being made on ancient materials using synchrotron techniques.



* Corresponding author at: IPANEMA, USR 3461 CNRS/MCC, Synchrotron SOLEIL, BP48 Saint-Aubin, F-91192 Gif-sur-Yvette, France.
*E-mail address:* loic.bertrand@synchrotron-soleil.fr (L. Bertrand).
*URL:* http://www.synchrotron-soleil.fr/ipanema (L. Bertrand).

0370-1573/$ – see front matter © 2012 Elsevier B.V. All rights reserved.
doi:10.1016/j.physrep.2012.03.003

**Contents**



## 1. Introduction

The study of the composition, structure, morphology and physico-chemical properties of materials from archaeology, cultural heritage and palaeontology is an essential component of the research in these fields [1–3]. It complements, when available, historical evidence and information retrieved from the geochronological context. Over the past years, progresses in the instrumentation available on site, at the laboratory and at large scale facilities led to considerable improvement in our understanding of these materials. Among them, synchrotron-based techniques are often unique in the brightness attained and the versatility of the source, allowing a very wide range of photon-based spectroscopy and imaging techniques.

Questions such as the understanding of the discolouration of smalt pigments in paint layers using synchrotron infrared and X-ray absorption spectroscopy techniques [4], the long-term alteration of bone materials in archaeological contexts through synchrotron small-angle X-ray scattering techniques [5,6], improvements in the determination of the age at death of hominins through phase-contrast visualisation of incremental features in fossil teeth [7] demonstrate the diversity of

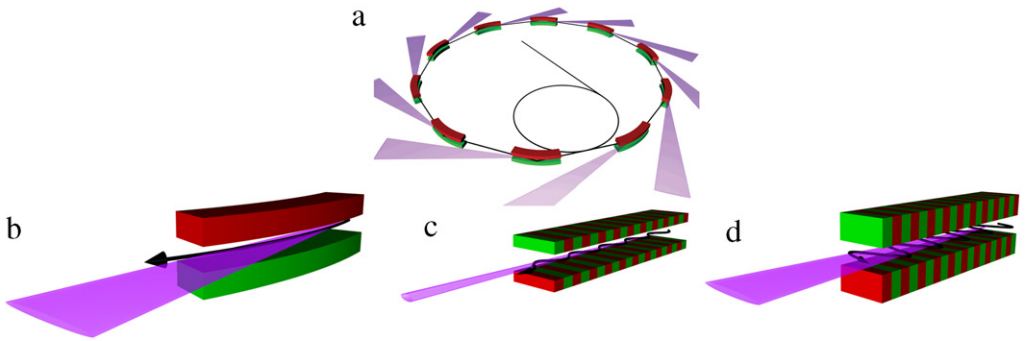


**Fig. 1.** (a) Bunches of electrons are accelerated in a linear accelerator and (in most cases) in a booster synchrotron. The bending magnets are used to steer the electrons and create synchrotron radiation. In third generation synchrotrons three main types of sources exist: (b) bending magnets, (c) undulators ($K < 1$), (d) wigglers ($K > 10$), where $K$ is the deflection parameter defined in Eq. (6).

approaches and questions in the field that benefited from synchrotron investigation in the recent years. The range of synchrotron techniques is very broad and includes hard X-ray, soft X-ray, EUV–VUV, UV/visible, near-, mid- and far-infrared techniques. Although the potentials of the source in the field of ancient and historical materials was identified as soon as the mid 80's [8–11], real developments started mainly from the years 2000 onwards [12–14] with major contributions from a restricted set of expert users of the technique. The field in some respect still lacks the strong collaborative effort that was put in place in some other fields of synchrotron studies such as for structural biology and nano-sciences.

The use of some of the core synchrotron radiation techniques for the characterisation of ancient materials has already been reviewed by several authors, including synchrotron microtomography for palaeontological specimens, synchrotron-based FT-IR and X-ray absorption spectroscopy for cultural heritage [14–19]. However, the present article focuses on the main methodological developments and trends that are central to this field of research. We therefore recall here the physical principles of the most important synchrotron techniques, review the use of synchrotron techniques with examples of application from the open literature and the contribution of the authors in the field, and present adaptations in each of the core techniques to the specific constraints of ancient and historical materials.

Finally, we discuss and question in a full section the prominent trends that may lead to future novel developments in the synchrotron-based study of ancient and historical materials.

## 2. Synchrotron radiation for ancient and historical materials

### 2.1. Generation of synchrotron radiation

When a charged particle is accelerated it emits electromagnetic radiation. The term synchrotron radiation (SR) is usually only used when the acceleration changes the direction and not the absolute speed (as in a magnetic field) while the opposed case of a decelerated charged particle is called *bremsstrahlung*. Synchrotron radiation is emitted by cosmic sources, like the electromagnetic fields around black holes, however, in this context we will only look at the radiation generated in synchrotron facilities.

The special properties of synchrotron radiation (wavelength in the Å regime, small opening cone…) stem from the Lorentz transformation under which an observer in the laboratory reference frame sees the radiation emitted by a relativistic particle. The quantitative properties of the radiation are described by the Liénard–Wiechert potentials

$$V(t) = \frac{e}{4\pi\epsilon_0}\left(\frac{1}{r(t')\,(1-\vec{n}(t')\cdot\vec{\beta}(t'))}\right) \tag{1}$$

$$\vec{A}(t) = \frac{\mu_0\, e}{4\pi}\left(\frac{\vec{\beta}(t')c}{r(t')\,(1-\vec{n}(t')\cdot\vec{\beta}(t'))}\right). \tag{2}$$

In the above equations $V(t)$ and $\vec{A}(t)$ are the scalar and vector potentials, respectively, $r$ is the distance of the particle to the observer, $\vec{n} = \vec{r}/r$ is its unit vector, $\vec{\beta} = \vec{v}/c$ is the normalised velocity of the charged particle. As the speed of the particle is almost as fast as the generated electromagnetic field, the potential observed at the time $t$ does not only depend on the radiation generated by the particle at this time, but also at the previous times $t'$. The full calculation of these potentials can be very lengthy and is beyond the scope of this review. The interested reader is referred to [20]. Instead we will only describe the most important properties of bending magnet (BM) and insertion device (ID) radiation (Fig. 1).

In most 3rd-generation synchrotron sources electrons are used as charged particles. The constant magnetic field of a bending magnet forces the electrons on a circular trajectory. Due to the Lorentz transformation its radiation is emitted

within a small opening angle

$$\Theta \approx \sin \Theta = \frac{1}{\gamma} \tag{3}$$

with the Lorentz factor $\gamma$:

$$\gamma = \frac{1}{\sqrt{1-\beta^2}} = \frac{E}{m_e c^2}. \tag{4}$$

Bending magnets emit a broad spectrum which is peaked at a characteristic frequency that is proportional to the magnetic field and the square of the electron energy. The radiated power $P$ depends on the square of the energy of the electrons $E$ and the magnetic field $B$ of the magnet:

$$P \propto E^2 B^2 y I. \tag{5}$$

$y$ is the path length of the electron during which its irradiation reaches the observer and is typically in the range of one to a few mm. $I$ is the storage ring current. The light emitted by an electron on a circular arc is linearly polarised if the observer is in the plane of the electron movement. When seen from a viewpoint out of the storage ring plane, the projected electron movement appears to be an elliptic arc and its radiation is therefore circularly polarised.

An insertion device is a periodic arrangement of magnets with opposite fields described by the wavelength of the magnetic undulation $\lambda_u$. They are characterised by the constant $K$, which measures the ratio between the deflection angle due to the magnetic structure and the natural opening of the SR cone $1/\gamma$ [21].

$$K = \frac{eB\lambda_u}{2\pi\, m_e\, c}. \tag{6}$$

Insertion devices are classified as wigglers ($K > 10$) and undulators ($K < 1$), Fig. 1. The magnetic field of undulators causes only weak deviations to the electron path, its $K$ value being around 1 or lower. This leads to interference effects between the radiation emitted from different poles. Constructive interference occurs when the wavefront emitted by the electron at one pole is one wavelength ahead of the particle when it reaches the next pole.

The electron speed is almost equal to the speed of light. It is due to the Lorentz contraction that the magnetic structures, which are centimetres in size, emit radiation in the X-ray regime. The fundamental wavelength of an undulator is [21]

$$\lambda_F(\theta) \approx \frac{\lambda_u}{2\gamma^2}\left(1 + \frac{K^2}{2} + (\gamma\theta)^2\right) \tag{7}$$

with the observation angle $\theta$. The spectral distribution around the fundamental wavelength and the harmonics becomes sharper with increasing number of periods $N$.

Wigglers have high magnetic fields that cause strong deviations to the electron path, their $K$ value is high. Due to the large deviation there is only a weak interference between the radiation emitted from different magnet poles. Their spectrum and radiated power are therefore similar to that of a bending magnet. However, the full length of the wiggler (which is typically around 1–2 metres) contributes to the radiation, leading to very high intensity emitted into a broad horizontal fan.

An important property of radiation sources is the *brightness*. It is defined as the number of photons that are emitted by one square mm of the source per second per solid angle and per 0.1% bandwidth. The brightness is a good measure how much "usable" radiation is created for typical synchrotron experiments. Most third generation synchrotron beamlines use undulators because the brightness is greater. However, applications that need raw intensity over a broad energy range favour wigglers.

In most synchrotron sources the electrons are pre-accelerated in linear accelerators and booster synchrotrons before they are injected into the storage ring. Due to collisions with gas molecules and other events the ring current decreases steadily and needs to be refilled a few times per day. Variations in the ring current lead to changes in the heat load of the X-ray optics that reduce the stability of the beam. For this reason modern synchrotrons use so called top-up mode, in which electrons are injected into the ring in very short time intervals.

In most cases the electrons in the storage ring are organised into *bunches*. This leads to a time structure of the synchrotron radiation in the picosecond regime. Most synchrotron experiments integrate over these bunches, which leads to a constant X-ray intensity. However, time resolved *pump and probe* experiments make use of this time structure to observe dynamics in the picosecond timescale.

### 2.2. Main specificities of ancient and historical materials in view of their synchrotron-based study

The main specificities of synchrotron radiation for the analysis of ancient materials are summarised in Fig. 2.

Ancient and historical materials are highly heterogeneous and/or composite, and their study requires working at the relevant length scales, using complementary analytical means and combining information coming from several methods. The composition and the properties of the assemblies under consideration are particularly complex: minerals, organic compounds, and weathering/interaction products are intermixed. In cases as distinct as the surface of a corroded metal

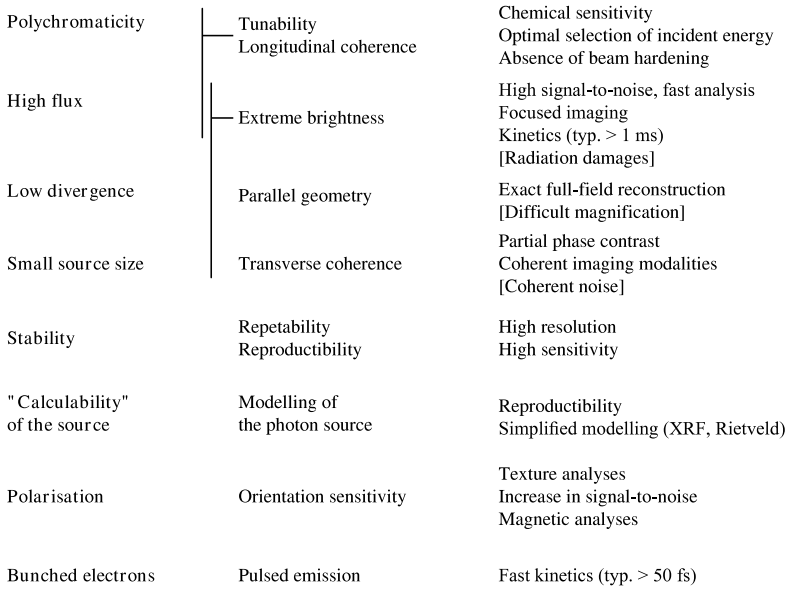


**Fig. 2.** Main properties of synchrotron radiation of interest for ancient and historical materials studies: basic properties of the source (left), beam characteristics (middle), instrumental characteristics (right). Instrumental characteristics between [brackets] highlight the possible drawbacks of synchrotron radiation techniques for ancient materials.

object or the pictorial layers of an easel painting, heterogeneity can be present over more than 7 orders of magnitude from the nanometre to the centimetre (Fig. 3). In this context, heterogeneity can concern elemental distribution, oxidation degree and nature of coordination spheres, structural defects, grain sizes, interfacial organisation, polymerisation degree, texture (i.e. specific orientation), etc. Most often, the information looked after will come from *deviation from the standard composition or behaviour* of the material. For this reason, in the following, we will deliberately not be too specific in the correlation between categories of materials and the choice of characterisation methods, as the information researched will frequently come from singularities, or *traces* in a general sense, which properties might significantly differ from that of the bulk material.

As for environmental or Earth science materials, collection of chemical, structural and morphological statistically-relevant information at the various length scales is a challenging yet essential prerequisite. Ancient and historical materials are systems particularly difficult to model or reproduce. Therefore, a naturalistic approach is usually favoured to analyse them *as is*. The strategies differ greatly from those adopted in most fields of research where the properties of model materials can partly be optimised inline with the measurement and characterisation process. Methods such as synchrotron X-ray, ultraviolet (UV)–visible (VIS) and infrared (IR) spectro-microscopy and imaging methods are particularly suited to these studies by allowing for the coupling of elemental, molecular and structural information. Working at a sufficiently high spatial resolution can often allow for a simpler interpretation of the data by leading to less complex mixtures within individual spots analysed. In addition, spectro-imaging will provide useful information on the correlation between compounds by bridging spatial and spectral levels of information.

The properties out of equilibrium of these materials are of major interest. Dynamic processes are very important in archaeology and palaeontology for both fundamental aspects (understanding of weathering processes/corrosion), and their consequences (differential degradation leading to possible palaeo-environmental interpretation, i.e. taphonomic biases, conservation measures, etc.). The alteration of artefacts and specimens can be particularly accelerated by the removal of the object from their depositional contexts of origin, which leads both to specific research on these processes and the need for specific care for sample collection, preparation, handling and storage. In conservation sciences, the effectiveness of stabilisation, conservation and restoration measures can be optimised by undertaking material characterisation under dynamic solicitation. This requires a detailed description of systems for which the physico-chemical history is sometimes very poorly known. *In-beam* dynamic monitoring was also occasionally used to track the changes occurring during the accelerated ageing of a material under a given solicitation.

Ancient and historical objects often take their full historical meaning when considered within corpuses/collections of objects, and compared to modern referentials or with materials which ageing has been simulated. The latter is not a straightforward process. Definition of ageing protocols as well as comparison between old materials and artificially-aged ones is usually difficult. The analytical techniques and synchrotron analytical modalities have to be optimised to take into account the need to work on corpuses rather than on isolated objects. This tends to require a statistical approach of the objects under study.

Some objects may require specific handling and storage conditions, or *non-invasive* examination. Most synchrotron techniques are regarded as *non-destructive* as the sample under study can usually be reanalysed using complementary

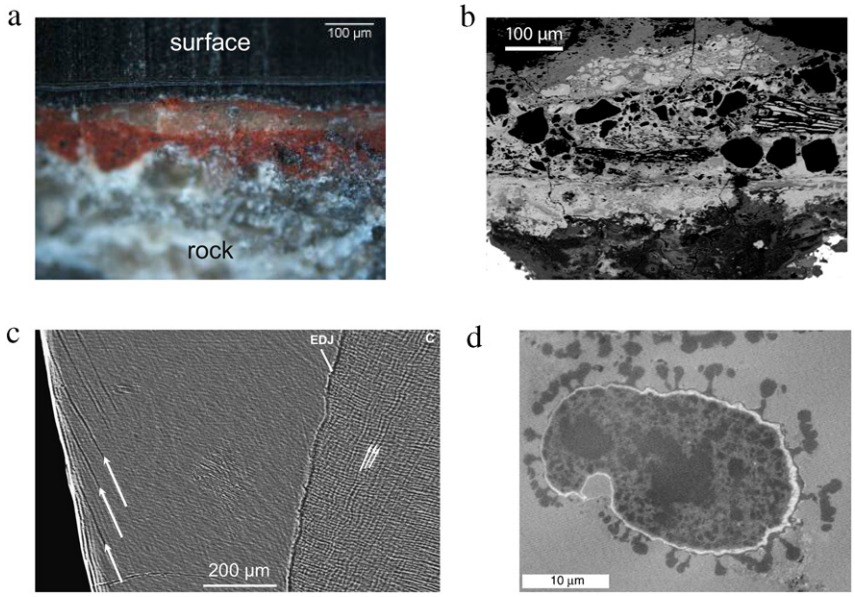


**Fig. 3.** Stratigraphy from (a) a rock art paint cross-section (image courtesy: St. Hoerlé), (b) a corroded mediaeval nail [22], (c) the enamel–dentine junction of a tooth, showing in particular incremental features [7], (d) a partly diagenetised model spore studied using STXM [23]. The heterogeneity length scale in these materials extends from nanometric to macroscopic scales.

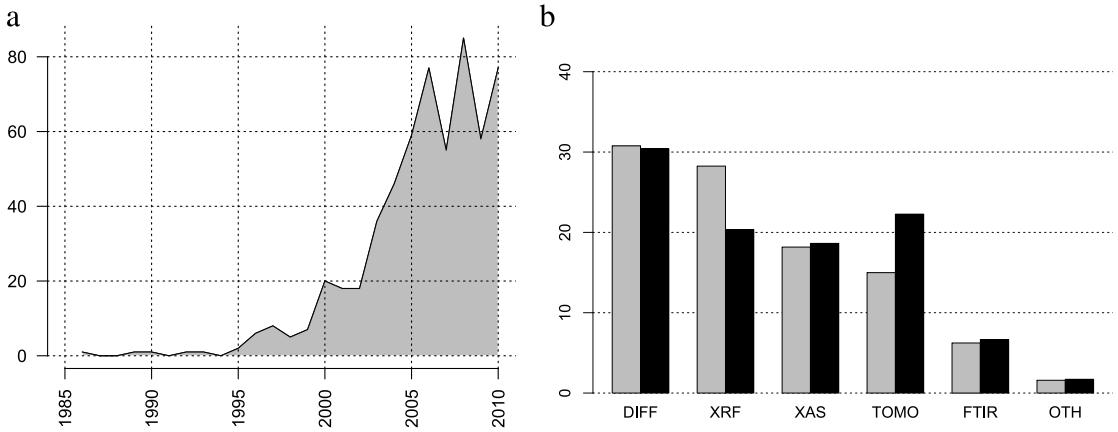


**Fig. 4.** (a) Evolution of the number of publications using synchrotron radiation for ancient and historical materials known to the authors in the timeframe 1986–2010. (b) Share in % of each method respectively in the 1986–2010 (*grey*) and in the 2005–2010 period (*black*). DIFF: XRD and SAXS, XRF: X-ray fluorescence, XAS: X-ray absorption, TOMO: X-ray µCT and laminography, FT-IR: Fourier-transform infrared microspectroscopy, OTH: STXM, X-PEEM and XPS, UV/visible spectroscopy.

analysis techniques after the synchrotron experiment (see Sections 5.8 and 5.5). However, a large part of synchrotron techniques from the infrared to hard X-rays in the few tens of keV range may require sampling and are therefore *invasive*. The development of specific non-invasive synchrotron methods is important in this context as they can provide additional information on larger areas of the object under study, i.e. leading to more statistically relevant information, on sectors that may not be sampled, and can also be used to refine the area where sampling should be performed.

An overview of the literature published in the field, and more particularly in cultural heritage and archaeology, is respectively reported in [24] and [13]. Main figures are represented in Fig. 4. 582 publications are known to the authors in the field in the 1986–2010 period (614 by including referenced publications for year 2011). It is particularly noticeable that 50% of these publications are less than 5 year old.

A list of common synchrotron methods with acronyms used in this text is presented in Table 1. Fig. 7 schematically represents the setups used for the main synchrotron characterisation techniques.

**Table 1**
List of synchrotron techniques with common acronyms. Techniques discussed in this review are marked by a *. Main techniques used thus far in the fields of cultural heritage and archaeology are denoted **.

| Energy range | Techniques |
|---|---|
| Infrared (IR) | Fourier-transform far infrared spectroscopy*<br>Fourier-transform infrared micro-spectroscopy (FT-IR)**, Fourier-transform infrared micro-imaging*<br>Near-infrared micro-spectroscopy (NIR) |
| Ultraviolet (UV) – visible (VIS) | Synchrotron UV/VIS luminescence micro-spectroscopy (UV-LMS)*<br>Synchrotron UV/VIS luminescence full-field spectro-microscopy (UV-LFS)*<br>Synchrotron radiation circular dichroism (SRCD) |
| X-rays | Scanning transmission X-ray microscopy (STXM)*<br>Transmission X-ray microscopy (TXM)<br>X-ray photoemission electron microscopy (XPEEM)<br>X-ray photoelectron spectroscopy (XPS),<br>Angle-resolved photoelectron spectroscopy (ARPES)<br>Auger electron spectroscopy (AES)<br>X-ray magnetic circular dichroism (XMCD), X-ray magnetic linear dichroism (XMLD)<br>X-ray fluorescence spectroscopy (XRF)**, confocal XRF (C-XRF)*, macro-scanning XRF (MA-XRF)*<br>X-ray absorption near-edge spectroscopy (XANES)**, Extended X-ray absorption fine structure spectroscopy (EXAFS)*<br>X-ray diffraction (XRD)**, Small-angle X-ray scattering (SAXS)*, Multiwavelength anomalous dispersion (MAD), Diffraction anomalous fine structure (DAFS), Grazing-incidence small angle X-ray scattering (GISAXS),<br>White-beam microdiffraction<br>Coherent diffraction imaging*, Ptychography*<br>Resonant inelastic X-ray scattering (RIXS)<br>X-ray topography (XRT)<br>X-ray reflectivity<br>X-ray radiography (XRR), (Phase-contrast) X-ray microcomputed-tomography ($\mu$CT)**, Diffraction enhanced imaging (DEI), *K*-edge subtraction imaging*, Laminography* |

### *2.3. Synchrotron micro-spectroscopy, mapping and imaging*

Following the clear distinction by Salzer and Siesler [25], we will generalise here to the whole spectral range the distinction between *mapping* (or *raster-scanning*) i.e. the sequential measurement of spectra from adjacent regions of a sample achieved by moving each region into the photon beam, and (full-field) *imaging* (or *microscopy*) where an image of the sample is focused onto an array detector where the signal coming from each region of the sample is measured at each pixel. In addition to the mapping and imaging approaches, a hybrid approach is also available where an array detector is used to raster-scan a sample and obtained data can be stitched together during processing.

Cultural heritage and archaeology scientific communities mostly exploit the micro-focused spectroscopy capabilities, while maintaining a reasonably low beam divergence, of synchrotron beamlines [14]. This is either used for precise spot analyses or in raster-scanning mode to map areas of samples (Fig. 5). Scanned spots can also be non contiguous, when one wants to map large objects for instance using *sub-sampled* fast XRF macro-scanning of paintings or flat fossils (see *infra*, Section 3.2.4). Full-field X-ray imaging techniques have only been scarcely used for archaeology and conservation research. On the contrary, in palaeontology, the use of synchrotron techniques has been very primarily restricted to full-field X-ray imaging (micro-computed tomography) now mostly performed in phase-contrast mode.

As the optical index *n* of most materials is close to unity in the X-ray range, focusing X-rays is challenging. However, there are today several types of optics used to focus X-ray beams (Fig. 6). Reflective optics are achromatic, which allows them to focus white beams and deliver a stable spot even when changing the energy of the incoming X-ray beam. They are therefore very suited to X-ray absorption experiments. They are capillaries or bent mirrors that consist of a substrate covered with a thin layer of a high-*Z* material. Some of them have a fixed bending, while others use mechanical benders to change the focal spot size or distance. The most common configuration used for focusing is the *Kirkpatrick-Baez* system, in which one mirror focuses the beam in the horizontal and a second mirror focuses in the vertical direction. Both mirrors can be moved and bent independently of each other, giving the system a lot of flexibility.

Diffractive optics use nanostructures to focus the beam. They are called Fresnel lenses and are very effective for low energies. This type of optics is chromatic, their focal points will move with the energy, therefore requiring adjustments when scanning the energy range (e.g. for STXM experiments). In addition, by using nanostructures of different patterns the shape of the beam can be determined, which makes square or double beams possible. At high X-ray energies it becomes increasingly difficult to manufacture nanostructures that provide the necessary phase shift for effective focusing.

Refractive optics work similar to lenses for visible light. As the index of refraction of X-rays in matter is smaller than one (the phase velocity is higher than the vacuum speed of light) they look like inverted lenses. Since the index of refraction is very close to unity many lenses are needed (often between ten and 100 of lenses are used) to provide sufficient refraction power. Most lenses are made out of beryllium, but many different materials are used. The main disadvantage of refractive

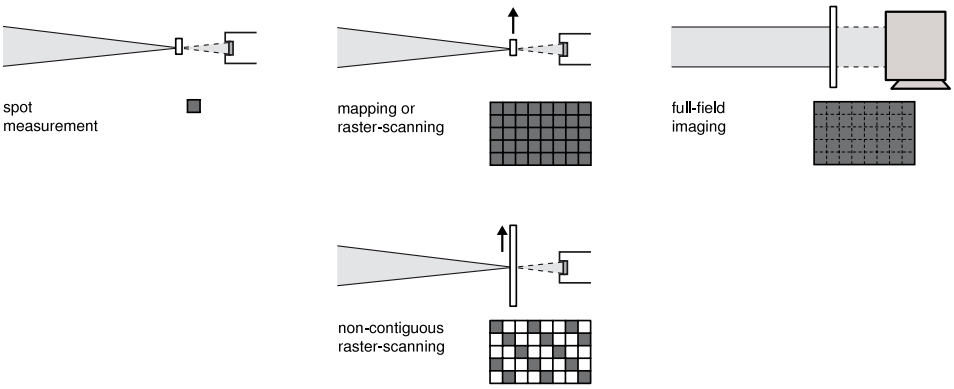


**Fig. 5.** Main data collection modalities discussed in the present review: spot measurement, mapping or raster-scanning, non-contiguous raster-scanning and full-field imaging. Non-contiguous raster-scanning is used for instance for the fast XRF macro-scanning of large objects by using a spot size smaller than the scanning step size.

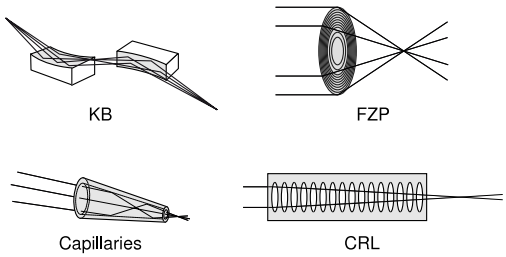


**Fig. 6.** Main X-ray focusing optics in use at synchrotron facilities. KB: Kirkpatrick–Baez elliptically-bent double-focusing mirrors [26], FZP: Fresnel zone plates [27], CRL: Compound refractive lenses [28,29], Mono and poly-capillaries [30]. KB systems and capillary optics are achromatic reflective optics therefore more suited to focus X-rays on wide energy ranges.

**Table 2**
Main synchrotron methods used to study ancient and historical materials, physical origin and level of information obtained.

| Physical origin | Core shell electronic levels | Bond vibration and rotation modes | Outer shell electronic levels | Crystalline order, mesoscopic organisation | Density and compositional contrast |
|---|---|---|---|---|---|
| Main information provided | Elemental composition | Coordination sphere, Molecular organisation/signature | Coordination sphere, Molecular organisation/signature, Structural defects, Impurities | Grain, texture, Mesoscopic organisation, Porosity | Morphology, Porosity |
| Common methods | XRF | FT-IR | XAS, XRD | XRD | μCT |
| Secondary methods | | UV/VIS | UV/VIS | SAXS | Laminography |

lenses is the low flux that they provide at low energies due to the absorption of the beam when transmitted through the optics, but they become more efficient at high energies.

Experimental setups for full-field imaging use optics to optimise the field of view and the coherence properties of the beam for the experiment. In general, optical elements will be kept at a minimum as defects, in particular slope errors, will introduce fluctuations in the beam intensity at the object position and degrade the quality of the wavefront, which reduce the image quality and may hamper quantitative results to be obtained.

## 3. Synchrotron X-ray techniques

Main processes of interaction between photon and matter and their analytical interest in the study of ancient and historical materials are summarised in Fig. 8 and in Table 2. For tabulated X-ray data, the reader is invited to turn towards more specialised reading [31]. The Center for X-ray optics at LBNL also produces a very convenient *X-ray data booklet* with most of its data available online at the CXRO website [32].

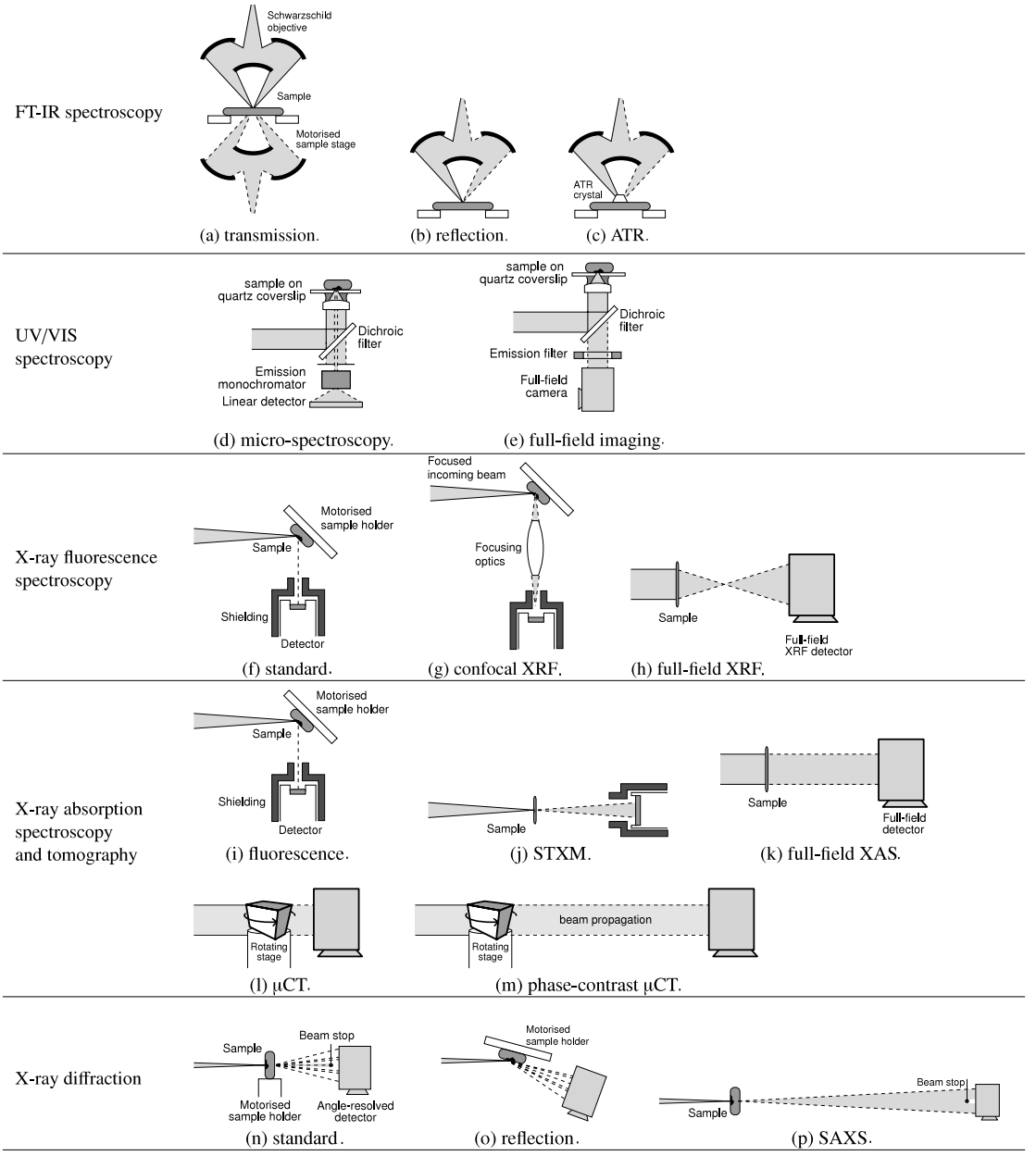


**Fig. 7.** Schematic representation of the main experimental methods used to study ancient materials discussed in this paper.

### *3.1. Basics of X-ray interaction with matter*

For energies $E$ in the 30 eV–100 keV range, typically encountered at SR facilities, the total photon interaction cross-section $\sigma(Z, E)$ corresponding to all processes between photons and an atom of atomic number $Z$ can be expressed as:

$$\sigma(Z, E) = \sigma_{pe}(Z, E) + \sigma_{coh}(Z, E) + \sigma_{incoh}(Z, E) \tag{8}$$

where $\sigma_{pe}(Z, E)$ is the photo-excitation cross-section, $\sigma_{coh}(Z, E)$ the coherent (Rayleigh) scattering cross-section and $\sigma_{incoh}(Z, E)$ the incoherent (Compton) scattering cross-section. Additional processes, such as nuclear electron/positron pair production and photonuclear absorption occur with a far lower probability.

For energies below 100 keV, photo-excitation mostly predominates (Fig. 9a), a process in which inner shell electrons transit to unoccupied electronic states or to the *continuum* (ionisation). When neglecting the effect of local environment (see *supra*, X-ray absorption spectroscopy), atomic contributions can be linearly summed. The decrease in intensity of an X-ray monochromatic beam through a thickness $\delta z$ of material of linear attenuation coefficient $\mu_l(Z, E)$, or mass attenuation

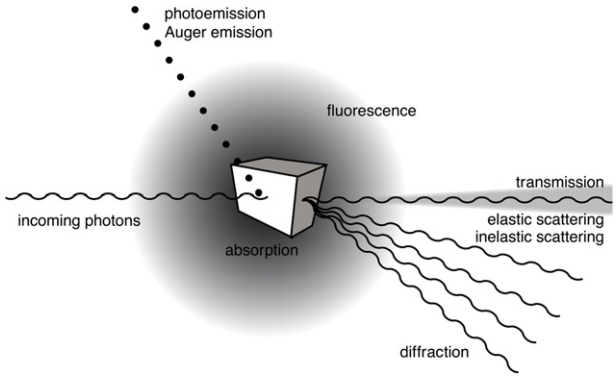


**Fig. 8.** Schematic representation of the main interaction processes involved in photon interaction with matter.

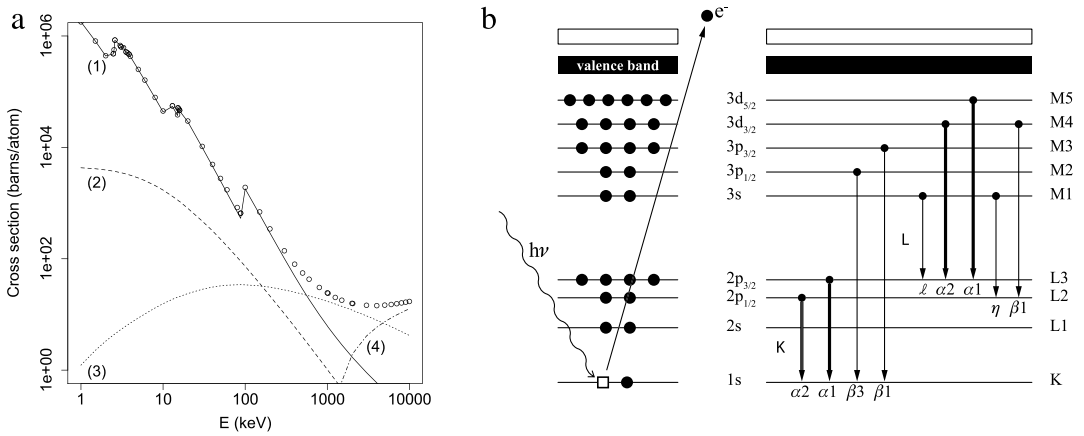


**Fig. 9.** (a) Photon cross-section as a function of energy, showing the contribution of the main processes: (1) atomic photoabsorption, (2) coherent scattering, (3) incoherent scattering, (4) nuclear pair production, (*points*) experimental data. Element: Pb, data: Xcom database, NIST [33]. (b) Schematic representation of the photo-excitation process and subsequent allowed X-ray fluorescence transitions. Main emission lines are shown in bold.

coefficient $\mu(Z, E) = \mu_l(Z, E)/\rho$, is then provided by the Beer–Lambert's law:

$$I(\delta z, Z, E) = I_0(E)\ \exp(-\mu_l(Z, E).\delta z) \tag{9}$$

$$I(Z, E) = I_0(E)\ \exp\left(-\int \mu_l(Z, E)\,\mathrm{d}z\right) \tag{10}$$

with $I_0$ and $I(\delta z)$ respectively the beam intensities before and after crossing the material. When refraction effects can be neglected, photo-excitation predominates and $\mu_l(Z, E)/\rho$ writes:

$$\frac{\mu_l(Z, E)}{\rho} = \frac{N_A}{A_M}\sigma(Z, E) \approx \frac{N_A}{A_M}\sigma_{pe}(Z, E) \tag{11}$$

with $N_A$ Avogadro's number, $\rho$ the material density and $A_M$ the atomic weight. At energies distant from absorption edges of atoms constituting the material, the linear attenuation coefficient decreases slowly with energy according to a Victoreen function:

$$\mu_l(Z, E) \approx \frac{A}{E^3} + \frac{B}{E^4} \tag{12}$$

which is primarily governed by a term proportional to $Z^4/E^3$. The ejected electron (or *photoelectron*) bears a kinetic energy equal to $E - E_0$ or a wave vector $k = \sqrt{2m_e.(E - E_0)/\hbar^2}$, where $E_0$ is the ionisation energy, $m_e$ the electron mass and $\hbar$ the reduced Planck constant. The photoelectron can be analysed either directly or by indirect phenomena due to the relaxation of the atom to its ground state may be used to probe material properties. Atomic relaxation involves transitions from outer shells, in turn compensated by radiative or non-radiative (Auger and Coster–Kronig) events. For K-shell vacancies, radiative effects predominate only for $Z > 30$.

Below 50–100 keV, elastic scattering cross-sections generally have far lower values than those of photo-excitation. However, in the beam forward direction or when scattered beams interfere constructively (diffraction), the resulting signal

leads to key analytical methods such as small-angle X-ray scattering (SAXS) and X-ray diffraction (XRD). Elastic scattering occurs when photons interact with electrons without changing their wavelength. In the classical picture this is due to an oscillation of the electron in the field of the photon. The electron emits a wave of the same wavelength, but scattered in a different direction.

Diffraction occurs when a wave is transmitted or reflected from a structure that has a similar periodicity as its wavelength. X-rays, having a wavelength in the Å regime, are diffracted by interatomic distances. X-ray diffraction patterns are therefore a powerful tool to explore the average structure of matter on atomic and molecular length scales. For a 3-dimensional periodic structure, like a single crystal, the pattern obtained is a network of spots that indicates the interatomic distances. Analysis of the symmetries of the diffraction pattern as well as the position of the diffraction spots for many different angles of incidence of the X-ray beam allows a complete reconstruction of the crystal structure. X-ray diffraction will be described in some detail in Section 3.4.

At high energies the inelastic Compton scattering (curve 3 in Fig. 9a) becomes an significant process. The photon transfers part of its energy to an electron thus creating a fast electron and a scattered photon with a longer wavelength. The amount of energy transferred depends on the photon energy and the scattering angle [21]

$$\frac{E_i}{E_s} = 1 + \lambda_C\, k\,(1 - \cos\psi)\,. \tag{13}$$

$E_i$ and $E_s$ are the energies of the incident and the scattered photon, respectively, $k$ is the wave vector of the incident photon, $\psi$ is the scattering angle and $\lambda_C$ is the *Compton scattering length*

$$\lambda_C = \frac{\hbar}{m_e c} \simeq 3.86 \cdot 10^{-3}\ \text{Å}, \tag{14}$$

with the speed of light in vacuum $c$.

At photon energies greater than $2 \cdot m_e \simeq 1022$ keV, the nuclear pair production process is activated (curve 4 in Fig. 9a), in which one photon creates an electron–positron pair. However, such energies are not commonly used for material experiments at SR facilities.

The calculated mean free paths of photons in a few reference materials are plotted on Fig. 10. The analytical limit is imposed here by the probability for fluoresced photons to escape the material and be detected. The thickness that can be probed when studying elements in light organic matrices typically lies in the few millimetre range, and falls down to tens of μm in metal matrices.

### 3.2. X-ray fluorescence spectroscopy and related techniques

#### 3.2.1. Basic principles

X-ray fluorescence results from the photoexcitation of an atom by ejection of an electron from an inner shell. The energy of the characteristic fluoresced photons, associated to the transition of an electron from a higher energy initial level $i$ to a less energetic final one $f$, is:

$$E = E_i - E_f = h\nu = \frac{hc}{\lambda}. \tag{15}$$

Elemental composition can then be identified from the integration of the peak area $A$ of these characteristic lines. Indeed, the relation between $A^i_{j,k}$ and the mass concentration $C_i$ of element $i$ can be approximated by [35, chap. 7]:

$$A^i_{j,k} = I(E_0) \cdot C^i \cdot \frac{\sigma^i_{pe,j}(E_0)}{M}\, F^i_{j,k} \left[1 - \exp\left(-M \frac{\rho\, z}{\sin\alpha}\right)\right] \epsilon^i_{j,k} \tag{16}$$

where $I(E_0)$ is the incident flux, $\sigma^i_{pe,j}$ the photoelectric absorption coefficient of element $i$ in shell $j$, $F^i_{j,k}$ the probability that an ionisation in shell $j$ leads to the emission of line $k$ at the energy $E^i_{j,k}$, $\rho$ the density, $\alpha$ the incident angle of the primary beam and of the outgoing fluorescence photon on the sample assumed here to be equal, $z$ the sample thickness, and $\epsilon^i_{j,k}$ the detector efficiency et energy $E^i_{j,k}$. $M = \mu(E_0) + \mu(E^i_{j,k})$, where $\mu(E0)$ and $\mu(E^i_{j,k})$ are the mass absorption coefficients of the matrix at energy $E_0$ and $E^i_{j,k}$, respectively.

The probability to detect the fluoresced photon therefore primarily depends on that of the photon to be reabsorbed (spatial distribution of the elements constituting the matrix, atmosphere), the geometry (detection solid-angle, angle at which the detector is positioned), the efficiency of the detector and of the potential optical elements (such as capillary optics for confocal-XRF) in detection. Quantitative determination of the elemental composition can be obtained, usually based on an iterative refinement process starting from an *a priori* model of the distribution of the elemental composition (homogeneous sample, layered sample, inclusion…).

Although XRF is a very powerful mean to obtain elemental composition, as it is primarily non-destructive (in contrast to ablation-based techniques) and sensitive to sub-surface (i.e. not too much influenced by the surface roughness nor surface

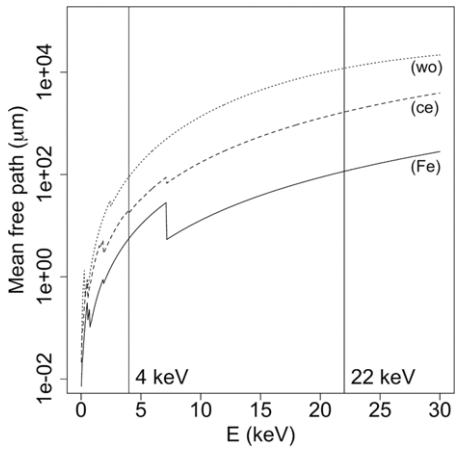


**Fig. 10.** Calculated photon mean free paths in reference materials: (Fe) pure iron, (ce) ceramic based on the composition by [34], assuming a density of 2.0 and that loss-on-ignition material is calcite, (wo) wool. This graph highlights the fact that hard X-ray photons can typically escape from an *information depth* of 5–100 μm in transition metals and 100 μm–10 mm in organic materials. Lines at 4 and 22 keV represent the typical boundaries between soft, hard and very hard X-ray synchrotron beamlines, mainly due to optical constraints on monochromators and mirrors.

contamination), several issues may hamper this process. (1) Some elements (H, He) have no characteristic fluorescence lines and, in standard analytical conditions, emission lines from low-$Z$ elements are too strongly reabsorbed by the surrounding atmosphere to be measured – typically below 1 keV (Na $K_\alpha$) in primary vacuum or He-atmosphere, below 4 keV (Ca $K_\alpha$) in air; (2) solving the inverse problem in order to determine the sample composition may be difficult or impossible, particularly in the case of heterogeneous and complicated geometry's as often encountered in ancient materials; (3) overlaps between some emission lines may make identification and/or quantification of some elements difficult; strategies such as wavelength-dispersive spectroscopy (see Section 3.2.3) can alleviate the latter difficulty, (4) secondary fluorescence effects can be difficult to take into account.

### *3.2.2. Confocal X-ray fluorescence spectroscopy*

Confocal XRF measurements can be carried out by focusing the impinging beam on the sample (generally using KB or capillary optics) and by collecting from a restricted solid angle (generally by putting a capillary in front of the detector). Even by maintaining a constant excitation energy for the incoming beam, as the detection chain results chromatic, the probed volume will vary as a function of the detected energy and must therefore be calibrated, for instance by measuring the signal coming from several $<10$ μm thin metal foils [3,36].

Recent examples include the study of slag inclusions coming from mediaeval metallurgical processes. By studying selected inclusions entrapped in the metal, which composition remains stable during the whole metallurgical process and are not significantly contaminated by the lining or the charcoal during the bloomery process, the trace elemental composition of such inclusions was shown to be conserved from the original ore, to the slags and semi-products (such as iron bars) and finally to the archaeological objects, i.e. all along the *operating chain*. This provided additional clues to stylistic information to confirm the provenance of Milanese- and Brescian-type armours [37]. On the biggest inclusions, measurements could also be performed by ablating inclusions and measuring their elemental composition by Laser ablation-Inductively coupled plasma-Mass spectrometry (LA-ICP-MS) after confocal SR-XRF measurements. The correlation observed between the two sets of data is very satisfactory and highlights the potentials of the technique (Fig. 11).

### *3.2.3. Synchrotron wavelength dispersive X-ray spectrometry*

The measurement of fluorescence spectra on X-ray microscopy beamlines is usually carried out using solid-state energy dispersive detectors. Their attainable energy resolution is in the range of 120–180 eV, which is sometimes insufficient to separate emission lines of distinct elements. The problem of line overlapping is quite frequent when studying artistic materials, since these materials are usually made of complex mixtures, containing both low- and high-$Z$ elements. Typical examples of emission overlap, and consequently complicated elemental identification, are found in paintings and glasses (Pb $M$-lines with S $K$-lines, Ba $L$-lines with Ti $K$-lines, Ca $K$-lines with Sn and Sb $L$-lines…).

To improve the energy resolution, a wavelength dispersive X-ray (WDX) spectrometer system was recently developed at the ID21 beamline of the ESRF (Fig. 12) [39]. It is based on a polycapillary optical element placed at a distance of a few millimetres from the sample, which collects the divergent XRF light emitted from the sample and converts it into a quasi-parallel beam. The beam is then directed onto the flat crystal at the required Bragg $\theta$ angle. X-rays are diffracted by the crystal and counted by a gas-flow proportional counter placed at $2\theta$ angle. The energy resolutions achieved are in the range of 5–30 eV, and can go down to less than 2 eV using a second crystal. This set-up has already been successfully used for the study of lead antimonate crystals in Egyptian, Roman and Nevers glasses [38]. More generally, the potential of

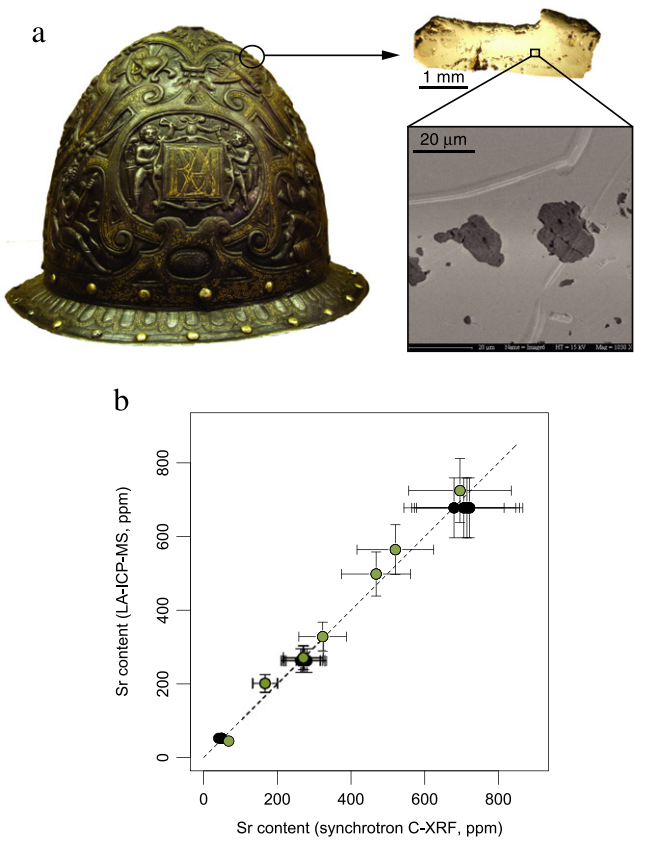


**Fig. 11.** (a) Archaeological morion from an Italian-style armour, described to be originating from *Milan or Brescia about 1600–1610* (Wallace Collection, London, inv. A144), sample taken on the morion and fayalitic-type slag inclusions trapped in the metallic matrix. (b) Comparison between the strontium contents (in ppm) measured using LA-ICP-MS and synchrotron confocal µXRF in selected slag inclusions from mediaeval archaeological iron objects (*green* dots) and reference samples (*black* dots). Error bars show the confidence interval associated to each method (LA-ICP-MS: 12%, µXRF: 20%). Synchrotron µXRF data were collected at the FLUO beamline (ANKA, Karlsruhe). Data courtesy St. Leroy [37]. (For interpretation of the references to colour in this figure legend, the reader is referred to the web version of this article.)

such system for the study of cultural heritage objects and in particular for µXANES analyses (Fig. 12) is discussed in detail elsewhere [40].

### 3.2.4. *Fast X-ray fluorescence macro-scanning and full-field X-ray fluorescence imaging*

The flux attainable at synchrotron sources allows for very fast measurements. However, when collecting very large datasets, the readout time may be a very constraining practical limitation. The development of detectors with very fast readout and high solid-angle of detection such as the Maia [41] detector allows for the fast collection of raster-scanned spectroscopy datasets that can today typically be made of millions of pixels. This approach has thus far been used on two types of objects: paintings [42,43] where elemental composition can be a way to determine the composition of paints over the full area of a canvas and fossils [44], complementing measurements that can be performed using laboratory equipments [45].

Recently, full-field methods to image the fluorescence of small objects were reported. In particular, a method was developed by coupling a *camera oscura* setup, or alternative capillary-based setups, and a pnCCD detector with a spatial resolution of 50 µm over an imaging area of $12.7 \times 12.7$ mm$^2$ and sensitive to photons in the energy range 3–40 keV, with a typical energy resolution better than 152 eV at the Mn $K_\alpha$-line [46]. This requires X-ray area energy-resolved detectors, which is currently an area of intense development.

## 3.3. *X-ray absorption spectroscopy and related techniques*

### 3.3.1. *Basic principles*

A very simplified description of X-ray absorption can be drawn from a particle model [47,48]. The photoelectron generated during photo-excitation (Fig. 9b) is successively scattered by one or more neighbours (*scatterers*) of the absorber. Interferences between the scattered waves lead to modulations of the absorber charge density distribution. This induces

(a)

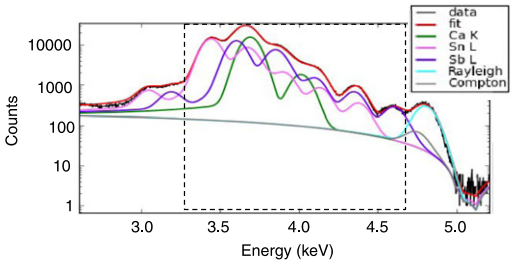


(b) Synchrotron EDX.

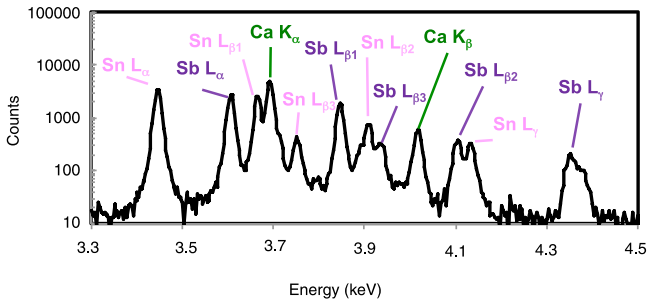


(c) Synchrotron WDX.

**Fig. 12.** WDS versus EDS XRF analysis of opaque coloured archaeological glasses. (a) Shard of the 18th Egyptian Dynasty (inventory number AF12707, credits: C2RMF/D. Vigears), from Lahlil et al. [38]. The opacity and colour of such glasses are usually obtained by an mastered introduction of Sn and Sb-based ingredients in a glass matrix (containing Ca). The spectral resolution of EDS detectors (about 150 eV) is not enough to separate the different emission lines of Ca, Sb and Sn (b). Using a high resolution WDS system (energy resolution of ≈10 eV with a Ge(220) crystal), Ca *K*-lines and Sb and Sn *L*-lines are clearly resolved and identified (c). This resolution can be further exploited for XANES analyses. The setup was implemented at beamline ID21 at the ESRF.

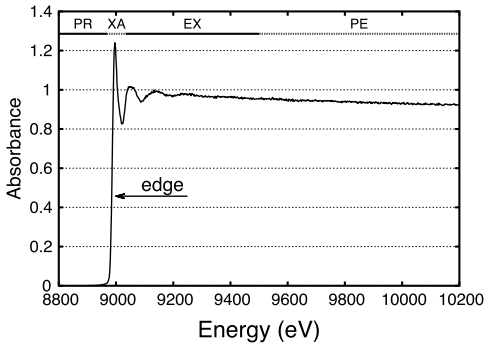


**Fig. 13.** Typical copper *K*-edge EXAFS spectrum showing the pre-edge (PR), XANES (XA), EXAFS (EX) and post-edge (PE) regions. Due to the various atomic environments found in ancient materials, the interpretable XAS signal is usually limited to a small number of interpretable oscillations in heterogeneous ancient materials.

variations in the absorption of the incident wave as a function of the incident beam energy $E$ as provided by the Fermi golden rule, where the modulation of the absorption signal is governed by the final state $|f\rangle$:

$$\mu_l = 4\pi^2\, n \frac{e^2}{\hbar c} \sum_i |\langle i|\vec{E}.\vec{r}|f\rangle|^2\, \delta(E_i + \hbar\omega - E_f). \tag{17}$$

Using a scattering formalism, one can consider that the final state $|f\rangle$ results from all possible paths of the photoelectron. Individual paths start from the absorber, through successive *scatterers* and return to the absorber, and are grouped into equivalent *shells*. The absorption spectrum as a function of $E$ reveals successive characteristic features (Fig. 13) when scanning an edge at an energy $E_0$:

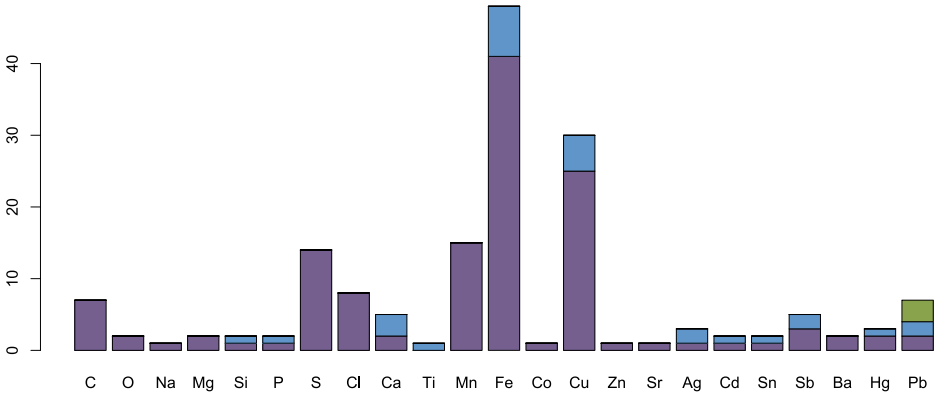


**Fig. 14.** $K$ — (*purple*), $L$ — (*blue*) and $M$ — (*green*) edges studied on ancient materials using X-ray absorption methods (XAS, STXM, X-PEEM and $K$-edge subtraction imaging), in the literature known to the authors in the 1986–2010 period. (For interpretation of the references to colour in this figure legend, the reader is referred to the web version of this article.)

(1) For $E$ close to $E_0$, the excited electron can populate free unoccupied states within the gap or the conduction band. Such transitions are governed by the respective symmetries of the initial and final states (Laporte selection rules). The precise value of the edge energy is usually indicative of the oxidation state of the absorber, and an increase of the oxidation degree of $\pm$I generally corresponds to a shift of 1–2 eV in $E_0$.

(2) Higher above $E_0$, the atom is ionised and the photoelectron is ejected to the continuum (ionised unbound state) with a kinetic energy $E - E_0$. Spectroscopy of the region just above the edge up to several tens of eV is referred to as XANES (for *X-ray absorption near edge structure*). The photoelectron energy is low and the associated wave extends over several interatomic distances. Modelling of the interactions is therefore made complex by the number of scattering atoms (*multiple scattering*). The XANES profile $\mu(E)$ primarily provides information on the oxidation degree of the absorber, the local symmetry of the coordination sphere and the occupation of the involved orbitals (Fig. 14). Qualitatively, this profile can be used as a *fingerprint* that is compared to that of reference compounds.

(3) At higher energies, single backscattering terms (involving one scatterer at a time) predominate and the corresponding spectroscopy is called EXAFS (*Extended X-ray absorption fine structure*). After correction, the EXAFS signal is described by the equation of [49]. The linear absorption coefficient derives from grouping scatterers per shell $j$ (same nature, same distance $R_j$), after averaging over all directions, and assuming a low thermal motion:

$$\mu(k) = \mu_0(1 + \chi(k)) \tag{18}$$

$$\chi(k) = -S_0^2 \sum_j \frac{N_j}{k R_j^2} |f_j(k)| e^{-2k^2\sigma_j^2} . \sin\left(2 k R_j + 2\,\delta_l(k) + \arg(f_j(k))\right) \tag{19}$$

where $f_j$ is the complex amplitude of the scattered wave, $\delta_l$ is the phase shift induced by the absorber, and $e^{-2k^2\sigma_j^2}$ the Debye–Waller factor arising from the disorder caused by thermal motion. Modelling parameters include electronic, $f_j(k)$ and $\delta_l$ — and structural terms, the number of neighbours of each layer: $N_j$, $R_j$ and $\sigma_j$. EXAFS allows a more complete depiction of the absorber local environment.

Instead of the transmission signal, the intensity of the fluoresced X-rays (or near-UV to near-IR luminescence intensity [50]) can be used, as absorption $\mu(k)$ is, in first approximation, proportional to $I_{\text{fluo}}(k)/I_0$.

### 3.3.2. *Elements studied using X-ray absorption spectroscopy techniques*

As shown in Fig. 14, all chemical elements are not equally studied by X-ray spectroscopy techniques. Fe and Cu clearly attract major attention. The main reason is their ubiquitous presence in artistic materials, being in pigments, inks, but also glass, or metallic artefacts. Similarly, Mn is present in various natural mineral or biogenic pigments, as well as in glasses. These elements being 3d transition metals, their electronic state is usually responsible for the optical appearance of artworks. In addition to heavier metals such as Ag, Sn and Sb, they are increasingly analysed by XAS techniques to get new insights on the chemical origin of optical effects in particular in glasses and ceramics such as opacity, iridescence, metallic, shine, or colour as well. XAS techniques are remarkably well suited for the analysis of such materials: since they are based on short distance probes, they can be equally applied on crystallised and amorphous samples. When performed in fluorescence mode, the selective analysis of minor elements, is possible, even in complex mixtures. Indeed, the above-mentioned optical effects are frequently obtained by introducing low quantities of these metals.

On the other hand, an increasing number of works aims at understanding the evolution of these materials with time (degradation, corrosion, role in paper ageing in manuscripts…). Questions are related to the stability of such chemical forms, as well as to their modification during cleaning treatments. The same way, most of the XAS experiments conducted at the S and Cl $K$-edges are related to the problematic of alteration (in paintings, metals, or wood as well). These elements can have

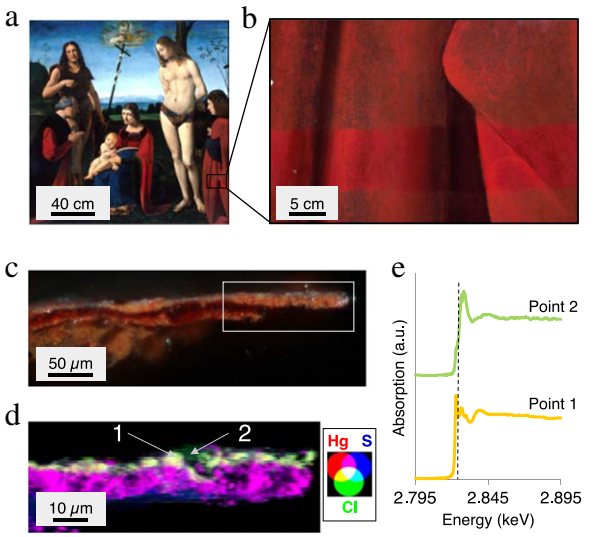


**Fig. 15.** *Madonna with Child, St Sebastian, St John the Baptist and two donors*, Boltraffio, between 1467 and 1471, Louvre museum (credits: C2RMF) studied at beamline ID21 at the ESRF; the dress of the donor, originally red, shows a severe darkening (a). The painting has been partially cleaned in 1995 (b). Cross-sections of tiny fragments reveal that the grey layer is only superficial (c). XRF mappings show the presence of S and Hg in both red and grey layers, while Cl appears only in the grey layer (d). Cl *K*-edge XANES reveals the presence of different chlorinated species and in particular mercury chloride type compounds in point 1 resulting from the reaction of chlorine on the original HgS pigment (e) [56,57]. (For interpretation of the references to colour in this figure legend, the reader is referred to the web version of this article.)

an exogenous origin, and XAS enables to determine if and how they react with the artistic materials. The effect of ambient $SO_2$ and chlorine of our cultural heritage is indeed a real concern.

The development of studies at the carbon and oxygen *K*-edges seen in Fig. 14 relates to organics speciation using STXM (Section 3.3.5).

### 3.3.3. *Recent developments in μXANES and μEXAFS*

As stated above, a large number of XAS experiments are focused on the characterisation of degradation reactions. Within the various artistic materials, pigments and paintings are currently being paid an increasing attention. μXANES is increasingly used for the study of pigments, and in particular for the characterisation of pigment alteration. Pigment degradation is usually a superficial phenomenon, where the major elemental composition remains unchanged, but where oxidation or reduction affects the chemical environment of elements, and consequently the colour of pigments. μXANES, which probes the element speciation, with very good sensitivity and with submicrometric resolution is therefore particularly relevant for such analyses. As an example, it has been recently used to study the fading of Prussian blue [51,52], the discolouration of smalt [4], the darkening of lead chromate in Van Gogh paintings [53], as well as in artificially aged model paintings [54]. In this case, it was shown that both in original and artificial painting fragments, pigment darkening was linked to the reduction of chromium from Cr(VI) to Cr(III). A similar reduction was observed in artificially aged zinc chromate paintings, mimicking the alteration affecting a masterpiece of George Seurat [55].

A more detailed example is presented in Fig. 15. This is one of several cases of cinnabar (HgS) darkening in paintings. μXANES has been exploited to better understand the role of chlorine and the instability of sulphur in the cinnabar colour changing. This degradation, which indeed is much more complex than a single chemical reaction, can affect not only frescoes, as at Pompei [58] but also canvas paintings, as observed in Rubens *The Adoration of the Magi* [59]. The example presented here was done on the Madonna with Child, St Sebastian, St John the Baptist and two donors, painted by Giovanni Antonio Boltraffio in ≈1470, presently in the Louvre collection. In this painting, cinnabar alteration is particularly visible on the dress of the donor, on the right side (facing painting) (Fig. 15a). Two rectangular cleaning tests carried out in 1995, are still visible today (Fig. 15b). The visible picture of a painting fragment cross-section shows a very complex red stratigraphy, covered with a tiny (≈2–5 μm) grey layer. XRF mappings revealed the specific presence of Cl, associated with Hg and S, in this grey layer (Fig. 15c, d). Additional XANES spectra were acquired at the S and Cl *K*-edges which demonstrated the presence of mercury chloride type compounds, in the alteration. In this example, the use of carbon tetrachloride in the 90's to treat the panel against woodworms is suspected to be at the origin of Cl introduction, and further degradation [57].

Fig. 16 shows μXANES spectra from two locations of the transverse section of an archaeological artefact immersed in a cupric solution. The general shape of the spectrum obtained at points 1 and 2 and the energy of the absorption edge are in good agreement with copper being present under the metallic Cu(0) form and significantly differs from Cu(II) compounds. This highlights the fact that $Cu^{2+}$-ions coming from the electrolyte were reduced at least 20 μm deep into the iron corrosion layer, revealing that electrons were available that deep during the corrosion process.

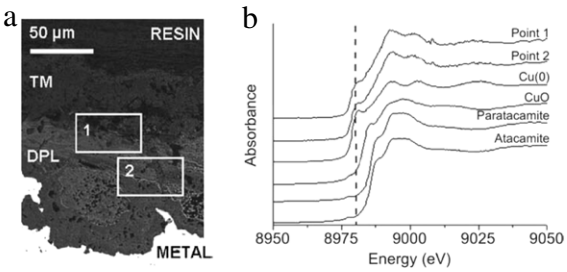


**Fig. 16.** µXANES study of the corrosion of an archaeological iron nails from the archaeological site of Glinet (sample GL08-18, Seine-Maritime, France) after immersion in $CuCl_2$ solutions. (a) Light microscopy image presenting two µXANES analyses zones from the corrosion or *dense product layer* (DPL). (b) Comparison between µXANES spectra of points 1 and 2 and reference powders showing that the copper is primarily present under its metallic form in the DPL. Data were collected at the SUL-X beamline at ANKA (Karlsruhe, Germany).
*Source:* Reproduced with permission from Saheb [60].

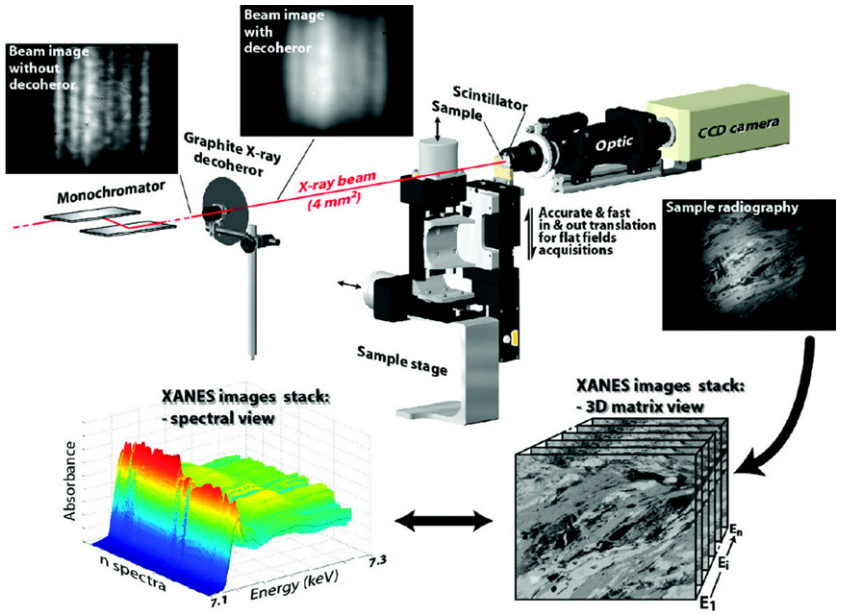


**Fig. 17.** Full-field µXANES setup developed at the beamline ID21 at the ESRF. This method provided mega-pixel elemental speciation maps, with a large field of view (≈4 $mm^2$) at a sub-micrometre resolution The typical projected pixel size achieved is 0.4–1.5 µm [61].

### *3.3.4. Scanning and full-field absorption imaging*

These analyses are usually carried out in fluorescence mode. XANES spectra are acquired over a few points, but barely over a complete 2D region. Some chemical mappings can be derived by exciting fluorescence at a few energies in the XANES region of the probed element. As an example, the pre-edge peak around 5.993 keV for the Cr *K*-edge allows the selective excitation of Cr(VI) [54]. It is also easy to selectively map sulphides and sulphates thanks to the 12 eV shift of the XANES edge, from S(−II) to S(+VI) [58]. However, such an approach is only applicable to a few cases, and assumes that samples can be described as simple binary or ternary pre-determined mixture.

In order to get a complete hyperspectral 2D-XANES dataset, a XANES full-field set-up was developed at the ID21 beamline, ESRF [61]. A complete set of radiographies is acquired while tuning the energy around the edge of interest, generating the corresponding set of XANES spectra, still with a submicrometric resolution, but over a millimetric 2D region (Fig. 17). This set-up has been primarily applied to geology, and is expected to find many applications in the field of cultural heritage and for the study of painting alterations in particular.

### *3.3.5. Potentials of scanning transmission X-ray microscopy*

At very low energies of a few hundreds of electron-volts, X-ray absorption can still be performed, and transmission X-ray microscopy has been an area of intense development particularly to image systems for life sciences in the water window [62,63] — i.e. the photon energy region 280–530 keV, respectively delimited by the carbon and the oxygen *K*-edges. In particular, carbon speciation using STXM is a powerful method to differentiate compounds from natural organic matter from C *K*-edge spectral signatures and peak positions of major organic functional groups [64]. Carbon *K*-edge STXM has been used in the field of palaeontology and palaeo-environments, allowing in particular the identification of faint signatures

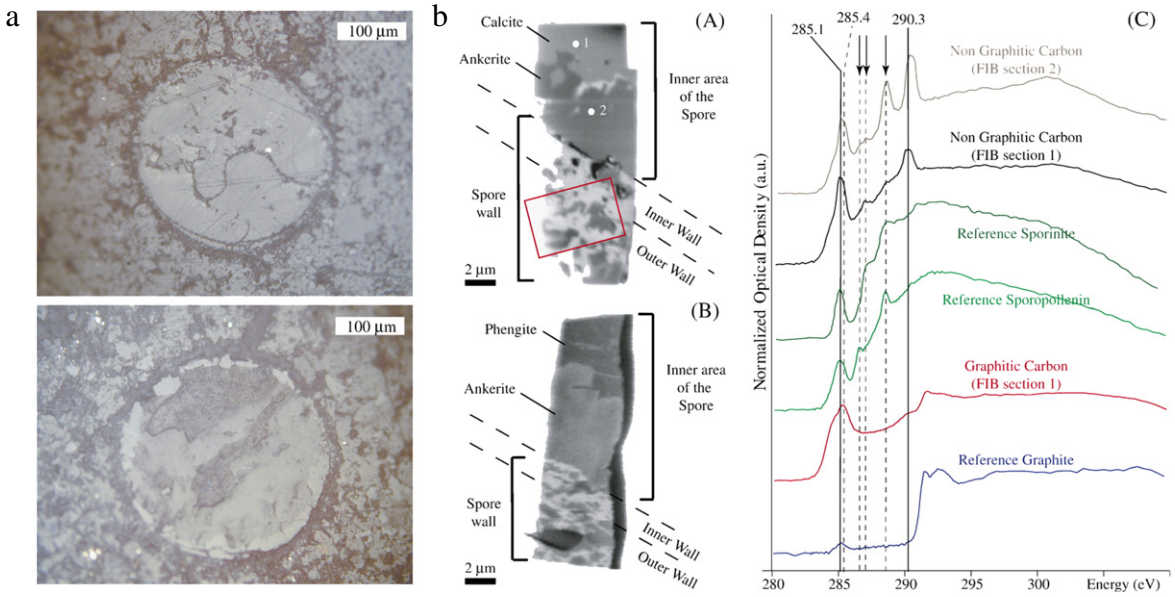


**Fig. 18.** Fossil lycophytes megaspores (230 Ma) found in Triassic metasedimentary rocks from the French Alps studied using the STXM beamline 11.0.2.2 at the *Advanced Light Source* (Berkeley, CA, USA). (a) Light microscopy images. (b) STXM images of organic matter (OM) composing the spore walls, (A) below the C *K*-edge at 280 eV (OM appears in bright spots) of the FIB Section 2 showing ankerite and calcite, (B) at 280 eV (OM appears in bright spots) of the FIB Section 2 showing ankerite and phengite. C. NEXAFS spectra of the different types of carbon observed in the FIB sections. For references spectra, please Ref. to [66]. Arrows at 286.7, 287.2, and 288.7 eV highlight peaks assigned, respectively, to ketone (C = O, $1s \rightarrow 2\pi^*_{C=O}$), phenol (Ar–OH, $1s \rightarrow \pi^*_{C\text{-}OH}$), and carboxylic groups (COOH, $1s \rightarrow \pi^*_{C=O}$).
*Source:* Reproduced with permission from Bernard [66].

from carbon functional groups; this may allow speciation of biological remnants even in very heavily diagenetised systems (Fig. 18) [23,65–67].

### 3.4. X-ray diffraction, scattering and related techniques

#### 3.4.1. Basic principles

The formalisms of X-ray diffraction are covered in many reference textbooks (see for example [21,68–70]). Here we will only present a short introduction into the basic principles.

X-rays are electromagnetic waves of wavelength $\lambda$ that can be described by a wave vector

$$\vec{k} = \frac{2\pi}{\lambda}\vec{n}. \tag{20}$$

The wave vector points in the direction of the momentum of the wave $\vec{n} = \vec{p}/p$. It is convenient to normalise the scattered intensity by the incident flux and the solid angle of the detector $\Delta\Omega$. This parameter is called the differential cross-section $(d\sigma/d\Omega)$. For a single electron it can be expressed as [21]

$$\left(\frac{d\sigma_{coh}}{d\Omega}\right) = \left(\frac{e^2}{4\pi\epsilon_0 m_e c^2}\right)^2 P = r_0^2 P, \tag{21}$$

with the elementary charge $e$, the speed of light $c$ and the permittivity $\epsilon_0$. The term inside the brackets is called the *classical electron radius* $(r_0)$ or the *Thomson scattering length*. $P$ is a polarisation factor and depends on the scattering geometry and the polarisation of the incident beam. For most synchrotron sources the beam is linearly polarised in the horizontal plane. $P$ is therefore

$$P = \begin{cases} 1 & \text{vertical scattering plane} \\ \cos^2\Psi & \text{horizontal scattering plane} \end{cases} \tag{22}$$

where $\Psi$ denotes the horizontal scattering angle. The polarisation leads to a decrease of the intensity scattered in the horizontal direction. This is the reason why most synchrotron beamlines try to work in a vertical scattering geometry.

The X-ray photons interact with the $Z$ electrons of each atom. The distribution (wave function) of these electrons is given by the solution of Schrödinger's equation. For our purpose, it is enough to view the atom as a cloud of electrons described by the electron density $\rho_e$. The wave field observed at the detector is a superposition of the waves scattered from different parts of the atom into the solid angle of the detector. It can be shown [21] that in the far field approximation the phase

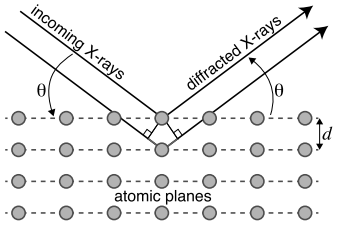


**Fig. 19.** Schematic representation of the Bragg's law. For constructive interference the path difference between rays reflected from the first and second crystallographic plane (shown in grey) must be $n \cdot \lambda = 2 \cdot d \sin\theta$.

difference between two waves scattered from positions $\vec{r}$ apart is $\vec{k}_e \cdot \vec{r} - \vec{k}_i \cdot \vec{r}$, with the incident wave $\vec{k}_i$ and the exit wave $\vec{k}_e$.

To calculate the scattering it is convenient to introduce the scattering vector or momentum transfer $\vec{Q} = \vec{k}_e - \vec{k}_i$. The scattering from an atom can be calculated by integrating over the electron density while taking the phase shift of the scattered waves into account and multiplying the result with the Thomson scattering length

$$\left(\frac{d\sigma_{coh}}{d\Omega}\right) = r_0^2 P \left| \int \rho(\vec{r})\, \mathrm{e}^{i\vec{Q}\cdot\vec{r}} d\vec{r} \right|^2 = r_0^2\, P f_0^2(\vec{Q}). \tag{23}$$

The integral $f_0$ is the Fourier transform of the electron density. It is called the *atomic form factor*. The derived term is correct for X-ray energies much higher than the absorption edges of the investigated material. For lower energies the so called *dispersion corrections* have to be applied

$$f = f_0(\vec{Q}) + f' + if''. \tag{24}$$

The values of $f'$ and $f'' = \sigma_{pe}/(2r_e\lambda)$ can be retrieved from published tables.

A (single) crystal is a three dimensional periodic arrangement of atoms. It can be described by a unit cell containing atoms with their respective structure factors $f_j$ at the positions $\vec{r}_j$. Depending on the symmetry of the crystal a lattice is chosen with the vectors $\vec{R}_n$ pointing at every lattice point. The complete crystal is obtained by duplicating the unit cell at each lattice point. The electron density of the crystal $\rho(\vec{R}_n + \vec{r}_j + \vec{r})$ is now a function of the vector $\vec{R}_n$, indicating the lattice cell, the vector $\vec{r}_j$, indicating the atom inside the cell, and the vector $\vec{r}$, indicating the position "inside" the atom. This allows to separate Eq. (23) into a sum over the unit cell and an independent sum over the lattice:

$$F_{\text{crystal}}(\vec{Q}) = \underbrace{\sum_j f_j(\vec{Q})\, \mathrm{e}^{i\vec{Q}\cdot\vec{r}_j}}_{\text{unit cell}} \underbrace{\sum_n \mathrm{e}^{i\vec{Q}\cdot\vec{R}_n}}_{\text{lattice sum}}, \tag{25}$$

where we have used the structure factor of the atom $j$, $f_j$. A more demonstrative, but also more limited formula can be obtained by analysing the reflections of X-rays from lattice planes, separated by the lattice constant $d$. As shown in Fig. 19, this leads to *Bragg's* law

$$n \cdot \lambda = 2d \sin\theta, \tag{26}$$

where $n$ is the diffraction order.

It can be shown [68] that $F_{\text{crystal}}$ is only non-zero if the scattering vector $\vec{Q}$ is equal to a vector of the *reciprocal lattice*. The basis vectors of the reciprocal lattice $\vec{b}_1$, $\vec{b}_2$ and $\vec{b}_3$ can be obtained from the basis vectors of the real-space lattice $\vec{a}_1$, $\vec{a}_2$ and $\vec{a}_3$

$$\vec{b}_1 = 2\pi \frac{\vec{a}_2 \times \vec{a}_3}{\vec{a}_1 \cdot (\vec{a}_2 \times \vec{a}_3)}, \tag{27}$$

$$\vec{b}_2 = 2\pi \frac{\vec{a}_3 \times \vec{a}_1}{\vec{a}_1 \cdot (\vec{a}_2 \times \vec{a}_3)}, \tag{28}$$

$$\vec{b}_3 = 2\pi \frac{\vec{a}_1 \times \vec{a}_2}{\vec{a}_1 \cdot (\vec{a}_2 \times \vec{a}_3)}. \tag{29}$$

For this reason the reciprocal lattice is a very helpful tool in the analysis of X-ray data.

So far, we have described the scattering of a single crystal. However, in nature and technology we almost never encounter single crystals. Except for specific cases (gems for instance), the samples of interest for art and archaeology will always be polycrystalline (if they are not amorphous). This means that they are composed of many small crystallites that each behave like a single crystal. However, the crystallites are in a random order and orientation towards each other. Illuminating

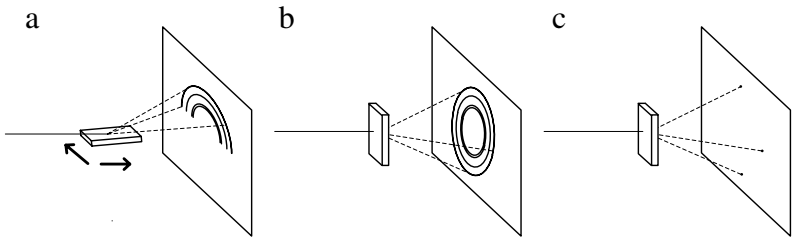


**Fig. 20.** Collection of 2D XRD raster-scans or *diffraction maps* in reflection geometry (a), and in transmission geometry (b) in a powder-type situation or when the beam size is below the crystallite size therefore leading to monocrystal-type diffraction (c). In the latter situation, integration of ring intensities may lead to strong errors in phase quantification.

such a sample with an X-ray beam leads to a smearing out of the diffraction pattern and the formation of the so called *Debye–Scherrer rings*. Depending on the illuminated volume, which depends on the beam size, and thereby on the number of crystallites illuminated, the rings can appear smooth (fine powder, Fig. 20a and b) or spotty (large grains, Fig. 20c). Analysis of the ring diameters and comparison with crystallographic tables allows to identify the crystalline structures, and thereby the phases, present in the sample. This is the main use of diffraction for archaeology and art. Knowledge of the phases inside the samples, often at a micrometric resolution, helps reconstructing what kind of materials and technologies were used in the creation of the artefact.

Fig. 7 shows typical experimental setups. The transmission geometry (Fig. 7n) can be used for thin sample sections. If the sample is too thick or too absorbing the reflection geometry (Fig. 7o) is used. It also allows to access higher order reflections. The SAXS setup (Fig. 7p) places the detector far behind the sample (if possible in a vacuum or helium flight tube) to analyse the low angle emissions with higher resolution.

Detectors, independent of their type, can only measure the scattered intensity which is obtained by squaring the absolute value of the scattering amplitude

$$I = \left|F_{\text{crystal}}(\vec{Q})\right|^2 . \tag{30}$$

This leads to a loss of the phase of the scattered wave. As the scattered amplitudes are a Fourier transform of the electron density of the crystal a simple Fourier back transformation of the complex wave field should be sufficient to obtain the crystal structure. However, due to the loss of the phase this is not possible anymore. To overcome this problem a number of techniques have been developed that use reference waves or iterative mathematical algorithms to "guess" the phase [71–76]. This techniques will become more important at 4th generation X-ray sources that will provide radiation with large coherence lengths.

The first diffraction patterns were recorded with photographic films. The resolution obtained with films is still superior to modern digital detectors. However, due to the problems of digitising the data afterwards for further treatment they are rarely utilised today. Instead, detectors that directly transform the photons into electric pulses are used. Point counters, such as scintillation detectors, allow the determination of the X-ray flux emitted into a small area of reciprocal space with high accuracy. One or two dimensional detectors measure the X-ray flux with spatial resolution, which significantly reduces the time needed for an experiment. Two-dimensional detectors used today are mainly image plates, charged coupled devices (CCD) and pixel detectors. CCD detectors are very common because they are easy to handle, robust and can be adjusted to different X-ray energies by changing the phosphor screen. A disadvantage of CCDs is the large point-spread function that is generated by the phosphor and that increases with the thickness of the screen (and hence its efficiency). CCD chips are read out line by line from the sides. This limits the read out speed and makes them slower than pixel detectors. Pixel detectors are a very recent development. Their multi-pixel sensor is directly illuminated by X-rays and each pixel is read out separately. They have a high dynamic range, very fast readout and no internal noise. Unfortunately, today only small sensor chips can be produced. Larger detectors can be created by tiling several sensors together; however, this creates blind areas or distorted pixels at the edges of the chips. Today, the largest pixel detectors are made of pure silicon, which has a low quantum efficiency for high X-ray energies. However, strong development efforts are undertaken to create large chips that are bonded to high-Z semiconductors, such as GaAs and CdTe.

### *3.4.2. Micro- and nano-X-ray diffraction*

Performing diffraction experiments with focused X-ray beams allows the investigation of small or heterogeneous objects [78,79]. The resolution of the technique depends on the size of the focal spot and has to be adapted to the object under investigation. Typically experiments are performed with a resolution of a few micrometres. An accurate positioning and sample observation system is needed to investigate the sample. In addition, if the sample features areas of different elemental composition, X-ray fluorescence is often used to identify the position of the object hit by the beam (see for example [80]). The advantage of micro-diffraction experiments is that they allow to separate different components, thus vastly facilitating the analysis of the diffraction pattern. In addition, they allow the investigation of individual small objects and, combined with a raster-scanning setup, imaging with diffraction contrast at the micron scale.

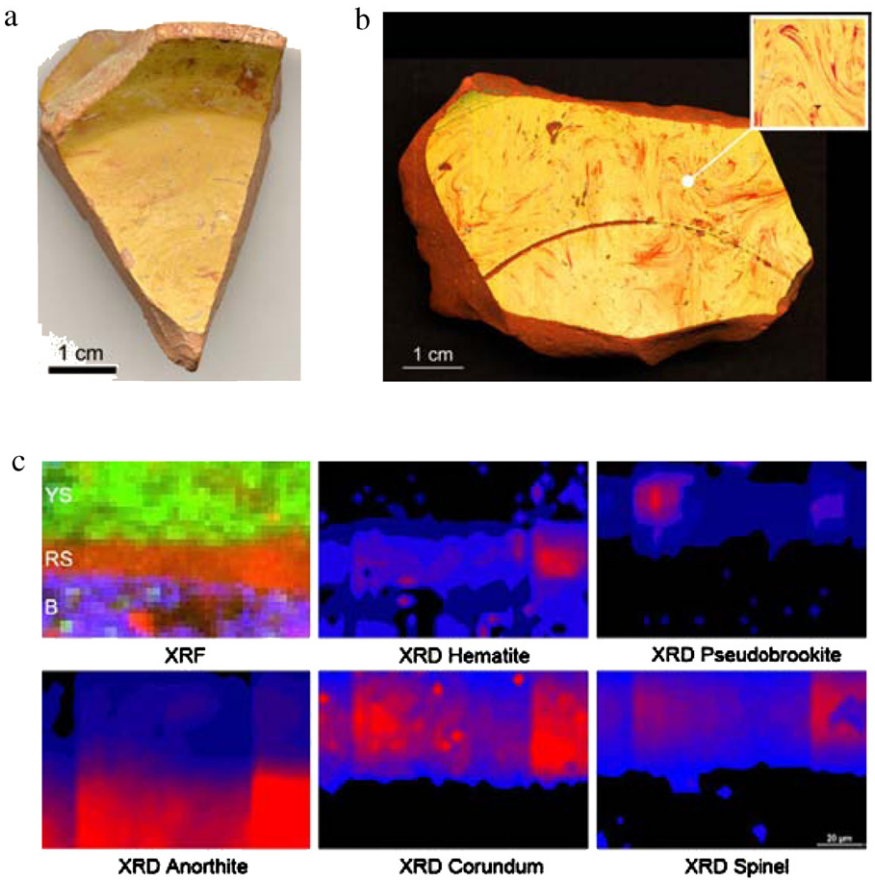


**Fig. 21.** XRD study on a sample of *terra sigillata* from the Gallic workshop *La Graufesenque*. (a) Photography of a terra sigillata sherd. (b) Light microscopy image of the sample. (c) XRF and mineral maps obtained by integrating XRD patterns over the intensity of the characteristic *d*-spacings of the mineral phases. The experiments were performed at the *Stanford Synchrotron Radiation Light Source* (Menlo Park, CA, USA).
*Source:* Reproduced with permission from Ph. Sciau [77].

Recent advances in X-ray focusing optics have allowed to reach ever smaller beam sizes and thereby the investigation and the imaging of objects smaller than microscopic resolution. One of the biggest drawbacks of micro-beam techniques is the radiation damage that is caused by the high flux density of the beam. Most organic materials quickly lose long-range order when illuminated [81–83]. This effect is aggravated in humid environments, where the photolysis of the water molecules causes the formation of aggressive radicals.

This technique is used in the field of archaeology and cultural heritage studies to analyse archaeological textile fibres [84–86] and hair samples [93], investigate paint cross-sections and identify archaeological pigments [77,87–89]. An example is shown in Fig. 21. The combined use of $\mu$XRD and $\mu$XRF allows the investigation of the mineral content of the paint layer of a *terra sigillata* sample and thereby the identification of the pigments used [77].

### *3.4.3. Small-angle X-ray scattering*

Due to the reciprocal scattering law the investigation of signals scattered to very low angles contains information on larger than atomic length scale. Small angle X-ray scattering (SAXS) allows to access the electron density distribution at the mesoscale. The presence of nanoparticles leads to diffraction peaks or rings that are modified by the geometry and size dispersion and interaction of these particles. In many systems, a characteristic decay law of the small angle scattering intensity can be found which yields information about the properties of the material. For an introduction to synchrotron SAXS see [91]. Small angle scattering experiments are usually performed at specialised beamlines. A parallel beam is needed to separate the scattered signal from the primary intensity. To resolve the scattering with enough resolution the detector is often placed several metres behind the sample (see Fig. 7p). An evacuated flight tube is placed between the sample and the detector to avoid scattering by air. SAXS is widely used in polymer, pharmaceutics and cosmetics research, however, it is also an interesting tool for ancient materials investigations of fibres, porous objects like stones and paint and organic samples like leather [92] and parchment [90], textiles and hair strands [93] and bone [94–96]. Fig. 22 shows an example of a combined SAXS/WAXS study of historical parchment.

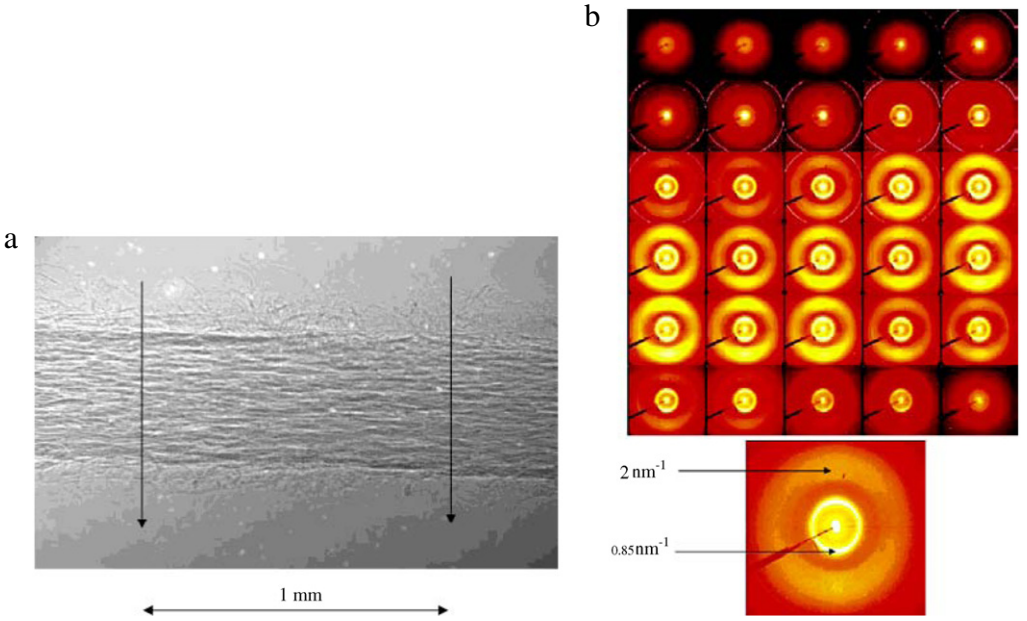


**Fig. 22.** (a) X-ray transmission image of a cross-section of a 238 years old parchment sample. The black arrows indicate the place where X-ray micro-focus investigations have been performed. (b) X-ray diffraction images from a scan through a 186 years old parchment sample. The first image is on the top left, the diffraction patterns are organised into rows. The top of the sample corresponds to the outer skin layers of the animal, where sharp rings indicate the presence of minerals. The individual image stems from the inner part of the parchment. The 0.85 and 2 $nm^{-1}$ reflections of the collagenous component can be seen. Data collected at the beamline ID18F at the ESRF.
*Source:* Reproduced with permission from Kennedy et al. [90].

### *3.5. X-ray computed tomography and related techniques*

#### *3.5.1. Basic principles*

X-ray microscopy takes advantage from the absorption (photo-electric effect) and (elastic) scattering (or refraction) of X-rays in their interaction with matter, giving rise to different imaging modalities [97]. The matter property that encapsulates these processes is the index of refraction $n$:

$$n(Z, E) = 1 - \delta(Z, E) + i\,\beta(Z, E) \tag{31}$$

where $\beta$ is proportional to the photo-electrical cross-section $\sigma_{pe}$ and $\delta$ to the electron density $\rho_e$ [98]. Which effect dominates the other depends mostly on the sample composition, X-ray energy and imaging geometry (i.e. sample–detector distance). When the propagation distance between the object and the detector is small, the refraction effect, in a first approximation, can be neglected. In such case, the obtained contrast primarily results from the decreased intensity of the X-ray beam traversing a sample, according to the Beer–Lambert law (ref. 3.1):

$$I(Z, E) = I_0(E)\ \exp\left(-\int \mu_l(Z, E)\,\mathrm{d}z\right) \tag{32}$$

with $I(Z, E)$ and $I_0(E)$ the X-ray beam intensity after and before the object (Fig. 23). The linear attenuation coefficient $\mu_l(E, Z)$ is related to $\beta$ as follows: $\mu_l = 4\pi\beta/\lambda$, and has a strong dependence on the atomic number $Z$ ($\propto Z^4$, Eq. (12)). This feature provides high contrast between materials with different densities, if the energy of the X-ray beam is properly tuned. In fact, since $\mu_l \propto E^{-3}$ (Eq. (12)), the optimal penetration depth into the material of interest leading to the highest contrast can be achieved by ad-hoc energy selection.

When the study object is composed of light elements or elements with close atomic number $Z$, refraction of X-rays at internal material boundaries in the sample becomes of interest for boosting the often insufficient observed contrast. In fact $\delta$ is small (around $10^{-5}$), but still about 3 orders of magnitude larger than $\beta$. Because the index of refraction $n$ only slightly deviates from unity, the refraction angle $\alpha$ is tiny but can be determined with great accuracy by so-called phase contrast techniques. It can be shown namely, that the refraction angle $\alpha$ is proportional to the gradient of the phase $\phi(x, y)$ of the refracted beam [99], e.g.:

$$\alpha_x = \frac{\lambda}{2\pi}\frac{\partial\phi(x, y)}{\partial x} = \int \frac{\partial\,\delta(x, y)}{\partial x}\,\mathrm{d}z \tag{33}$$

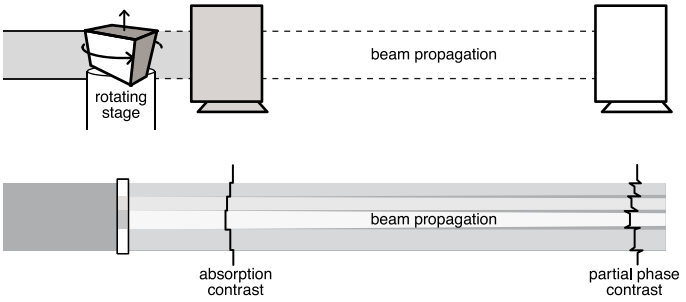


**Fig. 23.** (top) Setup for absorption and free-space propagation phase contrast tomographic microscopy, with the detector located close and further away from the sample, respectively. Note that the low divergence of the X-ray source generally leads to parallel or fan-beam geometry, and not cone-beam geometry. The reconstruction is then made easier as exact algorithms can be used. (bottom) Schematic representation of a sample together with its absorption and phase contrast projections, with the internal sample boundaries strongly enhanced in the latter case.

where $\delta$ is related to the electron density $\rho_e$ according to:

$$\delta = \frac{r_0\,\rho_e\,\lambda^2}{2\pi} \tag{34}$$

with $r_0$ being the classical electron radius.

If X-rays are instead viewed in the light of their particle nature, their macroscopic behaviour characterised by the index of refraction can be explained by elastic scattering resulting from the interaction of the X-ray photons with the electrons of the atoms constituting the studied material. Following the theory for elastic scattering, derived assuming that the electrons are not free, but in bonds and therefore modelled as damped harmonic oscillators with a resonance frequency and a damping constant, a relationship between $\sigma_{pe}$ (or $\beta$), which can be determined experimentally, and $\delta$ can be derived [98]. In addition, the link between these macroscopic properties and the microscopic scattering of photons can also be understood. In fact, the index of refraction $n$ is related to the dispersion corrections $f'$ and $f''$ [63]:

$$n = 1 - \frac{1}{2\pi} N_A\, r_0\, \lambda^2 (f' + if'') \tag{35}$$

and the Kramers–Kronig relationships [100] provide a link between $f'$ and $f''$. In this way, if $\beta$ is known, $\delta$ can be derived.

A 2D projection of an object provides useful information (e.g. as exploited in radiographs in the medical field) on its internal structure and composition. This gained knowledge is however cumulative and in this way an absorber or scatterer cannot be unambiguously located in the 3D space. Tomographic approaches overcome this ambiguity by recording a series of projections (or Radon transforms) with the object rotated at different angles. The 3D structural information can then be reconstructed using techniques based on Fourier analysis (e.g. filtered back-projection) or iterative methods (computationally inefficient, but useful in cases with insufficient data). Fourier analysis methods [101] are based on the Fourier slice theorem, stating that the Fourier transform of the parallel projection of the property of a sample (e.g. $\mu_l$) taken at a certain angle equals a line of the 2D Fourier transform of the object taken at the same angle. Information on the studied sample can then be recovered by a 2D inverse Fourier transform (or back-projection approaches).

To achieve a given sensitivity $\Delta\mu_l/\mu_l$ in a tomographic experiment, the chosen energy has to be high enough to ensure sufficient X-ray photon statistics at the detector within an acceptable time span. However, if the energy is too large, only few photons are absorbed by the sample and therefore the sensitivity for small changes in $\mu_l$ decreases. For an arbitrary sensitivity, scan times are minimised by the relation $\mu_l \cdot D = 2$, where $D$ is the sample diameter [102].

Current trends in hard X-ray *tomographic* microscopy aim at improving the density, spatial and temporal resolution. In addition, work is also going on to overcome the inconvenient physical shape of some objects (large flat samples, e.g. paintings or slab of rocks containing fossils).

### 3.5.2. X-ray phase-contrast imaging

X-ray phase contrast techniques aim at detecting the refraction angle $\alpha$ or a manifestation of the beam refraction (e.g. an interference pattern) with great accuracy. Existing methods fall into three main categories: free-space propagation [103,104], interferometry [105–107] and analyser systems [108,109] (Fig. 24).

The main advantages of the free-space propagation technique are the achievable spatial resolution and its simple setup, since no additional hardware is required (Fig. 24). If the probing X-rays are (partially) spatially coherent, their refraction at interfaces separating domains with different $\delta$ leads to interference phenomena with the directly transmitted beam. In a projection, this effect manifests itself as Fresnel fringes and is localised at domain boundaries (Fig. 23). It is therefore often called *edge enhancement*. This effect becomes more prominent with increasing propagation distances, i.e. for a large sample–detector separation. Although the contrast between areas with different $\delta$ is not improved compared to standard absorption tomography, internal boundaries are in this way clearly visualised. This approach is routinely used for the non-destructive investigation of organic inclusions preserved in amber samples [116] and visualisation of the internal structure of fossilised flowers, plants and seeds (e.g. [117,118]) (Fig. 25a). It has also proved invaluable for extracting information

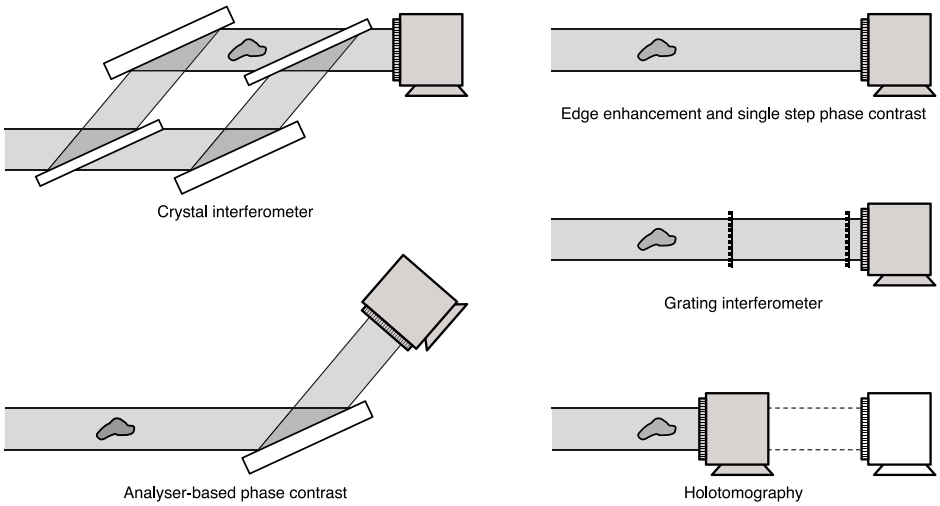


**Fig. 24.** Main categories of phase-contrast setups: Crystal interferometer [110], Analyser-based (*Diffraction Enhanced Imaging, DEI*) [109,111], Edge-enhancement and single step phase contrast [103,112–114], Grating interferometer (*Differential Phase Contrast, DPC*) [107], Holotomography [115].

on incremental dental development (Fig. 25b), also aimed for instance at better understanding primate evolutionary developmental biology or at resolving ongoing debates over hominin life history (e.g. [7]).

Fresnel fringes do not only allow better localisation and visualisation of internal boundaries. They also contain information on the wavefront phase and therefore on $\delta$. Several algorithms exist to exploit this information and they usually consist of two steps. First the phase information (or a related quantity) is retrieved from the projection data. Tomographic reconstruction of these phase projection maps is then performed with classical routines also used for absorption tomography (e.g. [101]). Simpler approaches for phase retrieval, based on the transport-of-intensity equation [112–114], require datasets acquired at only one single sample–detector distance. Although these methods are not fully quantitative and are based on different assumptions (e.g. homogeneous composition [114] or negligible absorption [113]), the provided image contrast is usually largely sufficient for enabling optimal segmentation and post-processing for specimens constituted either by low absorbing materials or materials with similar linear attenuation coefficients. Fully quantitative results for low absorbing samples can be obtained if tomographic datasets at multiple distances are acquired. In fact, combining the information provided by projections taken at different defocusing distances to obtain a projected phase map of the sample for each angle of the tomographic scan obviates the distance-dependent blindness to some spatial frequencies. This technique is known as holotomography [115]. Although it is not so often applied, due to the longer data acquisition required and the involved data post processing, it delivers superior results. Refinement of the holotomography approach with the aim of analysing strong absorbing objects (e.g. fossils) [121] demonstrated the great potential of this technique. It was in fact possible to accurately image mineralised soft tissue (brain) inside a dense fossil [122]. The other above-mentioned phase contrast methods also provide excellent results and in some cases feature a higher density discrimination power, since they directly measure the phase shift [105] or the phase gradient [107], rather than the Laplacian of the phase, as in free-space propagation techniques. Nonetheless, they are not commonly used for the investigation of ancient and historical specimens, mostly because of their demanding experimental setups. Grating interferometry [107] is though a promising technique when high sensitivity is required and medium spatial resolution is sufficient, once it will be compatible with high X-ray energies.

### *3.5.3. Hard X-ray nano-tomographic microscopy*

Most hard X-ray tomographic microscopy end stations at third generation synchrotron sources are based on parallel-beam geometry. With this configuration, millimetre-sized samples can be investigated with sub-micron resolution, limited by current detector technology. Resolution in the 100 nm range for smaller specimens (tens of micrometres) requires X-ray optics. In case of a full-field geometry, a condenser (Fresnel zone plate [123], beam-shaper [124], capillary [125] or mirrors [126]) produces the illumination of the sample and an objective Fresnel zone plate lens is used for the magnification of the image of the specimen on the detector. So far, this approach has mainly been exploited in the soft X-ray regime (e.g. water window) where diffractive optics is most efficient and resolution below 100 nm has been reported [127–129]. Recent efforts have though proved its feasibility also at energies above 8 keV [130] relaxing complex experimental requirements inherent to soft X-rays (e.g. short focal lengths or the necessity to work in vacuum) and enabling the investigation of thicker and denser samples, thanks to the higher penetration depth of hard X-rays and to the larger depth of focus of the optics at these energies.

For low absorbing samples, phase contrast can also be exploited. Common techniques include Zernike [130,131] (through manipulation of the wavefield in the back focal plane of the objective lens) and differential (by using different optical elements, e.g. a spiral zone plate as objective lens [132]) phase contrast imaging methods.

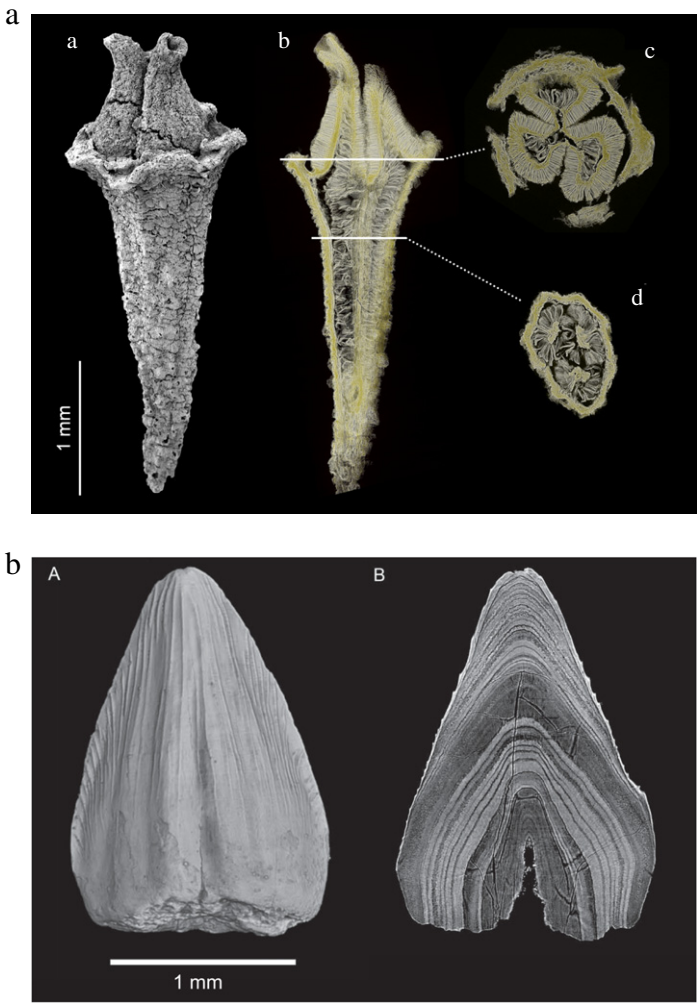


**Fig. 25.** Propagation phase-contrast (edge-enhancement) tomographic microscopy (a) of a 84 Ma old fossil flower (*Silvianthemum suecicum Friis*) from Sweden: (a) SEM image, (b–d) Virtual sections (volume rendering (voltex) of 20 consecutive slices) through the tomographic dataset in the sagittal (b) and axial (c-d) directions. Data acquired at the TOMCAT beamline [119] at the SLS-PSI, energy: 10 keV, voxel size: 0.74 μm, propagation distance: 10 mm. Sample courtesy: E. Friis. (b) Propagation phase-contrast (edge-enhancement) tomographic microscopy of a tooth of crocodilian *Atoposauridae* (CHEm03.503, Berriasian, Cherves-de-Cognac, Charente, France): (A) 3D rendering of the surface of the tooth, (B) Sagittal virtual slice. Data collected at beamline ID19 of the ESRF, energy: 20 keV, voxel size: 2.8 μm, propagation distance: 50 mm. *Source*: Reproduced with permission from Pouech [120].

Resolution in the order of 100 nm can also be achieved with a hard X-ray projection microscope, with a sub-100-nm focus produced by Kirkpatrick-Baez mirrors [133]. This approach is particularly suited for dynamical studies, since microscope efficiency and spatial resolution are in this case mostly decoupled. Due to the large distance between sample and detector for the highest magnification configuration, single projections feature both phase and absorption information. For high quality results, this information needs though to be disentangled using knowledge provided by radiographs acquired at different focus-to-sample distances and rather involved phase retrieval algorithms.

Nanometre resolution is crucial for the investigation of nanofossils, for instance in palynology. Knowledge of the morphology and internal ultrastructure of fossilised pollen, spores or acritarchs is critical e.g. for evolutionary studies of plants and for a better understanding of palaeoclimate and palaeoenvironmental conditions. For the study of degradation processes, for instance of paintings, and in conservation science, structural information at the nanometre level (e.g. porosity) could also be important (Fig. 26) and is complementary to the average mesoscale properties obtained from small angle X-ray scattering (SAXS, see Section 3.4.3).

### *3.5.4. Ultrafast X-ray tomographic microscopy*

A high quality tomographic dataset can be routinely acquired, at most synchrotron facilities, in about 5–30 min, depending on the energy used and the aimed resolution, requiring the sample to be stable within this time span. This

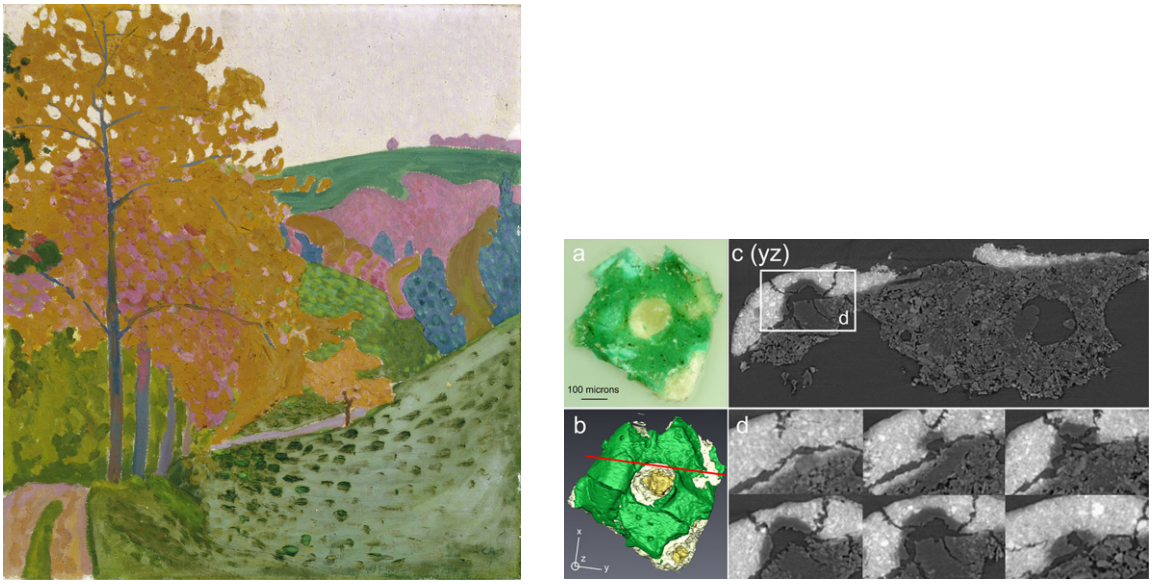


**Fig. 26.** Cuno Amiet, *Herbstlandschaft* (*Autumn Landscape*), 1906, oil on canvas, 61 × 55 cm$^2$ (private collection, Copyright: M. and D. Thalmann, Herzogenbuchsee). Investigation of the destructive effect of calcium soap migration in the painting using standard synchrotron X-ray tomographic microscopy applied on a painting micro-fragment. (a) Light microscopy image, (b) 3D rendering of the X-ray tomographic data, (c) virtual section along the red line in (b). Expansion of calcium soap aggregates into large pores is observed (c), as well as formation of such soaps at the paint-ground interface (d). Data acquired at the TOMCAT beamline [119] at the SLS-PSI, energy: 17 keV, voxel size: 370 μm. Data courtesy: Ferreira [134]. X-ray nano-tomographic microscopy would be important for the characterisation of the porosity beyond the micrometre level as well as for unravelling the spatial organisation of the single ground and paint particles. X-ray ultrafast tomographic microscopy could instead be used to advance the understanding of the dynamics of calcium soap formation and migration, using for instance ad-hoc prepared material subjected to different external conditions (e.g. temperature).

condition is not a problem for the study of static specimens. However, it becomes a nuisance when evolving objects and dynamic processes are of interest.

Recently, the high brightness of third generation synchrotron sources coupled to latest detector CMOS technology has been tremendously pushing the achievable temporal resolution, enabling the acquisition of high resolution tomographic datasets in less than 1 s, making new experiments possible. In this way, dynamic processes can be followed in 3 dimensions through time [135].

X-ray tomographic microscopy with sub-second temporal resolution could be crucial for a better understanding of degradation processes and conservation techniques for historical objects. If degradation (e.g. through exposure of a specimen to light, heat sources, humidity…) is fast or could be accelerated for investigation purposes, ultrafast tomographic microscopy would give insight into the structural changes as they occur, optimally unravelling the key processes involved (Fig. 26). The same is true for conservation techniques involving physical and chemical treatments, often not yet fully understood at the microscopic level, of unique and extremely valuable objects.

### *3.5.5. Laminography*

The optimal specimen size for micrometre resolution tomographic microscopy is in the order of few millimetres. Best results are actually obtained, when the analysed object completely fits in the available field of view. Small region of interests in larger samples can nonetheless also be successfully investigated using a local tomography configuration [15] and appropriate reconstruction algorithms [136,137] to mitigate the artefacts inherent to this geometry. More problematic is the examination of flat, laterally extended objects. In fact, in this case strong absorption occurs in the directions parallel to the lateral orientation of the specimen, preventing the acquisition of a consistent dataset. Although reconstruction of limited angle tomographic data is possible [138], the results often lack in quality.

Recently, inspired by tomosynthesis principles [139], Helfen et al. [140] developed laminography approaches adapted to the specificities of the synchrotron source. This technique relaxes geometrical requirements of standard tomographic microscopy and uses an inclined rotation axis with respect to the beam path. With the flat sample mounted with its normal parallel to the rotation axis, this configuration provides several advantages. A complete 360° scan is in this way accessible and the energy can be tuned to obtain an optimised and comparable average transmission for all acquired projections. In addition, despite incomplete sampling of the Fourier space, the rotational symmetry of the missing wedge leads to less severe artefacts compared to limited angle tomography. Phase contrast capabilities for this setup have also been developed [141].

Recent work shows the potential of this method. Using this emerging technique, Houssaye et al. [142] were able to virtually extract the remains of a prehistoric fossilised marine snake from a 10 cm large rock slab. Krug et al. [143] demonstrated the usefulness of laminography for detecting hidden cavities and therein contained relics sandwiched between high-$Z$ painting layers and thick wood panels in a mediaeval altarpiece.

## 4. Synchrotron ultraviolet/visible and infrared techniques

The Born–Oppenheimer approximation leads to consider, that since the mass of nucleus is much higher than the mass of electrons, it is possible to treat separately the electronic and the nuclear wave functions, as well as electronic and nuclear energies. In first approximation, the energy can be expressed as the sum of an electronic term $E_e$, linked to electrons energy, a term $E_v$, linked to nucleus vibration, and a term $E_r$, linked to nucleus rotation.

$$E = E_e + E_v + E_r \text{ with } E_e \gg E_v \gg E_r \tag{36}$$

where $E_e$ is typically in the UV/visible/near IR range, $E_v$ in the mid-infrared domain, and $E_r$ in the far infrared domain.

### 4.1. Synchrotron ultraviolet/visible spectroscopy and related techniques

#### 4.1.1. Basic principles

The principle of photoluminescence results from the absorption of photons by species. Under photo-excitation, an electron from an orbital in the electronic ground state $S_0$ (typically a bonding or lone-pair orbital, or valence band in crystals) is promoted to an unoccupied orbital of higher energy (typically a non- or anti-bonding orbital, or conduction band in crystals). The latter corresponds to an electronic excited state, usually a vibrational level associated to a singlet state. A molecule in a vibrational level of the excited state quickly falls to the lowest vibrational level of this state $S_{i\geqslant 1}$ by non-radiative energy transfer to other molecules through non-radiative processes such as collisions. The molecule can also give away the excess energy to other possible vibration and rotation modes (Fig. 27b). Fluorescence, or phosphorescence, occurs when the molecule returns to the electronic ground state $S_0$ or associated vibrational levels, from the excited singlet or triplet state, respectively, by emission of a photon of energy $h\nu \leqslant E_{S_i} - E_{S_0}$.

Atomic or molecular optical transitions between two energy levels 1 and 2, such as absorption and emission, can be described with the three Einstein's coefficient $A_{21}$ and $B_{12}$ and $B_{21}$, corresponding to the *spontaneous emission coefficient*, the *absorption coefficient* and the *stimulated emission coefficient*, respectively. Eq. (37) shows that at thermal equilibrium, the Einstein coefficients are related such that the rate of spontaneous emission and stimulated emission is equal to the rate of absorption

$$N_2A_{21} + N_2B_{21}\rho(\nu) = N_1B_{12}\rho(\nu) \tag{37}$$

where $N_1$ and $N_2$ are the number of species in states 1 and 2 respectively, $\rho(\nu)$ is the energy density incident on the sample at frequency $\nu$. $A_{21}$ is the transition probability per unit of time for a specie to go from level 2 to 1 by emission of a photon and corresponds to the luminescence phenomenon. In contrast, $B_{21}$ relates to the transition probability per unit time for emission due to incoming radiation.

$$A_{21} = \frac{8\pi h\nu^3}{c^3}B_{21}. \tag{38}$$

Eq. (38) shows that the ratio $A_{21}$ / $B_{21}$ is proportional to the cube of the frequency. As a consequence, the nature of the emission phenomenon is principally spontaneous in the UV/VIS domain whereas this is no longer true at lower frequency, or higher wavelength [144].

The luminescence phenomenon can be described by means of its spectral and temporal characteristics. Emission and excitation spectra inform on the distribution of probability of the transition between the excited and the ground states, and the luminescence quantum yields reflect the fraction of photons emitted by a material relative to that absorbed. The radiative lifetime is the time window during which the emission of photons can be observed. Both the spectral and temporal components of the luminescence signal can therefore be exploited to separate, identify or characterise species within complex mixtures.

The luminescence properties of a material are correlated to the behaviour of its electrons under photoexcitation, such as their ability to be delocalised. As a result, both intrinsic (physical state, chemical composition) and extrinsic characteristics (local environment) may influence either its electronic states levels or the excitation and de-excitation pathways involved in the luminescence phenomenon. In the current context, the luminescence properties of hard and soft condensed matter will be principally discussed. As of intrinsic parameters, the chemical structure of a material in a given state, as for example, the degree of conjugation of the $\pi$ orbitals in aromatic hydrocarbons, or the periodic nature of the atom lattices in a semiconductor, will define the energy levels at which the electrons will be allowed to be promoted to and decay from, under photoexcitation. Moreover, selections rules defined by quantum mechanical laws apply during the absorption and emission transitions. As a result, *allowed* and *forbidden* transitions (symmetry-forbidden and spin-forbidden) can be used to estimate excited-state lifetimes and quantum yields. As of extrinsic parameters, the pH, the presence of quenchers and the temperature will also influence radiative lifetime and luminescence quantum yields of the species involved, including by modifying the chemical structure or conformation of the luminophores or of their local environment.

The diversity in the chemical composition, the heterogeneity and the state of conservation of materials used in archaeological, palaeontological and cultural heritage samples condition the level of information which can be retrieved from luminescence measurements at a given spatial resolution. At the macroscale, several parameters can limit a finer

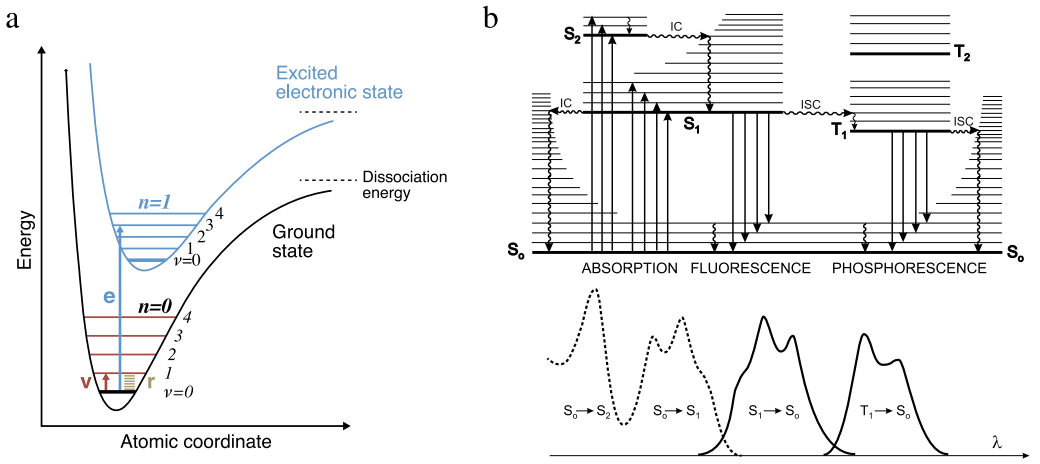


**Fig. 27.** (a) Potential energy diagram showing: **e** electronic transition (UV/visible/near IR), **v** vibrational transition (IR), **r** rotational transition (far IR), The vertical transition derives from the Born–Oppenheimer approximation. (b) Perrin–Jablonski diagram and illustration of the relative positions of absorption, fluorescence and phosphorescence spectra. Adapted with permission from Valeur [144]. As indicated by Valeur, characteristic time scales are: absorption ($10^{-15}$ s), vibrational relaxation ($10^{-12}$–$10^{-10}$ s), lifetime of the excited state $S_1$ ($10^{-10}$–$10^{-7}$ s, *fluorescence*), intersystem crossing (ISC, $10^{-10}$–$10^{-8}$ s), internal conversion (IC, $10^{-11}$–$10^{-9}$ s), lifetime of the excited state $T_1$ ($10^{-6}$–10 s, *phosphorescence*). $S_0$: fundamental electronic state, ($S_i$): singlet states, ($T_i$): triplet states, additional levels are quantified vibrational and rotational levels associated with each electronic state.

interpretation of materials' luminescence properties. For example, in case of heterogeneously mixed materials, the absorbance, scattering and luminescence properties of the surrounding environment of a luminescent particle may distort its intrinsic luminescence emission. Additionally, the variation of the luminescence properties of isolated individual particles from a same material can also be buried by stronger emission bands showing a greater spatial homogeneity. As a result, important information relative to the luminescence of isolated particles can be lost.

In full-field mode, luminescence images are collected on the whole field of view determined by the objective through a set of dichroic cubes, composed of an excitation and an emission filters and a dichroic mirror, allowing select a discrete number of excitation and the emission ranges. This type of technique is based on the selection of both the excitation and the emission ranges to stress contrast between the luminescence from micrometre-thin layers, otherwise indistinguishable under white light [145]. In narrow-field configuration, the size of the area analysed is defined by that of a pinhole aperture located in the excitation and/or the emission path(s) of the microscope. The coupling of the microscope with a dispersing optical component and a detector allow performing luminescence spectroscopy from micrometre size areas. Using benchtop instrumentation, luminescence microspectroscopy has been applied to the study of binding media and varnishes in cross-sections [146] and paint layers containing lake pigments [147].

### *4.1.2. Assets of synchrotron-based UV/VIS luminescence spectro-microscopy and full-field imaging*

In the aim of exploiting the luminescence signal from sub-micrometre size luminophores embedded in heterogeneously mixed materials, a fully continuous tunability of the excitation and a detection allowing sub-micrometre spatial resolution and nanometre spectral resolution are required. In this respect, the synchrotron radiation UV/VIS beam presents some advantages over classical UV sources used on benchtop instruments, in addition to the brightness of the beam. For instance, the fully tunable excitation synchrotron beam available at the DISCO beamline at the SOLEIL synchrotron (France) spans from 180 out to 600 nm (6.9–2.0 eV). When highly monochromatised, the energy of the beam can be used as a selection parameter to retrieve luminescence signals from structure containing lone-pair electrons (-Ö-, -N̈<, -S̈-), $\pi \rightarrow \pi^*$ transitions from isolated >C=C< bonds in organic molecules), as well as high bandgap energy semiconductors by allowing their selective excitation.

In the context of a recent study developed at the DISCO beamline (SOLEIL synchrotron), new methodological protocols using UV/VIS synchrotron radiation were defined to characterise small quantities of organic and inorganic compounds encountered in historical micro-samples, using both raster-scanning micro-spectrometry and full-field imaging. The spatial resolution attained with synchrotron UV/VIS luminescence microspectroscopy (SR-UV-LMS) setup was of 400 nm and allows recording luminescence features of localised particles of ZnO pigments, whose luminescence signal is buried at the macroscale. In parallel, images at 290 nm projected pixel size were obtained using synchrotron UV/VIS luminescence full-field spectro-microscopy (SR-UV-LFS) and allow highlighting the interface between two adjacent organic varnish strata of a cross-section from the *Provigny* violin by Stradivari (Fig. 28c) [148].

Promising applications of SR–UV/VIS multispectral luminescence microimaging can be foreseen for ancient materials. The high sensitivity and high spatial resolution attainable with SR-UV-LMS and SR-UV-LFS techniques allow complementary localisation and characterisation sub-micrometre heterogeneities within materials. In this perspective, a variety of new systems could be studied based on the characterisation of these heterogeneities: the study of micro-heterogeneities of

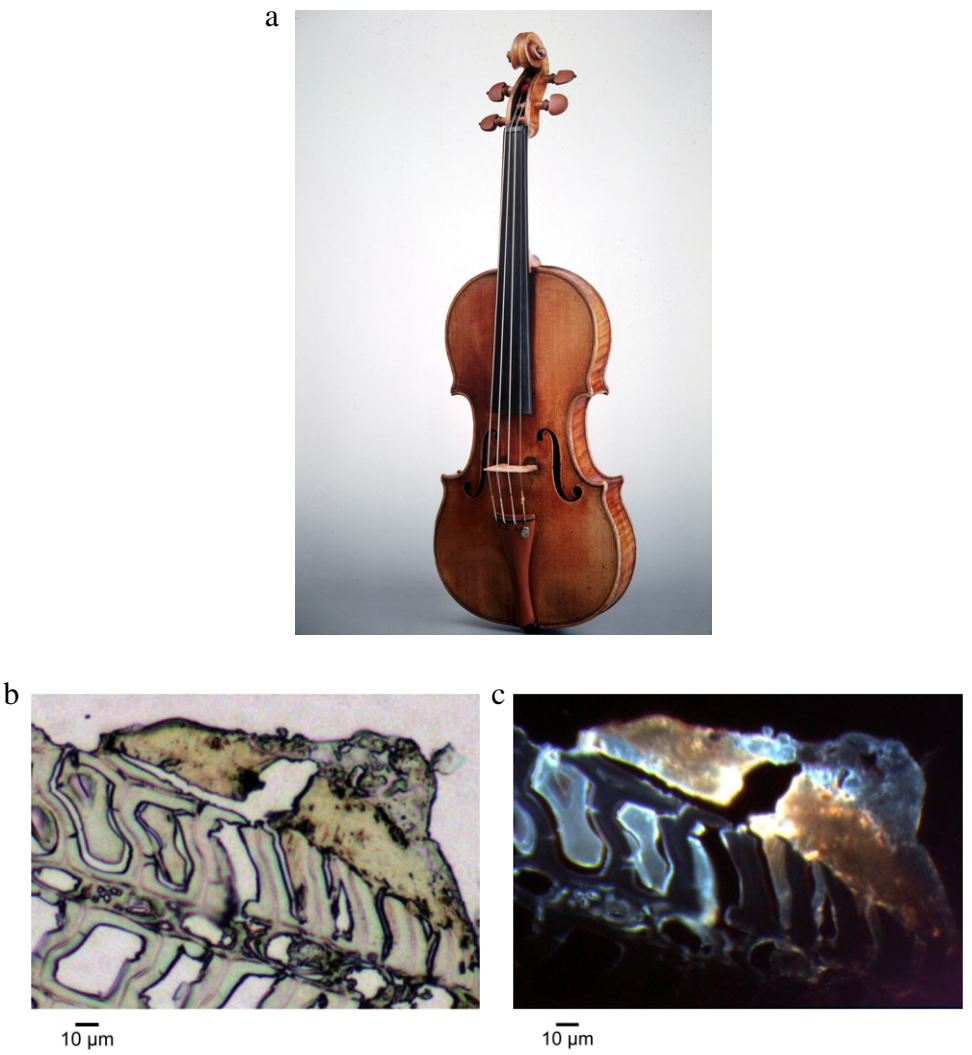


**Fig. 28.** SR–UV/VIS study of the finishing of the *Provigny* violin from A. Stradivari at the DISCO beamline, SOLEIL synchrotron (France). (a) Photography of the *Provigny* violin (Antonio Stradivari, 1716, Cremona, coll. Musée de la musique, Paris, inv. num. E.1730). Credits: Cité de la musique/J.-C. Billing. (b) Transmitted light microscopy image of a cross-section of a varnish from the *Provigny* violin by A. Stradivari, exhibiting several strata of organic binding media materials on top of spruce wood. (c) Reconstructed RGB full-field luminescence microscopy image of the cross-section; 340 nm excitation. Images collected band-pass emission filters centred at 500, 600, and 700 nm (all with 40 nm FWHM) (respectively 150, 45, and 120 s integration times) have been corrected from dark field and respectively attributed to the blue, green, and red channels [148]. (For interpretation of the references to colour in this figure legend, the reader is referred to the web version of this article.)

cultural heritage and archaeological materials, revealed by SR-UV/VIS multispectral luminescence microimaging, could be used as markers of their manufacturing process or of their degradation mechanisms, such as semiconductor-type pigments (in addition to ZnO: ZnS, $TiO_2$, CdS/Se, HgS, *etc.*) showing local crystal defects, or trace organic materials in fossilised samples, respectively. At last, in complex mixtures, the overall luminescence properties of materials observed at the macroscale do not account from luminescence from each luminophores. These distortions, resulting from optical interactions between materials or the disparity of quantum yields, can be uncovered at microscale by accessing to the luminescence of single particles or clusters of reasonably pure materials. Most interestingly, SR-UV/VIS multispectral luminescence microimaging can also be used to study the extrinsic properties of materials based on endogenous luminophores such as natural nanoprobes and contribute to the understanding of the degradation processes or chemical interactions between materials.

### *4.1.3. Towards synchrotron UV/VIS spectro-imaging setups and luminescence lifetime imaging*

Further developments of the synchrotron UV/VIS methodology based on the implementation of spectro-imaging detectors to attain high spectral resolution in the full-field mode have been initiated. This would provide collection of data with high spatial and spectral resolution and could be coupled to fluorescence lifetime imaging (FLIM).

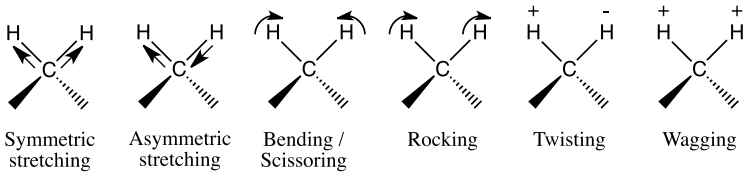


**Fig. 29.** Stretching and bending vibrational modes for a $CH_2$ group.

FLIM has mainly been used to highlight differences within Renaissance fresco painting of organic adhesives and plasters [149] using excitation in the UVA range (400–315 nm) at the macroscale in the field of conservation. As the temporal organisation of electrons in the storage ring consists of *bunches* it could be used to exploit this time structure of the synchrotron radiation for heterodyne FLIM [150, chap. 4]. Typically, using phase-modulation measurements, picosecond-long bunches of electrons generated at few hundreds of MHz would allow fluorescence and phosphorescence measurements with sub-nano temporal resolution to improve the spatial separation of luminophores in complex mixtures.

The improvement of the spectral, spatial and time component resolution are key parameters to refine the interpretation of the intrinsic luminescence properties of species within complex mixtures. Furthermore, it could allow evaluating the effect of the micro-environment (pH, polarity of the medium, aggregation state of the luminophore, etc.) on the temporal characteristics of submicrometre sized particles. Consequently, additional information could be provided on the (extrinsic) physico-chemical properties of local environments surrounding the considered luminophores. Particularly in the case of ancient materials, this would provide novel information on their degradation processes.

### 4.2. Synchrotron infrared spectroscopy and related techniques

#### 4.2.1. Basic principles

The principle of Fourier-Transform Infrared (FT-IR) spectroscopy relies on the excitation of vibrations (length stretching or angle bending) of molecular groups. The term $E_v$ in Eq. (36) is related to nucleus vibrations, therefore to the nucleus nature (namely mass) and arrangement (Fig. 27a). A simple model for stretching vibrations consists in describing a covalent bond as a simple harmonic oscillator, where two atoms of masses, $M$ and $m$, are connected with a spring of strength $k$. According to Hooke's law, the frequency of the vibration of the spring, $\nu$, is related to the masses ($m$ and $M$) and $k$ by the following formula:

$$\nu = \frac{1}{2\pi}\sqrt{\frac{k}{\mu}} \quad \text{where} \quad \mu = \frac{mM}{m+M}. \tag{39}$$

This simple model works well for simple diatomic molecules. It can give some basic feeling about how atom nature and chemical bonds will affect the stretching vibration frequency. However, the problem is much more complex in the case of polyatomic ($n > 2$) molecules. Fig. 29 represents the stretching and bending vibrational modes for a $CH_2$ group. Bending vibrations occur at lower frequencies.

As Raman spectroscopy, FT-IR spectroscopy is a quite classical method for the characterisation of ancient and historical materials [151,152]. A major advantage is the versatility of this technique which can probe almost any kind of materials (metals, glasses, paintings, wood, paper, textile, human remains…), as well as artefacts made of mixtures of such materials. More particularly, it can simultaneously probe organic, inorganic, as well as hybrid materials. For this reason, it is extensively used to study products resulting from controlled or long term reactions of organic binders with mineral pigments for example in cosmetics [153] or in paintings [154,155]. A second advantage of FT-IR spectroscopy is its non-invasiveness. Accordingly, it is increasingly used, in particular with portable instruments, directly onto objects, in museums or archaeological sites. In parallel to the development of such compact and easy-to-use instruments, another path was followed towards FT-IR microscopy. Combining an FT-IR spectrometer with a microscope makes possible the acquisition of 2D chemical maps, which allows not only the identification of ingredients in complex mixtures, but also their localisation.

The installation of such FT-IR microscopes on synchrotron sources was a major step in the direction of improved lateral resolution. The apparent brightness of SR can be 2–3 orders of magnitude higher than that of a Globar source. This enables to achieve significantly greater lateral resolution (typically close to the diffraction limit) with superior signal-to-noise ratio while keeping reasonable acquisition times. SR-based FT-IR microscopy is therefore mainly exploited to image complex structured compositions, at lateral resolutions of a few microns. Applications in the field of cultural heritage have recently been reviewed elsewhere [17,19].

#### 4.2.2. Trends in Fourier-transform infrared spectroscopy

Paintings are the most studied artistic materials. Indeed, the possibility to identify and map simultaneously almost all the painting ingredients (oil, glue, varnishes, wood, canvas, pigments, fillers, grounds, driers) with a micrometric probe is particularly well suited. Fig. 30 shows a demonstrative example, with the simultaneous identification of pigments (here,

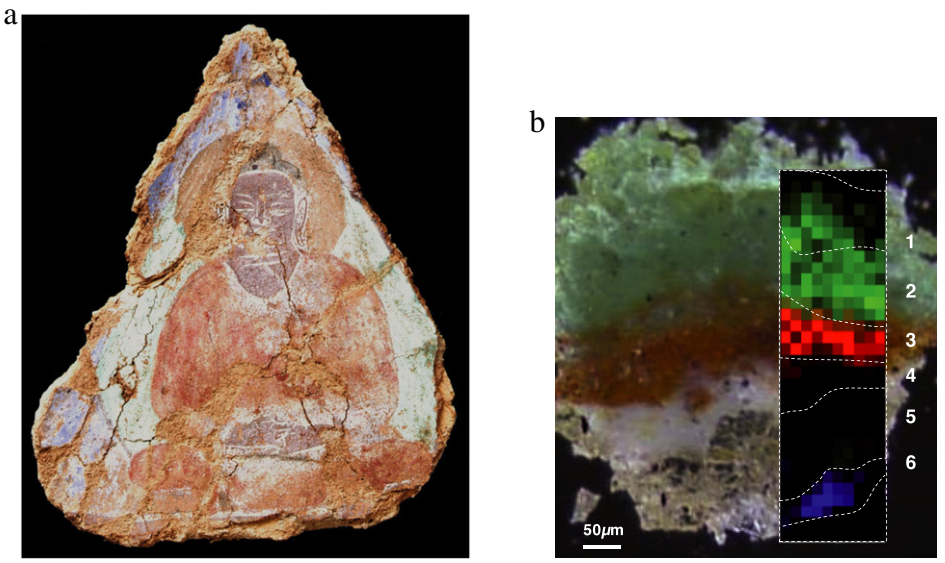


**Fig. 30.** (a) Fragment from the Buddhist wall paintings at the Foladi site (cave 4, sample 18) [156]. (b) Chemical mapping of ingredients in a painting fragment. The visible picture highlights a complex stratigraphy, with 6 successive layers. SR-based FT-IR microscopy reveals the composition of each layer. Highlighted here: goethite (*red*), metal carboxylates (*green*), and resin (*blue*). (For interpretation of the references to colour in this figure legend, the reader is referred to the web version of this article.)

a red pigment containing goethite $\alpha$-FeO(OH)), organic binders (here, a resin used in ground layer) as well as hybrid compounds (here, copper and lead carboxylates resulting from the reaction of oil with a metallic base). This fragment comes from Buddhist wall paintings at Bamiyan (dated from ca. 5th–9th centuries) where the key discovery was indeed the presence of oil [56]. More recently, a similar approach was followed for the elucidation of the composition of the varnish strata covering Antonio Stradivari's and contemporary violin-makers' instruments [157,158].

Lebon, Reiche et al. studied the long-term alteration of bone in archaeological settings, focusing at the relation between the complex supramolecular hierarchical structure of bone tissue and the spatial heterogeneity of diagenetic alterations [159,160]. Chemical variations in fossil bones at the microscale can be studied using synchrotron FT-IR, focusing at the micrometre-scale distribution of absorption features from the collagen (from the amide I band, 1645–1690 $cm^{-1}$), $\nu_1\nu_3PO_4^{3-}$ (1020–1100 $cm^{-1}$), $\nu_2$ and $\nu_3$ from $CO_3^{2-}$ (850–900 and 1415 $cm^{-1}$, resp.), $HPO_4$ bands. High resolution FT-IR spectro-microscopy provides spatially-resolved indications on the level of crystallinity of the bone, and allows to map preserved collagen and biogenic carbonates. Here again, sample preparation of extended thin cross-sections of typical thickness 2 $\mu$m is a key issue in order to be able to connect the taphonomic alteration observed with the histology of the bone (Fig. 31).

#### *4.2.3. Fourier-transform infrared imaging using Focal plane array detection*

In parallel to the increasing use of high-resolution SR-based FT-IR microscopy, a recent trend is observed in laboratories with the development of FT-IR imaging methods based on the use of focal plane array (FPA) detectors. Above the diffraction limit, The lateral resolution is no longer determined by the beam size itself, but by the detector projected pixel size. A further improvement can be achieved by the use of ATR (Attenuated Total Reflectance) objectives [161]. Typical IR-sensitive FPA detectors include 64 × 64, 128 × 128, and 256 × 256 elements, offering a major advantage in terms of total acquisition time, since spectra are collected simultaneously over the complete field of view. Such systems based on Globar sources are increasingly used for the study of paintings [162], and represent a good alternative to synchrotrons for mapping systems at a 10 $\mu$m-lateral resolution [152]. Very recently, these two different approaches (SR-based microscopy and FT-IR imaging) merged, with the development of SR-based FT-IR imaging instruments [163]. This requires the combination of multiple synchrotron beams to create a homogeneous beam over the field of view (Fig. 32). This set-up has primarily been employed for the study of biological samples, with observable features down to 0.5 $\mu$m. A first analysis of model painting fragment has been recently reported [164]. No doubt that applications to artistic and ancient materials will follow.

## 5. Discussion

We discuss here some of the main issues at stake and recent developments observed regarding the synchrotron-based characterisation of ancient and historical materials. In particular, we focus on those areas where improvements are foreseen in terms of methodology (spectro-imaging, nano-imaging, organic analysis, combination of techniques,

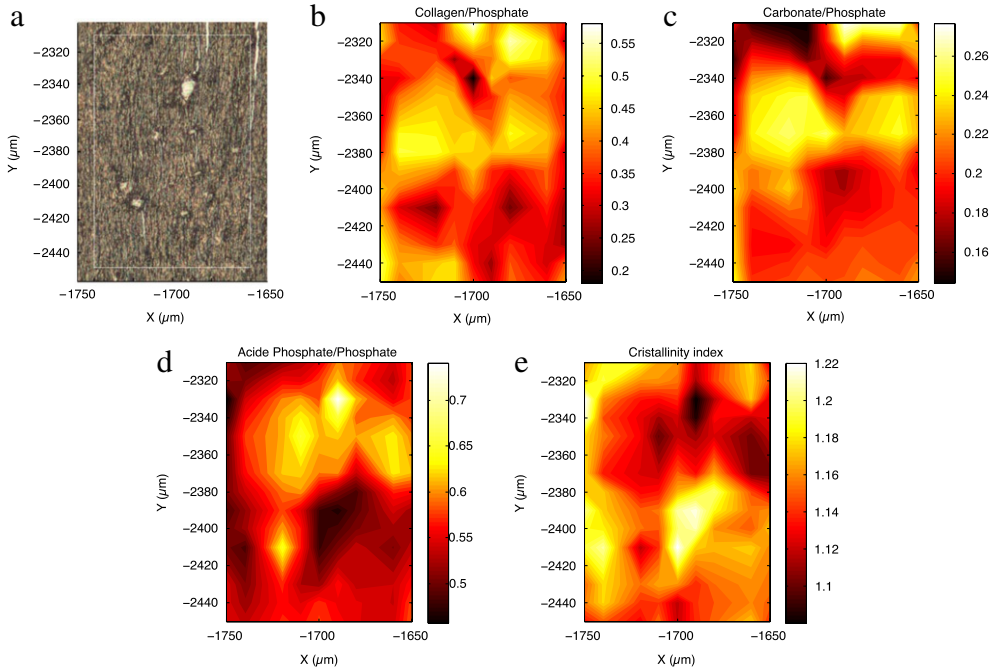


**Fig. 31.** (a) Light microscopy image of the microtomy cross-section of an archaeological bone sample (BZ-O30-17, dated 15,000 BP) from the Bise-Tournal site (Aude, France). The square indicates the area that was mapped using FT-IR raster-scanning micro-spectroscopy at the SMIS beamline, SOLEIL synchrotron (France). (b–e) colour-coded FT-IR maps presenting the spatial distribution of (b) the collagen to phosphate $PO_4$ ratio, (c) the carbonate $CO_3$ to phosphate ratio, (d) the acid phosphate $HPO_4$ to phosphate ratio, and (e) the crystallinity index derived from the ratio between the absorption intensities at 1060 and 1075 $cm^{-1}$.
*Source:* Reproduced with permission from Lebon [159].

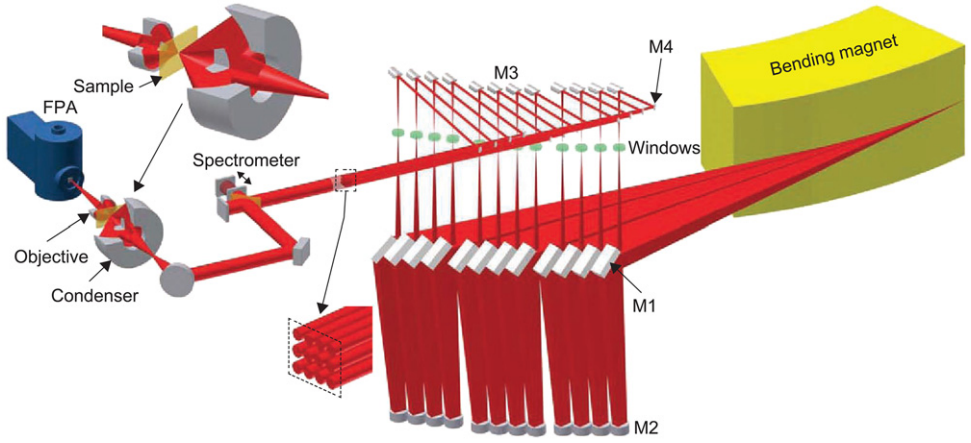


**Fig. 32.** Sketch of the experimental setup for FT-IR imaging using a multibeam synchrotron source coupled to a focal plane array detector, developed by Nasse et al. at the *Wisconsin Synchrotron Radiation Center* [163].

non-invasive characterisation, time-resolved measurements) taking into account on-going instrumental development. Mitigation strategies to prevent radiation damages are discussed, as well as specific support initiatives at synchrotron facilities.

### *5.1. New approaches bridging micro-/nano-focused spectroscopy and full-field imaging*

Ancient materials studies would greatly benefit from high spatial resolution low-noise measurements carried out on large sample areas. Today this can primarily rely on a tighter association between micro-spectroscopy and full-field imaging.

Improving the complementarity and the switch between fast raster-scanning micro-spectroscopy and full-field imaging approaches may lead to interesting developments for the study of ancient and historical materials. Full-field imaging provide *spatial information plus some spectral information* therefore allowing for the visualisation of regions of interest (ROIs) at high spatial resolution within large sample areas, typically leading today to megapixel multispectral images. Conversely, micro-spectroscopy mapping provides *spectral information plus some spatial information*, most often leading to far higher signal-to-noise high spectral resolution data, at the expense of orders of magnitude longer collection times. Both data collection modalities therefore today provide complementary ways to collect $I(x, y, (z), E_0, E, \ldots)$ maps.

A first expected evolution of interest for ancient materials studies might be the optimisation of joint data collection strategies in order: (1) to select more easily the most representative ROIs, (2) to decrease the time spent to adjust the sample position, (3) to decrease the dose to the sample under study including during the positioning step.

Beyond these adaptations, *spectro-imaging* is expected to bring additional capabilities for the SR-based study of ancient materials by enabling collection of high-resolution spatial and spectral information on large areas within a reasonably short timeframe. As stated before, at synchrotrons, the high brightness of the infrared photon beam has primarily been exploited for raster-scanning micro-spectroscopy. Only recently have Nasse et al. reported the implementation of a FPA system at a beamline of the *Wisconsin Synchrotron Radiation Center* coupled to an array of mirrors to increase the beam footprint [163]. In the ultraviolet/visible range, we have recently shown the interest of joint full-field imaging and micro-spectroscopy UV/visible luminescence studies of historical materials using a synchrotron source; the development of synchrotron UV/visible spectro-imaging is under way [148]. In the X-ray domain, the recent development of full-field XRF energy-dispersive pixel area detectors — such as the pnCCD *Colour camera* that was coupled to a *camera oscura* [165] (Fig. 7h — may well bring the same situation to SR-based X-ray fluorescence, and novel developments are taking place in full-field XANES imaging (ref. Section 3.3.4). Currently, the main limitation is the limited counting rate compared to classical XRF detectors, as well as the limited detector surface that can be produced. Indeed, the development of spectro-imaging strongly relies on detector development. The perspective to tighter define energy thresholds in pixel area X-ray detectors will also add to some extent multi-, if not hyper-, spectral capabilities. Another current limit is the lack of efficient and stable high-energy pixel detectors, namely CdTe-based [166], which on-going development is crucial for core ancient materials needs. Spectro-imaging therefore exists, at least at the pilot stage, for most spectroscopic methods of interest for the study of ancient materials.

Interestingly, when the spatial resolution attained using spectro-imaging is comparable or better than the characteristic length scale of heterogeneity of the property studied, the analysis can be conceptually compared to that obtained through separative techniques—based on time-of-flight, retention time, mass separation, in turn connected to $m/z$ ratios, volume exclusion, chemical affinity, *etc.* Here, the *in situ* spatial separation is inherent to the material raw constituents, their subsequent chemical modification and alteration, and is therefore comparable to an *in situ* 2D thin-layer chromatography (TLC), here based on the intrinsic and extrinsic history of the material that has induced local segregation or aggregation of chemical compounds. Using separative techniques, high level of discrimination of the many possible compounds is attained through the coupling of separation and detection modalities (GC/MS, HPLC/DAD, *etc.*) whereas, in the case of spectro-imaging a comparable result is achieved through the combination of mostly independent information from coarser spectral signatures and high-resolution spatial localisation (Fig. 33).

### 5.2. Towards more synchrotron nanoscale characterisation of ancient materials?

We discuss here the interest and development of spatially-resolved SR-based methods to study ancient materials at a resolution below a few hundreds of nanometres. Methods (XRD, XANES) that are carried out with a macrobeam yet leading to information on the organisation and state of matter at nanometre length scales are out the scope of the current section. As discussed above (Section 2.2), most ancient materials show a strong heterogeneity at the micro- and nanoscale; however nano-resolved methods are still struggling to find a regular use in the study of these materials except in very specific cases. This is due to the fact that understanding the complexity of these materials at the micrometre length scale is already in most cases very challenging and that nano-characterisation imposes strong constraints on sample preparation, handling and sample environment. For instance, in the setting-up of the IPANEMA platform at SOLEIL, scientific communities have repeatedly confirmed their interest for micro- rather than nano-imaging and spectroscopy.

However, further development of nano-characterisation could bring more insight in the analysis of interfaces, mineral grains, crystal texture, nanoparticles (such as in lustred ceramics), *etc.* on which most often crucial information is required to understand past manufacturing processes, provenance, reactivity, *etc.* [167].

As synchrotron technology evolves and especially with the advent of next generation sources, it will be possible to perform X-ray investigations with unprecedented resolution of a few nanometres. Today maximum available resolutions are typically in the 30–50 nm range at medium/hard X-ray beamlines. While inferior to the resolution of electron microscopes, X-rays offer the advantage of being able to penetrate matter, thus allowing to image buried nano-structures and objects in solution, and are often less damaging [168–170].

Nanoscale experiments require a high technological effort, not only on the X-ray instrumentation, but on the whole experimental infrastructure. The setup needs to be isolated against vibrations, air conditioning is required to maintain the temperature very stable without inducing turbulences, and interferometric systems may be used to compensate the mechanical instabilities of the positioning setup. This therefore tends to limit the adaptability of sample environments.

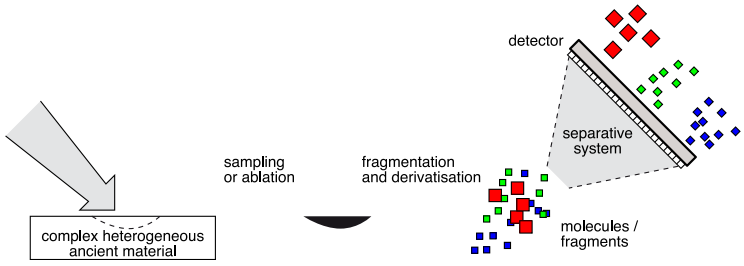


(a) Separative characterisation.

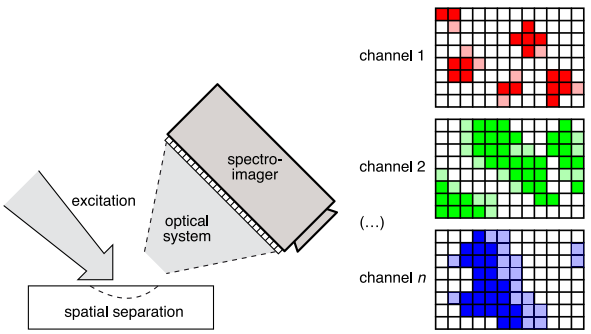


(b) Spectro-imaging below the characteristic length scale.

**Fig. 33.** Schematic representation of the separation obtained from complex heterogeneous ancient materials: (a) using separative techniques where the discrimination is based on highly specific signatures of the fragments: $m/z$ ratio, steric volume, polarity, chemical affinity with the matrix of the 'separative system'. Separation and detection usually involve the combination of several information levels. When the system is optimised, unique molecules may be unambiguously differentiated. Except in specific cases, such as ion or laser-based local ionisation, the high spatial resolution information from the original material is lost; (b) using spatially-resolved spectro-imaging where discrimination between species results from a *combination of the spectral signature and the high-resolution spatial localisation*. In itself, the spectral signature, is usually far less discriminant than that obtained with separative methods. However, mixed species with a varying composition ratio over the obtained map may be discriminated. Co-localisation, or on the contrary spatial discrimination, results from the properties of the original raw material (trace elemental segregation, mineral paragenesis…), from the manufacturing process, from alteration features, *etc.* Co-localised species with similar spectral signatures may not easily be discriminated. This approach can apply to organic, inorganic and hybrid nature compounds.

In order to perform nanoscale measurements on ancient materials, sample preparation is a key step. To gain meaningful information it is often important to work with submicrometre thin cross-sections, as required for instance for TEM characterisations. This requires the use of ultramicrotomy or ion-beam milling, which not only implies expensive equipment but also experience in the technology and in each material. In-depth pre-characterisation by non-destructive techniques including standard light microscopy is crucial to understand the sample and select regions of interest to be imaged during the SR experiment. However, to reach such exceptional resolutions very high flux densities have to be applied to samples, which somewhat limits the use of the technique for radiation-sensitive samples (Section 5.8), particularly in energy ranges where the absorption cross-section is high (VUV, soft X-rays).

Potentially more importantly, spatially-resolved area detectors today of $100 \times 100$ to $10,000 \times 10,000$ pixels in the X-ray, infrared and UV/visible ranges will typically span 2 to 4 orders in length scale (Section 5.1). For instance, in the UV/visible range, we recently imaged systems of several hundreds of micrometres in lateral dimensions with a projected pixel size smaller than 500 nm [148]. We also mentioned earlier novel developments in full-field XRF (Section 3.2.4) and full-field XANES (Section 3.3.4), typically covering the same range in length scales. Hyperspectral imaging may therefore provide the missing link from nano- to sub-millimetre scales by allowing providing information at these successive length scales altogether.

### *5.3. Prospects in the synchrotron characterisation of the organic fraction of ancient and historical materials*

X-ray synchrotron techniques were until recently used primarily to characterise high-$Z$ elements in low-$Z$ matrices due to the fact that: (1) the photoexcitation cross-sections of low-$Z$ elements are low at the typical high energies used for multi-elemental analyses, (2) non-radiative de-excitation (Auger and Coster–Kronig processes) predominates until $Z = 30$ therefore hampering bulk analyses, (3) X-rays fluoresced by low-$Z$ elements are very soft and are therefore absorbed very efficiently by the matrix and by air, and detected with difficulty.

Table 3 summarises the main methods of interest for the characterisation of organics compounds in ancient and historical materials. The development of synchrotron soft X-ray and FT-IR spectroscopy techniques allows for novel capabilities in

**Table 3**
Characteristics of the main synchrotron-based methods providing information on the organic fraction of ancient materials.

| Synchrotron method | FT-IR (mid-IR) micro-spectroscopy | UV/visible micro-spectroscopy | STXM | Small X-ray scattering | Phase-contrast μCT |
|---|---|---|---|---|---|
| Physical origin | Vibration and rotation modes of interatomic bonds | Allowed electronic transitions in the eV range | Photo-excitation of core shell electrons | Mesoscale structure | Elastic scattering |
| Main observable compounds | IR-active compounds: organics, *etc.* | Intrinsic and extrinsic luminophores: conjugated systems, *etc.* | Low-*Z* elements containing materials | Nano-structured and hierarchical materials | Low-*Z* elements containing materials |
| Sample preparation requests | Transm.: 0.5–5 μm thin sections Refl., ATR: flat surface | Flat surface | Thin section $<$ 100 nm | Sample must transmit X-rays (typ. 0.1–1 mm thickness) | Stable sample with sufficient X-ray transmission ($>$30%, preferably $>$60%) |
| Typical detection limit | 5–100% | traces–100% | 10–100% | NA | NA |
| Typical achievable spatial resolution | 4–10 μm | 300–500 nm | 25–40 nm | 1–100 μm | 1 μm |
| Frequency of use reported in the past 5 years in the field | *** | * | ** | * | ** |

molecular identification and speciation of organic materials [171,172]. As pointed above (Section 4.1), recent developments include the synchrotron UV/visible spectroscopy of organics [148]. Generally speaking, these techniques will provide signatures corresponding to classes of compounds from characteristic photo-excitation and electronic transitions (X-ray, UV/visible) or vibrational/rotational (IR) features, which need to be coupled to further non-invasive or invasive (such as GC/MS) techniques for better identification. The selectivity achieved is generally orders of magnitude lower than that attained with separative techniques. However, SR imaging methods jointly provide spatial information and molecular speciation, and therefore can also provide enhanced separation as pointed out before (Section 5.1 and Fig. 33). They are therefore very useful complements to methods such as TOF-SIMS [173]. In the infrared and UV/visible ranges, diffraction-limited resolution can be attained in the spectroscopy of organic compounds [148,174,175].

Using scattering techniques, small-angle X-ray scattering can be used to characterise the macromolecular organisation of organised organic materials such as textile fibres [84–86]. Phase-contrast X-ray imaging, exploiting the refraction of the X-ray beam at internal material boundaries rather than its absorption, is also an appropriate tool for the characterisation of organic samples. In fact, for low-*Z* materials the phase shift, resulting in beam refraction, plays a more prominent role than the attenuation because $\delta$ is typically 3 orders of magnitude larger than $\beta$. In particular, for a multi-component specimen, the relative differences in angular deviation arising from the phase shift are larger than the corresponding relative changes in beam intensity, which are the basis of traditional absorption-based X-ray imaging. As a result, phase-contrast techniques are valuable tools for boosting the often insufficient observed contrast for this type of samples.

These developments therefore appear particularly promising for the synchrotron-based study of the organic fraction of ancient and historical materials, but also as the opportunity to better combine information from organic and inorganic fractions, that addresses a key need for the study of ancient material most often of hybrid or composite nature.

### 5.4. Combination of characterisation techniques

The ability to combine techniques – SR-based altogether, and SR- with non SR-based – providing various information on the same point, area or volume of analysis is essential to study complex heterogeneous ancient materials. Three main approaches were reported: (1) the direct coupling at the same endstation of distinct micro-characterisation methods on the same spot of analysis such as the widely observed *golden X-ray trio* XRF, XAS and XRD, but also X-ray techniques with Raman spectrometry [176,177], (2) the accurate repositioning of the same sample on different instruments for spot analyses, and (3) the *a posteriori* spatial registration (or *alignment*) of the collected data from different instruments. The latter generally involves calculations to correct movements of the sample relative to the detectors, possibly differing pixel sizes, as well as optical distortions and aberrations. Full-field techniques (e.g. X-ray tomographic microscopy) could also be used as a tool to quickly get the overview of a sample and therefore better select regions of interest for other micro-characterisation analyses, even before sample extraction.

When combining techniques, the analytical sequence needs to be optimised to avoid perturbation of following measurements by earlier ones, and to optimise the exploitation of the output of previous measurements for further analyses.

**Table 4**
Characteristics of the main synchrotron-based methods used to study entire ancient artefacts and specimens. (*) Note that in full-field mode when working in parallel beam geometry, object dimension $D$ is directly related to the pixel size $d$ through the number of pixels $n$, as $D = n \cdot d$.

| Synchrotron Method | Deported FT-IR spectroscopy | XRF macro-scanning | $K$-edge subtraction imaging | μCT, laminography | High-energy XRD |
|---|---|---|---|---|---|
| Physical origin | Vibration and rotation modes of interatomic bonds | Photo-excitation of core shell electrons | Photo-excitation of core shell electrons | Photo-excitation of core shell electrons | X-ray scattering |
| Typical objects studied | Surface of metal artefact [154] | Paintings, flat fossils | Paintings | Fossils, building stones, small archaeological artefacts | Ceramic sherds, paintings |
| Typical object size | NA | $m^2$ | $m^2$ | $mm^2$–$m^2$(*) | $cm^2$ |
| Probed depth | surface | subsurface | bulk | bulk | bulk |
| Frequency of use reported in the past 5 years in the field | * | ** | * | *** | ** |

Different high-resolution techniques might probe different spot sizes and/or sample depths and might not be completely comparable, and complex correction might be needed regarding for instance matrix effects. Typical examples include the combination of laser spectroscopy and SR techniques, in which the spot sizes of the laser and the X-ray beam have to be carefully matched. But also techniques using the same primary beam, like XRD and XRF might suffer from the difference in probing depth, as the lower energy fluorescence photons might not escape from deeper sample layers.

When using the direct coupling or repositioning approaches, sample preparation and sample mounting also has to be considered. The different analytical techniques do not share the same constraints regarding sample preparation. Some will probe the entire sample thickness, while others will be selective to the surface. Some will be sensitive to elements, molecules or phases, therefore they will not be sensitive to the same contaminants. For instance, FT-IR analyses in transmission require thin samples, placed on IR transparent substrate (typical $BaF_2$, diamond, or ZnS window). The presence of organic embedding resin could complicate the analysis of organic original ingredients. Conversely, for XRF analyses, such organic materials are usually not critical, providing that they do not contain any high-$Z$ element which could contribute to XRF emission. Therefore, it is important to determine if the preparation of a single, versatile sample, will be more advantageous than the preparation of different samples, optimised for each technique. Advices regarding sample preparation for the analysis of painting fragments by combining FT-IR with XRF and XRD can be found elsewhere [178].

Data analysis techniques are an important point for any investigation, but can be especially important when dealing with multiple experimental methods probing the same sample. In most cases each technique is analysed individually. Modern statistical techniques can profit from correlations within the different data sets and help considerably in the extraction of information and the interpretation of data. However, this requires software capable of unifying different experimental data sets. Currently, few such programs exist and these are limited to commonly combined techniques. In addition, the researcher doing the data analysis must be callable of interpreting all the techniques used. As combined techniques become are more commonly used more effort is put into the creation of multi-technique data processing. One example is the PyMCA program [179] developed at the ESRF.

Compared to the more usual trace elemental analyses, elaborate signatures based on associating the various datasets can then be designed, able to provide more complete answers to questions such as provenance and ancient manufacturing techniques. This may be seen as an extension of the key concept of trace for archaeometric studies, aggregating all spectroscopic information.

### 5.5. Non-invasive synchrotron study of entire objects

Non-invasive characterisation may be preferred when studying unique and/or valuable heritage artefacts or palaeontological specimens. Table 4 summarises the main synchrotron-based micro-spectroscopic methods used to study entire ancient artefacts and specimens non-invasively. We establish here a clear distinction between experiments that are performed *non-invasively*, i.e. without having recourse to further sampling of the original object, fragment or sample, and those performed *non-destructively*, i.e. not damaging the sample or the object and, more specifically in the context of an analytical sequence, not hampering downstream measurements. This definition of non-invasiveness also applies to the study of pre-existing fragments of objects or protrusive parts, often of smaller thickness than that of the rest of an object. However, one should mention that current non-invasive methods do not reach by far the level of sensitivity (elemental, chemical, structural) provided by invasive methods and are not today yet a full alternative to understand the complexity of ancient materials. In addition, moving a fragile historical object to perform *non-invasive* characterisation such X-ray radiography or CT may sometimes result more damaging to the object than micro-sampling it in very controlled condition.

As shown on Fig. 10, the mean free path of photons at $100\,eV < E < 20\,keV$ is typically below 100 μm in transition metals, 1 mm in typical archaeological ceramic and 1 cm in purely organic compounds. Ancient materials are rarely of purely organic

nature even when it is originally the case, as taphonomic and ageing processes will generally bring heavier elements within aged materials. Below 20 keV, X-ray methods will therefore be limited to surface or sub-surface characterisation. This is also the case for most materials in the infrared and UV/visible range where the typical length of penetration may not exceed a few micrometres or tens of micrometres. In such conditions, on many ancient artefacts, the altered state of conservation of outer strata will be an additional strongly limiting factor for non-invasive synchrotron (and benchtop) infrared, UV/VIS and X-ray characterisation. For this reason, the vast majority of ancient materials studies using synchrotron sources has thus far been performed invasively on micro-samples.

However, the situation differs at the two far ends of the energy spectrum of photons delivered at synchrotron sources.

Above a few tens of keV, centimetres or tens of centimetres of materials can be crossed in transmission geometry with scattering (e.g. for hard X-ray powder diffraction) and photo-excitation-based techniques (e.g. with hard X-ray microtomography, laminography or X-ray fluorescence). In the field, specific sectors of ancient materials studies have particularly developed, the microtomography of palaeontological specimens, primarily after the seminal works by P. Tafforeau at the *European Synchrotron Radiation Facility* in Grenoble, France, as well as more recently the XRF macro-scanning of entire paintings (Section 3.2.4).

Far infrared radiations, particularly in the 0.1–2 THz range (0.4–8.3 meV or 3–67 $cm^{-1}$), can also cross centimetres of materials, allowing for the characterisation of inner features in entire objects without the ionising impact of X radiations. THz-pulse imaging has been tested using conventional far infrared sources on historical objects such as paint layers [180] and mummy soft tissues [181] with typical resolution in the 0.75–1 mm range. To our best knowledge, it has however never been tested using a synchrotron source on ancient materials.

The use of non-invasive methods to investigate thick samples usually requires 3D reconstruction to understand the depth profile of the sample and is therefore closely linked to the development of such methods. For samples with a complicated inner structure a full tomographic data set has to be taken. In simpler or more homogeneous objects the 3D information can be accessed with less effort by using confocal techniques. An example of this approach is the reconstruction of depth profiles by inserting spiral slits into the beam. This allowed the reconstruction of stress profiles in steel [182] or the depth-resolved *operando* observation of chemical reaction in fuel cells [183].

### 5.6. Time-resolved measurements

It may sound paradoxical to evoke time-resolved measurements when dealing with ancient materials that may have been 'stable' for long periods of time in their context. However, three main modalities are used and/or foreseen for the field:

- Measurements at characteristic time scales in the range between seconds to hours are major targets for fields such as the study of accelerated ageing, alteration processes, the effect of stabilisation and restoration treatments. Real time analyses have also already been used for the *in situ* temperature monitoring of reactions involved in artistic processes. As an example, Pradel et al. studied high temperature reactions in model lustre paint. The authors could correlate the decomposition of metacinnabar and the subsequent creation of a sulphur-reducing atmosphere with the reduction of $Cu^{2+}$-containing compounds to $Cu^{+}$; an intermediate chemical state that further leads to the formation of metallic Cu nanoparticles [184].
- The temporal component of some measures (such as the luminescence decay in FLIM) can be a tool to selectively record UV/visible luminescence signals from luminophores in heterogeneously mixed materials.
- Time resolution also provides a simple way to monitor radiation damages. Indeed, as most (not all) of the characterisation techniques involve a resonance at the absorption energy, radiation damage will result in changes in the signal. If they occur shortly after the start of the irradiation, observing the modification of the signal under the beam may be a good way to assess whether radiation damages are occurring or not.

For such time-resolved analyses, SR techniques offer not only fast data acquisition (thanks to the high flux attained) but also complex sample environment, such as electrochemical cells or furnace (thanks to the high penetration depth of X-rays).

### 5.7. Synchrotron methods not (yet) used to study ancient and historical materials

A huge potential seems to lie in a number of synchrotron techniques that could have direct implications for the study of ancient materials and have not or hardly been used thus far.

This includes methods that have only been scarcely used in the field.

Soft X-ray based techniques, such as STXM, TXM and to a lower extent X-PEEM, have attracted considerable interest in life and environmental sciences as they allow determining the speciation of light elements particularly carbon and oxygen from organic materials (particularly at the ALS and CLS synchrotrons), or working on *M* lines of transition metals, at spatial resolutions of a few tens of nanometres [171,185]. At such low energies — for instance, the carbon *K*-edge is at 280 eV — experiments require sample thicknesses in the 100 nm range, with requirements similar to those needed for transmission electron microscopy (TEM), and may require preparation such as focused ion beam (FIB) [186,187]. Particular developments are expected in the study of the alteration of organic materials (paper, wood, organic binders in paintings, *etc.*), or micro-organism induced degradation of archaeological and heritage materials.

The use of synchrotron (and conventional) X-ray μCT techniques is quite limited in archaeology and conservation sciences. Study of the consolidation of materials such as stone, glass and wood, as well as dendrochronological investigation used to date wooden artefacts are expected to develop in the years to come.

Synchrotron microbeam small angle X-ray scattering (μSAXS) allows a spatially-resolved investigation of the sample's mesoscale (see Section 3.4.3), namely in the 10–5,000 Å range. Although many ancient materials show interesting features of nanometre length scale, like nanoparticles or porosity or exhibit a hierarchical structure, like biological materials, this technique is hardly used.

On a longer term, additional synchrotron techniques appear particularly promising for ancient materials studies.

THz imaging capabilities, discussed in Section 5.5, may well find several applications in the field of ancient materials studies. An extension in IR spectroscopy towards the far-infrared domain is also observed using conventional sources, driven by applications in Space science. THz spectroscopy could also be highly valuable in the cultural heritage field, in particular for the analysis of inorganic compounds inactive in the mid infrared domain, such as some pigments or corrosion products. A first application to the study of 16th century Spanish paintings has recently been reported [188].

This is also the case for holographic or coherent scattering techniques that were developed to address the phase problem in XRD in the last years. Two main methods were developed to reconstruct the missing phases. In holography the signal emitted from the sample interferes with a reference wave [189–191]. Measuring the thus created hologram allows to reconstruct the complete wavefront emitted by the sample. However, this requires a large coherence length and is thus more readily achievable with soft and tender X-rays. The second method is phase guessing, in which no reference wave is used. Instead, just the diffraction pattern obtained by a fully coherent illumination of the sample is compared with one calculated from a model of the sample. An iterative algorithm then refines the electron density of the sample and the phases of the detected wave field [73,75,192,193]. The disadvantage of this technique is that *a priori* information is needed from the sample; in most cases an outline or *support* of the sample is put into the model. Ptychography [71,194,195] is very promising for real applications and has already been used to image microstructures from a computer chip [74] and soft matter [196,197]. This technique illuminates the sample with overlapping spots of coherent radiation. The information from these overlaps allows a much faster convergence of the reconstruction algorithm. In addition, this technique can be used to image a ROI, while other techniques need to reconstruct the full object. The disadvantage of all coherent diffraction techniques is the large amount of photons needed to attain high resolution [198], thus limiting its use to radiation-hard samples.

Finally, more use could be made of synchrotron surface/interface sensitive techniques, such as speciation obtained from photoemission techniques.

### 5.8. Radiation damage: mitigating, monitoring and studying

Third generation synchrotron sources are capable of delivering very high photon fluxes into the sample, especially when using focused beams. Potential radiation damages are particularly important in the X-ray and UV ranges of radiation, which are *ionising* radiations. For techniques that are applied invasively and/or with very small beam footprints, damage may not result in a visible alteration of the original objects, particularly museum objects. However, a main worry here is the possible loss of information, or worse misleading information, that could be retrieved from a radiation-damaged spot. For instance, photoreduction or oxidation can lead to local changes of speciation, and further lead to full misinterpretation of the data. For this reason tracking radiation-induced changes may prove as important as introducing mitigating measures.

For instance, X-ray beam fluxes are typically in the $10^{12}$–$10^{14}$ ph $\cdot$ $s^{-1}$ $\cdot$ $mm^{-2}$ range or higher at the sample position, i.e. in the 0.01–1 ph $\cdot$ $s^{-1}$ $\cdot$ $Å^{-2}$ range. On the only series of experiments known to the authors using synchrotron UV/VIS luminescence measurements on ancient materials, at 280 nm the irradiance at the UV/VIS synchrotron microspectroscopy beamline was comparable to that obtained with a 450 W Xenon lamp in the same bandpass. The high spectral irradiance of the UV/VIS synchrotron generated beam can be compensated by its high monochromatisation. Valence electrons, located in outer energy levels, induce photo-electronic transitions in the 200 nm–1.2 μm range (1–6 eV). In the UV range, the 200–380 nm region corresponds to bond energies from 140 to 70 kcal $\cdot$ $mol^{-1}$ respectively, typically found in organic and inorganic compounds. Organic materials show a greater number of photo-induced reaction pathways from the excited state than inorganics, such as photoxidation or photoreduction phenomena induced by the chemical reactivity of the excited state generated by light absorption, or intramolecular photoreactions during which photochromism or internal energy transfer may occur. All these pathways are responsible for the chemical changes of a material or its close environment.

Organic materials, such as textile fibres and paint binders, are most sensitive to radiation damage, while metals may be radiation-hard to even the highest SR fluxes. Radiation damage is a very complex phenomenon and types of material may react to it in very different ways. The damaging properties of a radiation beam depend on its energy, on the photon flux and on the experimental conditions (e.g. temperature, humidity, etc). *Direct damage* is created by the absorbed photons themselves, for example by photochemical reactions or ionisation, or by secondary particles like photoelectrons. Conversely, *indirect damage* is created by photons that react with the environment of the sample, creating aggressive moieties such as HO• radicals in water and ozone in air. These indirect processes are often more damaging than direct ones, but can be reduced by using inert atmospheres and cooling of the sample.

X-rays have energies high enough to ionise matter and can damage the material directly by creating fast electrons via the photoelectric and Compton effects. These electrons react via secondary electron cascades and may therefore destroy molecular bonds in the sample. For more information see [82,83,199]. Irradiation can also create point defects in semiconductors or isolators, which create new states in the energy gap of the material [200,201]. These defects are called "colour centres" because they lead to a darkening of transparent objects. This includes a group of cultural heritage materials like glasses [200,201], teeth [7], pigments and soft tissues. These optical degradations may be partly reversible. For instance, it is possible, at least to some extent, to remove the radiation marks on teeth [7] and glasses by subsequent UV irradiation.

The simplest way to minimise radiation damage is to use high quantum efficiency detectors, an efficient background reduction to lower the necessary radiation dose and appropriate shutters, pre-characterisation and pre-alignment procedures to limit the irradiation time. For instance, in X-ray tomography, which is especially prone to radiation damage induced artefacts, two different methods have been developed to reduce the impact of the damage. The first aims at performing the tomogram ultra-fast with particularly sensitive detectors. In this way, it is often possible to complete the tomogram before the radiation damage leads to visible degradation. The other approach uses phase contrast at high X-ray energies. Since the absorption drops faster than the refraction with increasing energies (except at absorption edges) this increases the signal/damage ratio of the experiment.

Reducing the intensity of the primary beam is usually counter-productive since a longer exposure time is needed. This does not limit the direct radiation damage but allows the indirect damage to work over a longer period of time.

In addition to mitigation procedure, a stronger focus could be put on monitoring. On top of monitoring the signal change itself over time, integrating complementary techniques at a beamline, like FT-IR, colourimetry, UV/VIS or Raman spectroscopy can allow the *in situ* determination of radiation damage and improve the acquisition quality for damage types that can be detected with these techniques.

In general, the assessment of invisible radiation damages is more difficult. Many organic materials, like fibres of parchments and canvas, suffer a loss of structural order when subject to high radiation doses. Although this leaves no visible mark on the sample, the danger of long-term degradation has to be considered. Unfortunately, few information is available to this time, and systematic methodological studies have yet to be performed [202]. This should lead to clear indication which radiation doses are tolerable on a given material.

It is important to note that radiation damage in general does not heal out over time and hence the radiation exposure of a cultural heritage object or sample accumulates over successive treatments and should be carefully archived. Unfortunately, this information appears insufficiently recorded and made available for the time being. Procedures could be implemented for important palaeontological specimens and heritage samples to allow recording and storing the information on the potentially altering experiments performed on these sample and objects.

### *5.9. Perspectives for specific support at synchrotron facilities*

Dedicated projects developed at synchrotron facilities are expected to facilitate the study of ancient and historical materials. This includes initiatives such as the *Heritage science unit* (M. Pantos, CCLRC, 2003–2008) at SRS Daresbury, the IPANEMA platform (*Institut photonique d'analyse non-destructive européen des matériaux anciens*) at synchrotron SOLEIL and the *Initiative in Palaeontology* at the ESRF, Grenoble. For example, developments of the IPANEMA platform at SOLEIL focus on supporting experiments and developing research activities in instrumentation and data processing optimised to the needs of ancient materials. Support of synchrotron experiments may include support to project definition, sample preparation, adaptation of experimental setups, data collection and data processing. A particular focus is aimed at studying series or collections of objects which are often more relevant to the field than case studies on individual artefacts. The setting-up of the platform aims at facilitating interactions with scientists, as well as end users, such as conservators and archaeologists, including by organising training sessions [24,203].

## Acknowledgements

The authors acknowledge critical reading by S. Hustache (synchrotron SOLEIL) and É. Anheim (UVSQ), and rereading of the presentation of their work by St. Leroy (IRAMAT, Saclay), S. Bernard (Muséum National d'Histoire Naturelle, Paris), Ph. Sciau (CEMES, Toulouse) and P. Tafforeau (ESRF, Grenoble). The Bamiyan painting study was funded by grants from ESRF (Project EC-101). The authors are grateful to Y. Taniguchi (NRICP) for active collaboration, to the Ministry of Information and Culture of Afghanistan for their kind assistance and UNESCO/Japanese Funds-in-Trust for funding. The authors thank the team at DISCO (M. Réfrégiers, Fr. Jamme) on which the UV/VIS experiment was set-up in the context of a project associating the Cité de la Musique (J.-Ph. Échard) in Paris. The IPANEMA platform at SOLEIL is jointly developed by CNRS, the French Ministry of Culture and Communication, MNHN and NWO, and benefits from a CPER grant (MESR, Région Île-de-France). The authors acknowledge the financial support by the Access to Research Infrastructures activity in the 7th Framework Programme of the EU (CHARISMA Grant Agreement n. 228330).

## Appendix A. Acronyms and abbreviations used

See Table A.1.

**Table A.1**

| | |
|---|---|
| ATR | Attenuated total reflectance |
| BM | Bending magnet |
| BP | Before present, taken as 1950 AD |
| CCM | Channel-cut monochromator |
| CRL | Compound refractive lenses |
| CT | Computed tomography |
| DAD | Diode array detector |
| DCM | Double crystal monochromator |
| DMM | Double multilayer monochromator |
| EDS/EDX | Energy dispersive X-ray spectrometry |
| EUV | Extreme ultraviolet |
| EXAFS | Extended X-ray Absorption Fine Structure |
| FIB | Focused ion beam |
| FLIM | Fluorescence lifetime imaging |
| FPA | Focal plane array detector |
| FT-IR | Fourier-transform infrared (microscopy) |
| FWHM | Full-width at half maximum |
| FZP | Fresnel zone plate |
| GC | Gas chromatography |
| IR | Infrared |
| KB | Kirkpatrick-Baez (focusing mirrors) |
| LA-ICP-MS | Laser ablation-Inductively coupled plasma-Mass spectrometry |
| HPLC | High performance liquid chromatography |
| Ma | Million years |
| MS | Mass spectrometry |
| NEXAFS | Near-edge X-ray Absorption Fine Structure (= XANES) |
| OM | Organic matter |
| PIXE | Particle induced X-ray emission |
| refl. | reflection |
| ROI | Region of interest |
| SAXS | Small-angle X-ray scattering |
| SEM | Scanning electron microscopy |
| SIMS | Secondary ion mass spectroscopy |
| SR | Synchrotron radiation |
| STXM | Scanning transmission X-ray microscopy |
| TLC | Thin-layer chromatography |
| TOF | Time of flight |
| transm. | transmission |
| TXM | (Full-field) transmission X-ray microscopy |
| typ. | typical(ly) |
| UV | Ultraviolet |
| SR-UV-LFS | Synchrotron UV/VIS luminescence full-field spectro-microscopy |
| SR-UV-LMS | Synchrotron UV/VIS luminescence microspectroscopy |
| VIS | Visible |
| VUV | Vacuum ultraviolet |
| XANES | X-ray Absorption Near Edge Structure |
| XAS | X-ray absorption |
| X-PEEM | X-ray photoemission electron microscopy |
| XPS | X-ray photoelectron spectroscopy |
| XRD | X-ray diffraction |
| XRF | X-ray fluorescence |
| WDS/WDX | Wavelength dispersive X-ray spectroscopy |
| μ | Micro |

## References


[1] C. Renfrew, P. Bahn, Archaeology: Theories, Methods and Practice, 3rd Edition, Thames & Hudson, London, UK, 2000.
[2] M.A. Pollard, C. Heron, Archaeological Chemistry, Royal Society of Chemistry 2008. URL: http://dx.doi.org/10.1039/9781847558299.
[3] K. Janssens, K. Proost, G. Falkenberg, Confocal microscopic X-ray fluorescence at the HASYLAB microfocus beamline: characteristics and possibilities, Spectrochim. Acta B 59 (10–11) (2004) 1637–1645. URL: http://dx.doi.org/10.1016/j.sab.2004.07.025.
[4] L. Robinet, M. Spring, S. Pagès-Camagna, D. Vantelon, N. Trcera, Investigation of the discoloration of smalt pigment in historic paintings by Co K-edge micro X-ray absorption spectroscopy, Anal. Chem. 83 (13) (2011) 5145–5152. http://pubs.acs.org/doi/pdf/10.1021/ac200184f URL: http://dx.doi.org/10.1021/ac200184f.
[5] J.C. Hiller, T.J. Wess, Investigation of diagenetic and postmortem bone mineral change by small-angle X-ray scattering, in: D. Bradley, D. Creagh (Eds.), Physical Techniques in the Study of Art, Archaeology and Cultural Heritage, vol. 1, Elsevier, 2006, Ch. 3, pp. 125–149.
[6] J.C. Hiller, T.J. Wess, The use of small-angle X-ray scattering to study archaeological and experimentally altered bone, J. Archaeol. Sci. 33 (4) (2006) 560–572. URL: http://dx.doi.org/10.1016/j.jas.2005.09.012.
[7] P. Tafforeau, T.M. Smith, Nondestructive imaging of hominoid dental microstructure using phase contrast X-ray synchrotron microtomography, J. Human Evol. 54 (2) (2008) 272–278. http://dx.doi.org/10.1016/j.jhevol.2007.09.018.
[8] G. Harbottle, B.M. Gordon, K.W. Jones, Use of synchrotron radiation in archaeometry, Nucl. Instrum. Methods B 14 (1) (1986) 116–122. URL: http://dx.doi.org/10.1016/0168-583X(86)90431-3.

[9] I. Brissaud, J.X. Wang, P. Chevallier, Synchrotron radiation induced X-ray fluorescence at LURE, J. Radioanal. Nucl. Chem. 131 (2) (1989) 399–413. URL: http://dx.doi.org/10.1007/BF02060606.

[10] I. Brissaud, P. Chevallier, C. Dardenne, N. Deschamps, J.P. Frontier, K. Gruel, A. Taccoen, A. Tarrats, J.X. Wang, Analysis of Gaulish coins by proton induced X-ray emission, synchrotron radiation X-ray fluorescence and neutron activation analysis, Nucl. Instrum. Methods B 49 (1–4) (1990) 305–308. URL: http://dx.doi.org/10.1016/0168-583X(90)90265-V.

[11] I. Nakai, A. Iida, Applications of SR-XRF imaging and micro-XANES to meteorites, archaeological objects and animal tissues, in: C.S. Barrett, J.V. Gilfrich, T.C. Huang, R. Jenkins, G.J. McCarthy, P.K. Predecki, R. Ryon, D. Smith (Eds.), Advances in X-ray analysis, vol. 35, Plenum Press, New-York, USA, 1992, pp. 1307–1315.

[12] A.M. Pollard, P. Bray, A bicycle made for two? The integration of scientific techniques into archaeological interpretation, Annu. Rev. Anthropol. 36 (2007) 245–259. URL: http://dx.doi.org/10.1146/annurev.anthro.36.081406.094354.

[13] L. Bertrand, L. Robinet, M. Thoury, K. Janssens, S.X. Cohen, S. Schöder, Cultural heritage and archaeology materials studied by synchrotron spectroscopy and imaging, Appl. Phys. A 106 (2) (2011) 377–396. URL: http://dx.doi.org/10.1007/s00339-011-6686-4.

[14] L. Bertrand, Synchrotron imaging for archaeology, art history, conservation and paleontology, in: D.C. Creagh, D.A. Bradley (Eds.), in: Physical Techniques in the Study of Art, Archaeology and Cultural Heritage, vol. 2, Elsevier Science, 2007, pp. 97–114.

[15] P. Tafforeau, R. Boistel, E. Boller, A. Bravin, M. Brunet, Y. Chaimanee, P. Cloetens, M. Feist, J. Hoszowska, J.J. Jaeger, R.F. Kay, V. Lazzari, L. Marivaux, A. Nel, C. Nemoz, X. Thibault, P. Vignaud, S. Zabler, Applications of X-ray synchrotron microtomography for non-destructive 3D studies of paleontological specimens, Appl. Phys. A 83 (2) (2006) 195–202. URL: http://dx.doi.org/10.1007/s00339-006-3507-2.

[16] M.D. Sutton, Tomographic techniques for the study of exceptionally preserved fossils, Proc. Roy. Soc. B 275 (1643) (2008) 1587–1593.

[17] M. Cotte, P. Dumas, Y. Taniguchi, E. Checroun, P. Walter, J. Susini, Recent applications and current trends in Cultural Heritage Science using synchrotron-based Fourier transform infrared micro-spectroscopy, C. R. Physique 10 (7) (2009) 590–600. URL: http://dx.doi.org/10.1016/j.crhy.2009.03.016.

[18] M. Cotte, J. Susini, J. Dik, K. Janssens, Synchrotron-based X-ray absorption spectroscopy for art conservation: looking back and looking forward, Acc. Chem. Res. 43 (6) (2010) 705–714. URL: http://dx.doi.org/10.1021/ar900199m.

[19] M.C. Martin, U. Schade, P. Lerch, P. Dumas, Recent applications and current trends in analytical chemistry using synchrotron-based Fourier-transform infrared microspectroscopy, Trends Anal. Chem. 29 (6) (2010) 453–463. http://dx.doi.org/10.1016/j.trac.2010.03.002. URL: http://www.sciencedirect.com/science/article/B6V5H-4YMY6VN-1/2/94dfde5a2cd6ee6466d173a0adcc9f5f.

[20] A. Hofmann, The Physics of Synchrotron Radiation, Cambridge University Press, 2004.

[21] J. Als-Nielsen, D. McMorrow, Elements of Modern X-ray Physics, John Wiley & Sons, Ltd, 2001.

[22] S. Réguer, P. Dillmann, F. Mirambet, Buried iron archaeological artefacts: Corrosion mechanisms related to the presence of Cl-containing phases, Corros. Sci. 49 (6) (2007) 2726–2744. URL: http://dx.doi.org/10.1016/j.corsci.2006.11.009.

[23] S. Bernard, K. Benzerara, O. Beyssac, G.E. Brown, L.G. Stamm, P. Duringer, Ultrastructural and chemical study of modern and fossil sporoderms by Scanning Transmission X-ray Microscopy (STXM), Rev. Palaeobot. Palynol. 156 (1–2) (2009) 248–261. URL: http://dx.doi.org/10.1016/j.revpalbo.2008.09.002.

[24] L. Bertrand, M.-A. Languille, S.X. Cohen, L. Robinet, C. Gervais, S. Leroy, D. Bernard, E. Le Pennec, W. Josse, J. Doucet, S. Schöder, European research platform IPANEMA at the SOLEIL synchrotron for ancient and historical materials, J. Synchrotron Radiat. 18 (5) (2011) 765–772. URL: http://dx.doi.org/10.1107/S090904951102334X.

[25] R. Salzer, H.W. Siesler, Infrared and Raman Spectroscopic Imaging, Wiley-VCH, Weinheim, Germany, 2009.

[26] P.J. Eng, M. Newville, M.L. Rivers, S.R. Sutton, Dynamically figured Kirkpatrick Baez X-ray micro-focusing optics, in: Proc. SPIE Conf. on X-ray Micro-focusing: Applications and Techniques, San Diego, California, July 1998, vol. 3449, 1998, pp. 145–156. URL: http://dx.doi.org/10.1117/12.330342.

[27] W. Yun, B. Lai, Z. Cai, J. Maser, D. Legnini, E. Gluskin, Z. Chen, A.A. Krasnoperova, Y. Vladimirsky, F. Cerrina, E. Di. Fabrizio, M. Gentili, Nanometer focusing of hard X-rays by phase zone plates, Rev. Sci. Instrum. 70 (5) (1999) 2238–2241. URL: http://dx.doi.org/10.1063/1.1149744.

[28] A. Snigirev, V. Kohn, I. Snigireva, B. Lengeler, A compound refractive lens for focusing high-energy X-rays, Nature 384 (1996) 49–51.

[29] B. Lengeler, J. Tümmler, A. Snigirev, I. Snigireva, C. Raven, Transmission and gain of singly and doubly focusing refractive X-ray lenses, J. Appl. Phys. 84 (11) (1998) 5855–5861. URL: http://dx.doi.org/10.1063/1.368899.

[30] D.H. Bilderback, S.A. Hoffman, D.J. Thiel, Nanometer spatial resolution achieved in hard X-ray imaging and Laue diffraction experiments, Science 263 (5144) (1994) 201–203. URL: http://dx.doi.org/10.1126/science.8284671.

[31] G.H. Zschornack, Handbook of X-ray Data, Springer Verlag, Berlin, Heidelberg, 2007.

[32] A.C. Thompson, D. Vaughan, X-ray data booklet, Center for X-ray Optics and Advanced Light Source, Lawrence Berkeley National Laboratory, USA, Oct. 2009.

[33] M.J. Berger, J.H. Hubbell, S.M. Seltzer, J. Chang, J.S. Coursey, R. Sukumar, D.S. Zucker, K. Olsen, Xcom: Photon cross sections database, Website, NIST Standard Reference Database 8 (XGAM) [cited Aug. 21, 2011]. URL: http://www.nist.gov/pml/data/xcom/.

[34] L. Jacobson, W.A. Van der westhuizen, J. Oosthuysen, SARM 69 CERAMIC-1: A new pottery certified reference material for inter- and intra-laboratory calibration, in: E. Jerem, K.T. Biro (Eds.), Proc. 31th Int. Symp. Archaeometry, Budapest, 26 April–3 May 1998, Archaeopress BAR Int. Ser. 1043 (II), Oxford, 2002, pp. 585–586.

[35] B. Beckhoff, B. Kanngiesser, N. Langhoff, R. Wedell, H. Wolff, Handbook of Practical X-ray Fluorescence Analysis, Springer Verlag, Berlin, Heidelberg, 2006.

[36] I. Mantouvalou, W. Malzer, I. Schaumann, L. Lühl, R. Dargel, C. Vogt, B. Kanngiesser, Reconstruction of thickness and composition of stratified materials by means of 3D micro X-ray fluorescence spectroscopy, Anal. Chem. 80 (3) (2008) 819–826. http://dx.doi.org/10.1021/ac701774d. URL: http://dx.doi.org/10.1021/ac701774d.

[37] S. Leroy, R. Simon, L. Bertrand, A. Williams, E. Foy, P. Dillmann, First examination of slag inclusions in medieval armours by confocal SR-micro-XRF and LA-ICP-MS, J. Anal. Atom. Spectrom. 26 (2011) 1078–1087. URL: http://dx.doi.org/10.1039/C0JA00261E.

[38] S. Lahlil, M. Cotte, I. Biron, J. Szlachetko, N. Menguy, J. Susini, Synthesizing lead antimonate in ancient and modern opaque glass, J. Anal. Atom. Spectrom. 26 (2011) 1040–1050. URL: http://dx.doi.org/10.1039/C0JA00251H.

[39] J. Szlachetko, M. Cotte, J. Morse, M. Salome, P. Jagodzinski, J.C. Dousse, J. Hoszowska, Y. Kayser, J. Susini, Wavelength-dispersive spectrometer for X-ray microfluorescence analysis at the X-ray microscopy beamline ID21 (ESRF), J. Synchrotron Radiat. 17 (2010) 400–408. http://dx.doi.org/10.1107/S0909049510010691. URL: http://dx.doi.org/10.1107/S0909049510010691.

[40] M. Cotte, J. Szlachetko, S. Lahlil, M. Salomé, V.A. Solé, I. Biron, J. Susini, Coupling a Wavelength Dispersive Spectrometer with a synchrotron-based X-ray microscope: a winning combination for micro-X-ray fluorescence and micro-XANES analyses of complex artistic materials, J. Anal. Atom. Spectrom. 26 (5) (2011) 1051–1059.

[41] C. Ryan, R. Kirkham, R. Hough, G. Moorhead, D. Siddons, M. de Jonge, D. Paterson, G.D. Geronimo, D. Howard, J. Cleverley, Elemental X-ray imaging using the Maia detector array: the benefits and challenges of large solid-angle, Nucl. Instrum. Methods A 619 (1–3) (2010) 37–43. http://dx.doi.org/10.1016/j.nima.2009.11.035. URL: http://www.sciencedirect.com/science/article/B6TJM-4XP37N0-C/2/219fefd451b9d07d66e6034b579652ac.

[42] J. Dik, K. Janssens, G. van der Snickt, L. van der Loeff, K. Rickers, M. Cotte, Visualization of a Lost Painting by Vincent van Gogh Using Synchrotron Radiation Based X-ray Fluorescence Elemental Mapping, Anal. Chem. 80 (2008) 6436–6442. URL: http://dx.doi.org/10.1021/ac800965g.

[43] W. de Nolf, J. Dik, G. van der Snickt, A. Wallert, K. Janssens, High Energy X-ray Powder Diffraction for the imaging of (hidden) paintings, J. Anal. Atom. Spectrom. 26 (2011) 910–916. URL: http://dx.doi.org/10.1039/c0ja00255k.

[44] U. Bergmann, R.W. Morton, P.L. Manning, W.I. Sellers, S. Farrar, K.G. Huntley, R.A. Wogelius, P. Larson, Archaeopteryx feathers and bone chemistry fully revealed via synchrotron imaging, Proc. Natl. Acad. Sci. USA 107 (20) (2010) 9060–9065. http://dx.doi.org/10.1073/pnas.1001569107. URL: http://dx.doi.org/10.1073/pnas.1001569107.

[45] M. Alfeld, K. Janssens, K. Appel, B. Thijsse, J. Blaas, J. Dik, A portrait by Philip Otto Runge – Visualizing modifications to the painting using synchrotron-based X-ray Fluorescence Elemental Scanning, Z. Kunsttech. Konser. 25 (2011) 157–163.

[46] O. Scharf, S. Ihle, I. Ordavo, V. Arkadiev, A. Bjeoumikhov, S. Bjeoumikhova, G. Buzanich, R. Gubzhokov, A. Günther, R. Hartmann, M. Kühbacher, M. Lang, N. Langhoff, A. Liebel, M. Radtke, U. Reinholz, H. Riesemeier, H. Soltau, L. Strüder, A.F. Thünemann, R. Wedell, Compact pnCCD-based X-ray camera with high spatial and energy resolution: A Color X-ray Camera, Anal. Chem. http://pubs.acs.org/doi/pdf/10.1021/ac102811p, http://dx.doi.org/10.1021/ac102811p. URL: http://pubs.acs.org/doi/abs/10.1021/ac102811p.

[47] B.K. Teo, EXAFS: Basic Principles and Data Analysis, 1st edition, in: Inorganic Chemistry Concepts, vol. 9, Springer-Verlag, Berlin, 1986, 349 p.

[48] D.C. Koningsberger, R. Prins, X-ray Absorption. Principles, Applications, Techniques of EXAFS, SEXAFS and XANES, 1st edition, in: Chemical Analysis, John Wiley, 1987, p. 688 p.

[49] F.W. Lytle, D.E. Sayers, E.A. Stern, Extended X-ray-absorption fine-structure technique. II. Experimental practice and selected results, Phys. Rev. B 11 (12) (1975) 4825–4835. URL: http://dx.doi.org/10.1103/PhysRevB.11.4825.

[50] M.G. Dowsett, A. Adriaens, G.K.C. Jones, N. Poolton, S. Fiddy, S. Nikitenko, Optically Detected X-ray absorption spectroscopy measurements as a means of monitoring corrosion layers on copper, Anal. Chem. 80 (22) (2008) 8717–8724. http://dx.doi.org/10.1021/ac800895n. URL: http://dx.doi.org/10.1021/ac800895n.

[51] L. Samain, G. Silversmit, J. Sanyova, B. Vekemans, H. Salomon, B. Gilbert, F. Grandjean, G.J. Long, R.P. Hermann, L. Vincze, D. Strivay, Fading of modern Prussian blue pigments in linseed oil medium, J. Anal. Atom. Spectrom. 26 (2011) 930–941. URL: http://dx.doi.org/10.1039/C0JA00234H.

[52] C. Gervais, M.-A. Languille, M. Gillet, C. Garnier, S. Pelletier, S. Reguer, E. Vicenzi, L. Bertrand, Light-induced fading of Prussian blue: It does not come out of the blue, rather from the substrate (in preparation).

[53] L. Monico, G. van der Snickt, K. Janssens, W. de Nolf, C. Miliani, J. Dik, M. Radepont, E. Hendriks, M. Geldof, M. Cotte, Degradation process of lead chromate in paintings by Vincent van Gogh studied by means of synchrotron X-ray spectromicroscopy and related methods. 2. original paint layer samples, Anal. Chem. 83 (4) (2011) 1224–1231.

[54] L. Monico, G. van der Snickt, K. Janssens, W. de Nolf, C. Miliani, M. Radepont, J. Dik, E. Hendriks, M. Geldof, M. Cotte, Degradation process of lead chromate in paintings by Vincent van Gogh studied by means of Synchrotron X-ray Spectromicroscopy and related methods. 1. Artificially aged model samples, Anal. Chem. 83 (2011) 1214–1223. URL: http://dx.doi.org/10.1021/ac102424h.

[55] L. Zanella, F. Casadio, K.A. Gray, R. Warta, Q. Ma, J.-F. Gaillard, The darkening of zinc yellow: XANES speciation of chromium in artist's paints after light and chemical exposures, J. Anal. Atom. Spectrom. 26 (2011) 1090–1097. URL: http://dx.doi.org/10.1039/C0JA00151A.

[56] M. Cotte, J. Susini, V.A. Solé, Y. Taniguchi, J. Chillida, É Checroun, P. Walter, Applications of synchrotron-based micro-imaging techniques to the chemical analysis of ancient paintings, J. Anal. Atom. Spectrom. 23 (2008) 820–828. URL: http://dx.doi.org/10.1039/b801358f.

[57] M. Cotte, J. Susini, Watching ancient paintings through synchrotron-based X-ray microscopes, MRS Bull. 34 (6) (2009) 403–405.

[58] M. Cotte, J. Susini, N. Metrich, A. Moscato, C. Gratziu, A. Bertagnini, M. Pagano, Blackening of Pompeian cinnabar paintings: X-ray microspectroscopy analysis, Anal. Chem. 78 (21) (2006) 7484–7492. URL: http://dx.doi.org/10.1021/ac0612224.

[59] M. Radepont, W. de Nolf, K. Janssens, G. van der Snickt, Y. Coquinot, L. Klaassen, M. Cotte, The use of microscopic X-ray diffraction for the study of HgS and its degradation products corderoite ($\alpha$-$Hg_3S_2Cl_2$), kenhsuite ($\gamma$-$Hg_3S_2Cl_2$) and calomel ($Hg_2Cl_2$) in historical paintings, J. Anal. Atom. Spectrom. 26 (2011) 959–968. URL: http://dx.doi.org/10.1039/c0ja00260g.

[60] M. Saheb, D. Neff, C. Bataillon, E. Foy, P. Dillmann, Copper tracing to determine the micrometric electronic properties of a thick ferrous corrosion layer formed in an anoxic medium, Corros. Sci. 53 (2011) 2201–2207.

[61] V. De Andrade, J. Susini, M. Salomé, O. Beraldin, C. Rigault, T. Heymes, E. Lewin, O. Vidal, Submicrometer hyperspectral X-ray imaging of heterogeneous rocks and geomaterials: applications at the Fe K-edge, Anal. Chem. 83 (11) (2011) 4220–4227. URL: http://dx.doi.org/10.1021/ac200559r.

[62] C. Jacobsen, J. Kirz, X-ray microscopy with synchrotron radiation, Nature Struct. Biol. 5 (1998) 650–653. URL: http://dx.doi.org/10.1038/1341.

[63] J. Kirz, C. Jacobsen, M. Howells, Soft X-ray microscopes and their biological applications, Q. Rev. Biophys. 28 (1) (1995) 33–130. URL: http://xray1.physics.sunysb.edu/downloads/qrb96.pdf.

[64] D. Solomon, J. Lehmann, J. Kinyangi, B. Liang, K. Heymann, L. Dathe, K. Hanley, S. Wirick, C. Jacobsen, Carbon (1s) NEXAFS spectroscopy of biogeochemically relevant reference, Soil Sci. Soc. Am. J. 73 (6) (2009) 1817–1830.

[65] C.K. Boyce, G.D. Cody, M. Feser, C. Jacobsen, A.H. Knoll, S. Wirick, Organic chemical differentiation within fossil plant cell walls detected with X-ray spectromicroscopy, Geology 30 (11) (2002) 1039–1042.

[66] S. Bernard, K. Benzerara, O. Beyssac, N. Menguy, F. Guyot, G.E. Brown Jr., B. Goffe, Exceptional preservation of fossil plant spores in high-pressure metamorphic rocks, Earth Planet. Sci. Lett. 262 (1–2) (2007) 257–272. URL: http://dx.doi.org/10.1016/j.epsl.2007.07.041.

[67] K. Benzerara, S. Bernard, K. Lepot, J. Miot, G.E. Brown, STXM-based study of microbial fossils in recent and ancient rocks, Geochim. Cosmochim. Acta 72 (12) (2008) A75. URL: http://dx.doi.org/10.1016/j.gca.2008.05.005.

[68] B. Warren, X-ray Diffraction, Dover Publications, Inc., New York, 1990.

[69] A. Guinier, X-ray Diffraction in Crystals, Imperfect Crystals and Amorphous Bodies, 1st edition, Dover, New York, 1994.

[70] C. Giacovazzo, H.L. Monaco, G. Artioli, D. Viterbo, G. Ferraris, G. Gilli, G. Zanotti, M. Catti, Fundamentals of crystallography, in: IUCr Texts on Crystallography, vol. 7, Oxford University Press, 2002, URL http://books.google.com/books?id=ISTwAAAAMAAJ.

[71] J. Rodenburg, A. Hurst, A. Cullis, B. Dobson, F. Pfeiffer, O. Bunk, C. David, K. Jefimovs, I. Johnson, Hard-X-ray lensless imaging of extended objects, Phys. Rev. Lett. 98 (3) (2007) 34801.

[72] J. Miao, K. Hodgson, T. Ishikawa, C. Larabell, M. LeGros, Y. Nishino, Imaging whole *Escherichia coli* bacteria by using single-particle X-ray diffraction, Proc. Natl. Acad. Sci. USA 100 (1) (2003) 110.

[73] C.G. Schroer, P. Boye, J. Feldkamp, J. Patommel, A. Schropp, A. Schwab, S. Stephan, M. Burghammer, S. Schöder, C. Riekel, Coherent X-ray diffraction imaging with nanofocused illumination, Phys. Rev. Lett. 101 (9) (2010) 090801.

[74] A. Schropp, P. Boye, A. Goldschmidt, S. Hönig, R. Hoppe, J. Patommel, C. Rakete, D. Samberg, S. Stephan, S. Schöder, M. Burghammer, C.G. Schroer, Non-destructive and quantitative imaging of a nano-structured microchip by ptychographic hard X-ray scanning microscopy, J. Microsc. 241 (1) (2010) 9–12.

[75] I. Robinson, I. Vartanyants, G. Williams, M.A. Pfeifer, J.A. Pitney, Reconstruction of the shapes of gold nanocrystals using coherent X-ray diffraction, Phys. Rev. Lett. 87 (2001) 195505.

[76] I. Robinson, R. Harder, Coherent X-ray diffraction imaging of strain at the nanoscale, Nat. Mater. 8 (2009) 291–298.

[77] Y. Leon, P. Sciau, P. Goudeau, N. Tamura, S. Webb, A. Mehta, The nature of marbled Terra Sigillata slips: a combined XRF and XRD investigation, Appl. Phys. A 99 (2) (2010) 419–425.

[78] C. Riekel, New avenues in X-ray microbeam experiments, Rep. Prog. Phys. 63 (3) (2000) 233–262.

[79] O. Paris, From diffraction to imaging: New avenues in studying hierarchical biological tissues with X-ray microbeams (Review), Biointerphases 3 (2) (2008) 16–26.

[80] M. Hanke, M. Dubslaff, M. Schmidbauer, T. Boeck, S. Schöder, M. Burghammer, C. Riekel, J. Patommel, C.G. Schroer, Scanning X-ray diffraction with 200 nm spatial resolution, Appl. Phys. Lett. 92 (19) (2008) 193109–193109-3.

[81] E. Leccia, A. Gourrier, J. Doucet, F. Briki, Hard alpha-keratin degradation inside a tissue under high flux X-ray synchrotron micro-beam: a multi-scale time-resolved study, J. Struct. Biol. 170 (1) (2010) 69–75.

[82] C. Riekel, M. Burghammer, R. Davies, E. Di Cola, C. Konig, H. Lemke, J. Putaux, S. Schöder, Raster microdiffraction with synchrotron radiation of hydrated biopolymers with nanometre step-resolution: case study of starch granules, J. Synchrotron Radiat. 17 (6).

[83] M. Howells, T. Beetz, H. Chapman, C. Cui, J. Holton, C. Jacobsen, J. Kirz, E. Lima, S. Marchesini, H. Miao, An assessment of the resolution limitation due to radiation-damage in X-ray diffraction microscopy, J. Electron. Spectrosc. Relat. Phenom. 170 (1–3) (2009) 4–12.
[84] L. Herrera, A. Justo, A. Duran, M. de Haro, M. Franquelo, J. Perez Rodríguez, Identification of cellulose fibres belonging to Spanish cultural heritage using synchrotron high resolution X-ray diffraction, Appl. Phys. A 99 (2) (2010) 391–398.
[85] A. Hermes, R. Davies, S. Greiff, H. Kutzke, S. Lahlil, P. Wyeth, C. Riekel, Characterizing the decay of ancient chinese silk fabrics by microbeam synchrotron radiation diffraction, Biomacromolecules 7 (3) (2006) 777–783.
[86] M. Müller, B. Murphy, M. Burghammer, C. Riekel, M. Roberts, M. Papiz, D. Clarke, J. Gunneweg, E. Pantos, Identification of ancient textile fibres from Khirbet Qumran caves using synchrotron radiation microbeam diffraction, Spectrochim. Acta, B 59 (10–11) (2004) 1669–1674.
[87] M. Cotte, J. Susini, V.A. Solé, Y. Taniguchi, J. Chillida, E. Checroun, P. Walter, Applications of synchrotron-based micro-imaging techniques to the chemical analysis of ancient paintings, J. Anal. Atom. Spectrom. 23 (6) (2008) 820.
[88] N. Salvadó, S. Butí, J. Nicholson, H. Emerich, A. Labrador, T. Pradell, Identification of reaction compounds in micrometric layers from gothic paintings using combined SR-XRD and SR-FTIR, Talanta 79 (2) (2009) 419–428.
[89] N. Salvadó, T. Pradell, E. Pantos, M. Papiz, J. Molera, M. Seco, M. Vendrell-Saz, Identification of copper-based green pigments in Jaume Huguet's Gothic altarpieces by Fourier transform infrared microspectroscopy and synchrotron radiation X-ray diffraction, J. Synchrotron Radiat. 9 (4) (2002) 215–222.
[90] C.J. Kennedy, J.C. Hiller, D. Lammie, M. Drakopoulos, M. Vest, M. Cooper, W.P. Adderley, T.J. Wess, Microfocus X-ray diffraction of historical parchment reveals variations in structural features through parchment cross sections, Nano Lett. 4 (8) (2004) 1373–1380. URL: http://dx.doi.org/10.1021/nl049696a.
[91] T. Narayanan, Synchrotron Small-Angle X-ray Scattering, in: R. Borsali, R. Pecora (Eds.), Soft Matter: Scattering, Imaging and Manipulation, Springer-Verlag New York Inc., 2008, pp. 899–952.
[92] M.M. Basil-Jones, R.L. Edmonds, T.F. Allsop, S.M. Cooper, G. Holmes, G.E. Norris, D.J. Cookson, N. Kirby, R.G. Haverkamp, Leather structure determination by small-angle X-ray scattering (SAXS): cross sections of ovine and bovine leather, J. Agric. Food Chem. 58 (9) (2010) 5286–5291.
[93] L. Bertrand, J. Doucet, P. Dumas, A. Simionovici, G. Tsoucaris, P. Walter, Microbeam synchrotron imaging of hairs from Ancient Egyptian mummies, J. Synchrotron Radiat. 10 (5) (2003) 387–392. URL: http://dx.doi.org/10.1107/S0909049503015334.
[94] T. Wess, M. Drakopoulos, A. Snigirev, J. Wouters, O. Paris, P. Fratzl, M. Collins, J. Hiller, K. Nielsen, The use of small-angle X-ray diffraction studies for the analysis of structural features in archaeological samples, Archaeometry 43 (1) (2001) 117–129.
[95] J. Hiller, M. Collins, A. Chamberlain, T. Wess, Small-angle X-ray scattering: a high-throughput technique for investigating archaeological bone preservation, J. Archaeol. Sci. 31 (10) (2004) 1349–1359.
[96] T. Wess, I. Alberts, J. Hiller, M. Drakopoulos, A. Chamberlain, M. Collins, Microfocus small angle X-ray scattering reveals structural features in archaeological bone samples; detection of changes in bone mineral habit and size, Calcified Tissue Int. 70 (2) (2002) 103–110.
[97] J. Baruchel, J.Y. Buffière, E. Maire, P. Merle, G. Peix, X-ray Tomography in Material Science, Hermes Sci. Publ., Paris, 2000.
[98] J. Als-Nielsen, D. McMorrow, Elements of Modern X-ray Physics, 2nd edition, Wiley, 2011.
[99] M. Born, E. Wolf, Principles of Optics: Electromagnetic Theory of Propagation, Interference and Diffraction of Light, 7th edition, Cambridge University Press, 1999.
[100] R.D.L. Kronig, On the theory of dispersion of X-rays, J. Opt. Soc. Am. Rev. Sci. Instrum. 12 (6) (1926) 547–557.
[101] A.C. Kak, M. Slaney, Principles of Computerized Tomographic Imaging, Classics in Applied Mathematics, vol. 33, Society for Industrial and Applied Mathematics, 2001.
[102] U. Bonse, F. Busch, X-ray computed microtomography (μCT) using synchrotron radiation (SR), Prog. Biophys. Mol. Biol. 65 (1–2) (1996) 133–169. URL: http://dx.doi.org/10.1016/S0079-6107(96)00011-9.
[103] A. Snigirev, I. Snigireva, V. Kohn, S. Kuznetsov, I. Schelokov, On the possibilities of X-ray phase contrast microimaging by coherent high-energy synchrotron radiation, Rev. Sci. Instrum. 66 (12) (1995) 5486–5492.
[104] P. Cloetens, R. Barrett, J. Baruchel, J.P. Guigay, M. Schlenker, Phase objects in synchrotron radiation hard X-ray imaging, J. Phys. D 29 (1) (1996) 133–146.
[105] U. Bonse, M. Hart, An X-ray interferometer with long separated interfering beam paths, Appl. Phys. Lett. 7 (4) (1965) 99–100. URL: http://dx.doi.org/10.1063/1.1754330.
[106] A. Momose, Demonstration of phase-contrast X-ray computed-tomography using an X-ray interferometer, Nucl. Instrum. Methods A 352 (3) (1995) 622–628.
[107] T. Weitkamp, A. Diaz, C. David, F. Pfeiffer, M. Stampanoni, P. Cloetens, E. Ziegler, X-ray phase imaging with a grating interferometer, Opt. Express 13 (16) (2005) 6296–6304.
[108] T.J. Davis, D. Gao, T.E. Gureyev, A.W. Stevenson, S.W. Wilkins, Phase-contrast imaging of weakly absorbing materials using hard X-rays, Nature 373 (6515) (1995) 595–598. URL: http://dx.doi.org/10.1038/373595a0.
[109] D. Chapman, W. Thomlinson, R.E. Johnston, D. Washburn, E. Pisano, N. Gmur, Z. Zhong, R. Menk, F. Arfelli, D. Sayers, Diffraction enhanced X-ray imaging, Phys. Med. Biol. 42 (11) (1997) 2015–2025. URL: http://stacks.iop.org/0031-9155/42/2015.
[110] U. Bonse, M. Hart, An X-ray interferometer, Appl. Phys. Lett. 6 (8) (1965) 155–156. URL: 10.1063/1.1754212.
[111] T.J. Davis, A.W. Stevenson, Direct measure of the phase shift of an X-ray beam, J. Opt. Soc. Am. A 13 (6) (1996) 1193–1198. http://dx.doi.org/10.1364/JOSAA.13.001193. URL: http://josaa.osa.org/abstract.cfm?URI=josaa-13-6-1193.
[112] A.V. Bronnikov, Theory of quantitative phase-contrast computed tomography, J. Opt. Soc. Am. A 19 (3) (2002) 472–480.
[113] A. Groso, R. Abela, M. Stampanoni, Implementation of a fast method for high resolution phase contrast tomography, Opt. Express 14 (18) (2006) 8103–8110.
[114] D. Paganin, S. Mayo, T. Gureyev, P. Miller, S. Wilkins, Simultaneous phase and amplitude extraction from a single defocused image of a homogeneous object, J. Microsc. Oxford 206 (1) (2002) 33–40.
[115] P. Cloetens, W. Ludwig, J. Baruchel, D. van Dyck, J. van Landuyt, J.-P. Guigay, M. Schlenker, Holotomography: Quantitative phase tomography with micrometer resolution using hard synchrotron radiation X-rays, Appl. Phys. Lett. 75 (19) (1999) 2912. URL: http://dx.doi.org/10.1063/1.125225.
[116] C. Soriano, M. Archer, D. Azar, P. Creaser, X. Delclòs, H. Godthelp, S. Hand, A. Jones, A. Nel, D. Néraudeau, J. Ortega-Blanco, R. Pérez-de la fuente, V. Perrichot, E. Saupe, M. Solórzano Kraemer, P. Tafforeau, Synchrotron X-ray imaging of inclusions in amber, C. R. Palevol 9 (6–7) (2010) 361–368. http://dx.doi.org/10.1016/j.crpv.2010.07.014.
[117] S.Y. Smith, M.E. Collinson, P.J. Rudall, D.A. Simpson, F. Marone, M. Stampanoni, Virtual taphonomy using synchrotron tomographic microscopy reveals cryptic features and internal structure of modern and fossil plants, Proc. Natl. Acad. Sci. USA 106 (29) (2009) 12013–12018.
[118] E.M. Friis, K.R. Pedersen, *Canrightia resinifera* gen. et sp. nov., a new extinct angiosperm with *Retimonocolpites*-type pollen from the Early Cretaceous of Portugal: missing link in the eumagnoliid tree?, Grana 50 (1) (2011) 3–29. URL: http://dx.doi.org/10.1080/00173134.2011.559728.
[119] M. Stampanoni, A. Groso, A. Isenegger, G. Mikuljan, Q. Chen, A. Bertrand, S. Henein, R. Betemps, U. Frommherz, P. Böhler, D. Meister, M. Lange, R. Abela, Trends in synchrotron-based tomographic imaging: the SLS experience, in: U. Bonse (Ed.), Developments in X-ray Tomography V, Proc. of SPIE, Vol. 6318, SPIE, 2006, p. 63180M. URL: http://dx.doi.org/10.1117/12.679497.
[120] J. Pouech, J.M. Mazin, P. Tafforeau, High quality 3D imaging of vertebrate microremains using X-ray synchrotron phase contrast microtomography, C.-R. Palevol. 9 (6–7) (2010) 389–395. http://dx.doi.org/10.1016/j.crpv.2010.07.010.
[121] J.-P. Guigay, M. Langer, R. Boistel, P. Cloetens, Mixed transfer function and transport of intensity approach for phase retrieval in the Fresnel region, Opt. Lett. 32 (12) (2007) 1617–1619. URL: http://dx.doi.org/10.1364/OL.32.001617.
[122] A. Pradel, M. Langer, J.G. Maisey, D. Geffard-Kuriyama, P. Cloetens, P. Janvier, P. Tafforeau, Skull and brain of a 300-million-year-old chimaeroid fish revealed by synchrotron holotomography, Proc. Natl. Acad. Sci. USA 106 (13) (2009) 5224–5228. http://dx.doi.org/10.1073/pnas.0807047106. URL: http://dx.doi.org/10.1073/pnas.0807047106.

[123] E.H. Anderson, D.L. Olynick, B. Harteneck, E. Veklerov, G. Denbeaux, W.L. Chao, A. Lucero, L. Johnson, D. Attwood, Nanofabrication and diffractive optics for high-resolution X-ray applications, J. Vac. Sci. Technol. B 18 (6) (2000) 2970–2975.
[124] K. Jefimovs, J. Vila-Comamala, M. Stampanoni, B. Kaulich, C. David, Beam-shaping condenser lenses for full-field transmission X-ray microscopy, J. Synchrotron Radiat. 15 (2008) 106–108. URL: http://dx.doi.org/10.1107/S0909049507047711.
[125] G.C. Yin, Y.F. Song, M.T. Tang, F.R. Chen, K.S. Liang, F.W. Duewer, M. Feser, W.B. Yun, H.P.D. Shieh, 30 nm resolution X-ray imaging at 8 keV using third order diffraction of a zone plate lens objective in a transmission microscope, Appl. Phys. Lett. 89 (22) (2006) 221122.
[126] C. Rau, V. Crecea, C.P. Richter, K.M. Peterson, P.R. Jemian, U. Neuhausler, G. Schneider, X. Yu, P.V. Braun, T.C. Chiang, I.K. Robinson, A hard X-ray KB-FZP microscope for tomography with sub-100-nm resolution, in: U. Bonse (Ed.), Developments in X-ray Tomography V, in: Proceedings of the Society of Photo-Optical Instrumentation Engineers (SPIE), vol. 6318, SPIE—Int. Soc. Optical Engineering, 2006, pp. G3181-2–G3181-6.
[127] D.Y. Parkinson, G. McDermott, L.D. Etkin, M.A. Le Gros, C.A. Larabell, Quantitative 3-D imaging of eukaryotic cells using soft X-ray tomography, J. Struct. Biol. 162 (3) (2008) 380–386.
[128] J.L. Carrascosa, F.J. Chichón, E. Pereiro, M.J. Rodríguez, J.J. Fernández, M. Esteban, S. Heim, P. Guttmann, G. Schneider, Cryo-X-ray tomography of vaccinia virus membranes and inner compartments, J. Struct. Biol. 168 (2) (2009) 234–239.
[129] W. Meyer-Ilse, D. Hamamoto, A. Nair, S.A. Lelievre, G. Denbeaux, L. Johnson, A.L. Pearson, D. Yager, M.A. LeGros, C.A. Larabell, High resolution protein localization using soft X-ray microscopy, J. Microsc. Oxford 201 (3) (2001) 395–403. URL: http://dx.doi.org/10.1046/j.1365-2818.2001.00845.x.
[130] M. Stampanoni, R. Mokso, F. Marone, J. Vila-Comamala, S. Gorelick, P. Trtik, K. Jefimovs, C. David, Phase-contrast tomography at the nanoscale using hard X-rays, Phys. Rev. B 81 (14) (2010) 140105R. URL: http://dx.doi.org/10.1103/PhysRevB.81.140105.
[131] U. Neuhausler, G. Schneider, W. Ludwig, M.A. Meyer, E. Zschech, D. Hambach, X-ray microscopy in Zernike phase contrast mode at 4 keV photon energy with 60 nm resolution, J. Phys. D 36 (10A) (2003) A79–A82.
[132] A. Sakdinawat, Y. Liu, Soft-X-ray microscopy using spiral zone plates, Opt. Lett. 32 (18) (2007) 2635–2637. URL: http://dx.doi.org/10.1364/OL.32.002635.
[133] R. Mokso, P. Cloetens, E. Maire, W. Ludwig, J.Y. Buffiere, Nanoscale zoom tomography with hard X-rays using Kirkpatrick–Baez optics, Appl. Phys. Lett. 90 (14) (2007) 144104.
[134] E.S.B. Ferreira, J.J. Boon, M. Stampanoni, F. Marone, Study of the mechanism of formation of calcium soaps in an early 20th-century easel painting with correlative 2d and 3d microscopy, in: Proc. 16th ICOM-CC triennial conference, Lisbon, Portugal, 2011, 19–23 September, 2011.
[135] R. Mokso, F. Marone, M. Stampanoni, in: R. Garrett, I. Gentle, K. Nugent, S. Wilkins (Eds.), Real Time Tomography at the Swiss Light Source, in: SRI 2009: The 10th International Conference on Synchrotron Radiation Instrumentation, in: AIP Conference Proceedings, vol. 1234, Amer. Inst. Physics, 2010, pp. 87–90.
[136] F. Marone, B. Munch, M. Stampanoni, Fast reconstruction algorithm dealing with tomography artifacts, in: S.R. Stock (Ed.), Developments in X-ray Tomography VII, in: Proceedings of SPIE—The International Society for Optical Engineering, vol. 7804, SPIE—Int Soc Optical Engineering, 2010.
[137] A. Kyrieleis, V. Titarenko, M. Ibison, T. Connolley, P.J. Withers, Region-of-interest tomography using filtered backprojection: assessing the practical limits, J. Microsc. 241 (1) (2011) 69–82.
[138] A. Peres, Tomographic reconstruction from limited angular data, J. Comput. Assist. Tomogr. 3 (6) (1979) 800–803.
[139] J.T. Dobbins, D.J. Godfrey, Digital X-ray tomosynthesis: current state of the art and clinical potential, Phys. Med. Biol. 48 (19) (2003) R65–R106.
[140] L. Helfen, T. Baumbach, P. Mikulik, D. Kiel, P. Pernot, P. Cloetens, J. Baruchel, High-resolution three-dimensional imaging of flat objects by synchrotron-radiation computed laminography, Appl. Phys. Lett. 86 (7) (2005) 071915. URL: 10.1063/1.1854735.
[141] L. Helfen, T. Baumbach, P. Cloetens, J. Baruchel, Phase-contrast and holographic computed laminography, Appl. Phys. Lett. 94 (10) (2009) 104103.
[142] A. Houssaye, F. Xu, L. Helfen, V. De Buffrenil, T. Baumbach, P. Tafforeau, Three-dimensional pelvis and limb anatomy of the Cenomanian hind-limbed snake *Eupodophis descouensi* (Squamata, Ophidia) revealed by synchrotron-radiation computed laminography, J. Vertebrate Paleontol. 31 (1) (2011) 2–7.
[143] K. Krug, L. Porra, P. Coan, A. Wallert, J. Dik, A. Coerdt, A. Bravin, M. Elyyan, P. Reischig, L. Helfen, T. Baumbach, Relics in medieval altarpieces? Combining X-ray tomographic, laminographic and phase-contrast imaging to visualize thin organic objects in paintings, J. Synchrotron Radiat. 15 (1) (2008) 55–61. URL: http://dx.doi.org/10.1107/S0909049507045438.
[144] B. Valeur, Molecular Fluorescence Principles and Applications, Wiley VCH, Weinheim, Germany, 2002.
[145] B. Berrie, L. Mathews, Material Innovation and Artistic Invention: New Materials and New Colors in Renaissance Venetian Paintings, in: (Sackler NAS Colloquium) Scientific Examination of Art: Modern Techniques in Conservation and Analysis (2005), 2005, pp. 12–26.
[146] G. Bottiroli, A. Gallone Galassi, E. Bernacchi, Proc. of the Symposium on Scientific Methodologies Applied to Works of Art, Florence, Italy, 2–5 May 1984, Montedison Progetto Cultura, Florence, Italy, 1984, pp. 168–172.
[147] A. Claro, M.J. Melo, J.S. Seixas de Melo, K.J. van den Berg, A. Burnstock, Identification of Red Colorants in Van Gogh Paintings and Ancient Andean Textiles by Microspectrofluorimetry, J. Cult. Her. 11 (1) (2010) 27–34.
[148] M. Thoury, J.-P. Echard, M. Réfrégiers, B. Berrie, A. Nevin, F. Jamme, L. Bertrand, Synchrotron UV–visible multispectral luminescence micro-imaging of historical samples, Anal. Chem. 83 (5) (2011) 1737–1745. URL: http://dx.doi.org/10.1021/ac102986h.
[149] D. Comelli, C. D'andrea, G. Valentini, R. Cubeddu, C. Colombo, L. Toniolo, Fluorescence lifetime imaging and spectroscopy as tools for nondestructive analysis of works of art, Appl. Opt. 43 (2004) 2175–2183.
[150] J.R. Lakowicz, Principles of Fluorescence Spectroscopy, 3rd edition, Springer Science and Business Media, 2006.
[151] M. Perez-Alonso, K. Castro, J.M. Madariaga, Vibrational Spectroscopic Techniques for the Analysis of Artefacts with Historical, Artistic and Archaeological Value, Curr. Anal. Chem. 2 (1) (2006) 89–100. http://dx.doi.org/10.2174/157341106775197385. URL: http://dx.doi.org/10.2174/157341106775197385.
[152] S. Prati, E. Joseph, G. Sciutto, R. Mazzeo, New Advances in the Application of FTIR Microscopy and Spectroscopy for the Characterization of Artistic Materials, Acc. Chem. Res. 43 (6) (2010) 792–801. http://dx.doi.org/10.1021/ar900274f. http://pubs.acs.org/doi/pdf/10.1021/ar900274f, URL: http://pubs.acs.org/doi/abs/10.1021/ar900274f.
[153] M. Cotte, P. Dumas, G. Richard, R. Bréniaux, P. Walter, New insight on ancient cosmetic preparation by synchrotron-based infrared microscopy, Anal. Chim. Acta 553 (1–2) (2005) 105–110. URL: http://dx.doi.org/10.1016/j.aca.2005.07.067.
[154] N. Salvadó, S. Butí, M.J. Tobin, E. Pantos, J.N.W. Prag, T. Pradell, Advantages of the use of SR-FT-IR microspectroscopy: applications to cultural heritage, Anal. Chem. 77 (11) (2005) 3444–3451. URL: http://dx.doi.org/10.1021/ac050126k.
[155] M. Cotte, E. Checroun, J. Susini, P. Dumas, P. Tchoreloff, M. Besnard, P. Walter, Kinetics of oil saponification by lead salts in ancient preparations of pharmaceutical lead plasters and painting lead mediums, Talanta 70 (5) (2006) 1136–1142. URL: http://dx.doi.org/10.1016/j.talanta.2006.03.007.
[156] Study of the Afghanistan's Displaced Cultural Properties Materials and Techniques of the Bamiyan Mural Paintings, in: Recent Cultural Heritage Issues in Afghanistan, vol. 3, Japan Center for International Cooperation in Conservation, National Research Institute for Cultural Properties, Japan, 2006.
[157] J.-P. Echard, L. Bertrand, A. von Bohlen, A.-S. Le Hô, C. Paris, L. Bellot-Gurlet, B. Soulier, A. Lattuati-Derieux, S. Thao, L. Robinet, B. Lavédrine, S. Vaiedelich, The Nature of the Extraordinary Finish of Stradivari's Instruments, Angew. Chem. Int. Ed. 49 (1) (2010) 197–201. URL: http://dx.doi.org/10.1002/anie.200905131.
[158] L. Bertrand, L. Robinet, S.X. Cohen, C. Sandt, A.-S. Le Hô, B. Soulier, A. Lattuati-Derieux, J.-P. Echard, Identification of the finishing technique of an early eighteenth century musical instrument using FTIR spectromicroscopy, Anal. Bioanal. Chem. 399 (9) (2011) 3025–3032. URL: http://dx.doi.org/10.1007/s00216-010-4288-1.
[159] M. Lebon, K. Müller, J.-J. Bahain, F. Fröhlich, C. Falguères, L. Bertrand, C. Sandt, I. Reiche, Imaging fossil bone alterations at the microscale by SR-FTIR microspectroscopy, J. Anal. Atom. Spectrom. 26 (5) (2011) 922–929. URL: http://dx.doi.org/10.1039/c0ja00250j.

[160] I. Reiche, M. Lebon, C. Chadefaux, K. Müller, A.-S. Le Hô, M. Gensch, U. Schade, Microscale imaging of the preservation state of 5000-year-old archaeological bones by synchrotron infrared microspectroscopy, Anal. Bioanal. Chem. 397 (6) (2010) 2491–2499. URL: http://dx.doi.org/10.1007/s00216-010-3795-4.
[161] S.G. Kazarian, K.L.A. Chan, Micro- and macro-attenuated total reflection Fourier transform infrared spectroscopic imaging, Appl. Spectrosc. 64 (5) (2010) 135A–152A. URL http://as.osa.org/abstract.cfm?URI=as-64-5-135A.
[162] M. Spring, C. Ricci, D.A. Peggie, S.G. Kazarian, ATR-FTIR imaging for the analysis of organic materials in paint cross sections: case studies on paint samples from the National Gallery, London, Anal. Bioanal. Chem. 392 (1–2) (2008) 37–45.
[163] M.J. Nasse, M.J. Walsh, E.C. Mattson, R. Reininger, A. Kajdacsy-Balla, V. Macias, R. Bhargava, C.J. Hirschmugl, High-resolution Fourier-transform infrared chemical imaging with multiple synchrotron beams, Nat. Meth. 8 (2011) 413–416. URL: http://dx.doi.org/10.1038/nmeth.1585.
[164] M.J. Nasse, B. Bellehumeur, S. Ratti, C. Olivieri, D. Buschke, J. Squirrell, K. Eliceiri, B. Ogle, C. Schmidt Patterson, M. Giordano, C.J. Hirschmugl, Opportunities for multiple-beam synchrotron-based mid-infrared imaging at IRENI, Vib. Spectrosc. (in press), http://dx.doi.org/10.1016/j.vibspec.2011.11.016. URL: http://www.sciencedirect.com/science/article/pii/S0924203111001846.
[165] L. Strüder, S. Epp, D. Rolles, R. Hartmann, P. Holl, G. Lutz, H. Soltau, R. Eckart, C. Reich, K. Heinzinger, C. Thamm, A. Rudenko, F. Krasniqi, K.-U. Kühnel, C. Bauer, C.-D. Schröter, R. Moshammer, S. Techert, D. Miessner, M. Porro, O. Hälker, N. Meidinger, N. Kimmel, R. Andritschke, F. Schopper, G. Weidenspointner, A. Ziegler, D. Pietschner, S. Herrmann, U. Pietsch, A. Walenta, W. Leitenberger, C. Bostedt, T. Möller, D. Rupp, M. Adolph, H. Graafsma, H. Hirsemann, K. Gärtner, R. Richter, L. Foucar, R.L. Shoeman, I. Schlichting, J. Ullrich, Large-format, high-speed, X-ray pnCCDs combined with electron and ion imaging spectrometers in a multipurpose chamber for experiments at 4th generation light sources, Nucl. Instrum. Methods A 614 (3) (2010) 483–496. http://dx.doi.org/10.1016/j.nima.2009.12.053. URL: http://dx.doi.org/10.1016/j.nima.2009.12.053.
[166] S. Basolo, J.-F. Bérar, N. Boudet, P. Breugnon, B. Chantepie, J.C. Clémens, P. Delpierre, B. Dinkespiler, S. Hustache, K. Medjoubi, M. Ménouni, C. Morel, P. Pangaud, E. Vigeolas, A 20 kpixels CdTe photon-counting imager using XPAD chip, Nucl. Instrum. Methods A 589 (2) (2008) 268–274. http://dx.doi.org/10.1016/j.nima.2008.02.042. URL: http://www.sciencedirect.com/science/article/pii/S0168900208002234.
[167] L. Bertrand, P. Dillmann, M.G. Dowsett, A. Adriaens, Ancient and historical systems, in: H. Dosch, M.H. van de Voorde (Eds.), GENNESYS White Paper – A new European partnership between nanomaterials science & nanotechnology and synchrotron radiation and neutron facilities, Max Planck Gesellschaft, Stuttgart, Germany, 2009, pp. 241–245, ISBN 978-3-00-027338-4.
[168] A.P. Hitchcock, J.J. Dynes, G. Johansson, J. Wang, G. Botton, Comparison of NEXAFS microscopy and TEM-EELS for studies of soft matter, Micron 39 (2008) 311–319.
[169] A. Braun, F.E. Huggins, N. Shah, Y. Chen, S. Wirick, S.B. Mun, C. Jacobsen, G.P. Huffman, Advantages of soft X-ray absorption over TEM-EELS for solid carbon studies—a comparative study on diesel soot with EELS and NEXAFS, Carbon 43 (2005) 117–124.
[170] J. Wang, C. Morin, L. Li, A.P. Hitchcock, A. Scholl, A. Doran, Radiation damage in soft X-ray microscopy, J. Electron Spectrosc. Relat. Phenom. 170 (2009) 25–36.
[171] C. Jacobsen, S. Wirick, G. Flynn, C. Zimba, Soft X-ray spectroscopy from image sequences with sub-100 nm spatial resolution, J. Microsc. 197 (2) (2000) 173–184. URL: http://dx.doi.org/10.1046/j.1365-2818.2000.00640.x.
[172] P. Dumas, L. Miller, The use of synchrotron infrared microspectroscopy in biological and biomedical investigations, Vib. Spectrosc. 32 (2003) 3–21. URL: http://dx.doi.org/10.1016/S0924-2031(03)00043-2.
[173] V. Mazel, P. Richardin, D. Debois, D. Touboul, M. Cotte, A. Brunelle, P. Walter, O. Laprevote, Identification of Ritual Blood in African Artifacts Using TOF-SIMS and Synchrotron Radiation Microspectroscopies, Anal. Chem. 79 (24) (2007) 9253–9260. URL: http://dx.doi.org/10.1021/ac070993k.
[174] E. Levenson, P. Lerch, M.C. Martin, Infrared imaging: Synchrotrons vs. arrays, resolution vs. speed, Infrared Phys. Technol. 49 (2006) 45–52.
[175] E. Levenson, P. Lerch, M.C. Martin, Spatial resolution limits for synchrotron-based spectromicroscopy in the mid- and near-infrared, J. Synchrotron Radiat. 15 (2008) 323–328.
[176] V. Briois, D. Vantelon, F. Villain, B. Couzinet, A.-M. Flank, P. Lagarde, Combining two structural techniques on the micrometer scale: micro-XAS and micro-Raman spectroscopy, J. Synchrotron Radiat. 14 (5) (2007) 403–408. http://dx.doi.org/10.1107/S0909049507028683. URL: http://dx.doi.org/10.1107/S0909049507028683.
[177] R.J. Davies, M. Burghammer, C. Riekel, Simultaneous microRaman and synchrotron radiation microdiffraction: tools for materials characterization, Appl. Phys. Lett. 87 (26) (2005) 264105.
[178] M. Cotte, E. Checroun, V. Mazel, V.A. Solé, P. Richardin, Y. Taniguchi, P. Walter, J. Susini, Combination of FTIR and X-rays synchrotron-based micro-imaging techniques for the study of ancient paintings: a practical point of view, e-Preserv. Sci. 6 (2009) 1–9.
[179] V. Solé, E. Papillon, M. Cotte, P. Walter, J. Susini, A multiplatform code for the analysis of energy-dispersive X-ray fluorescence spectra, Spectrochim. Acta, Part B 62 (1) (2007) 63–68.
[180] A.J.L. Adam, P.C.M. Planken, S. Meloni, J. Dik, Terahertz imaging of hidden paint layers on canvas, Opt. Express 17 (5) (2009) 3407–3416. URL: http://www.opticsexpress.org/abstract.cfm?URI=oe-17-5-3407.
[181] L. Öhrström, A. Bitzer, M. Walther, F.J. Rühli, Technical note: Terahertz imaging of ancient mummies and bone, Am. J. Phys. Anthropol. 142 (3) (2010) 497–500. http://dx.doi.org/10.1002/ajpa.21292.
[182] R.V. Martins, V. Honkimäki, Depth resolved investigation of friction stir welds made from AA2024/AA2024 and AA2024/AA6082 using a spiral slit and high energy synchrotron radiation, Mater. Sci. Forum 490 (2005) 424–429.
[183] A. Hagen, H.F. Poulsen, T. Klemensø, R.V. Martins, V. Honkimäki, T. Buslaps, R. Feidenshans'l, A depth-resolved in-situ study of the reduction and oxidation of ni-based anodes in solid oxide fuel cells, Fuel Cells 6 (5) (2006) 361–366.
[184] T. Pradell, J. Molera, E. Pantos, A.D. Smith, C.M. Martin, A. Labrador, Temperature resolved reproduction of medieval luster, Appl. Phys. A 90 (2008) 81–88. URL: http://dx.doi.org/10.1007/s00339-007-4226-z.
[185] J. Lehmann, D. Salomon, J. Kinyangi, L. Dathe, S. Wirick, C. Jacobsen, Spatial complexity of soil organic matter forms at nanometre scales, Nature Geosci. 1 (2008) 238–242.
[186] P.J. Heaney, E.P. Vicenzi, L.A. Giannuzzi, K.J.T. Livi, Focused ion beam milling: A method of site-specific sample extraction for microanalysis of earth and planetary materials, Am. Mineral. 86 (9) (2001) 1094–1099. URL: http://ammin.geoscienceworld.org/cgi/content/abstract/86/9/1094.
[187] P. Sciau, P. Salles, C. Roucau, A. Mehta, G. Benassayag, Applications of focused ion beam for preparation of specimens of ancient ceramic for electron microscopy and synchrotron X-ray studies, Micron 40 (5–6) (2009) 597–604.
[188] R.J.H. Clark, R.R. Hark, N. Salvadó, S. Butí, T. Pradell, Spectroscopy study of mural paintings from the Pyrenean Church of Saint Eulàlia of Unha, J. Raman Spectrosc. 41 (11) (2010) 1418–1424. http://dx.doi.org/10.1002/jrs.2687. URL: http://dx.doi.org/10.1002/jrs.2687.
[189] H. Chapman, Phase-retrieval X-ray microscopy by Wigner-distribution deconvolution, Ultramicrosc. 66 (3) (1996) 153–172.
[190] G. Faigel, G. Bortel, C. Fadley, A. Simionovici, M. Tegze, Ten years of X-ray holography, X-ray Spectrom. 36 (1) (2007) 3–10.
[191] G. Faigel, M. Tegze, X-ray holography, Rep. Prog. Phys. 62 (1999) 355–393.
[192] J. Fienup, Phase retrieval algorithms: a comparison, Appl. Opt. 21 (15) (1982) 2758–2769.
[193] J. Miao, P. Charalambous, J. Kirz, D. Sayre, Extending the methodology of X-ray crystallography to allow imaging of micrometre-sized non-crystalline specimens, Nature 400 (6742) (1999) 342–344.
[194] J. Rodenburg, H. Faulkner, A phase retrieval algorithm for shifting illumination, Appl. Phys. Lett. 85 (2004) 4795.
[195] A. Schropp, P. Boye, J.M. Feldkamp, R. Hoppe, J. Patommel, D. Samberg, S. Stephan, K. Giewekemeyer, R.N. Wilke, T. Salditt, J. Gulden, A.P. Mancuso, I.A. Vartanyants, E. Weckert, S. Schöder, M. Burghammer, C.G. Schroer, Hard X-ray nanobeam characterization by coherent diffraction microscopy, Appl. Phys. Lett. 96 (9) (2010) 091102.
[196] M. Dierolf, P. Thibault, A. Menzel, C. Kewish, K. Jefimovs, I. Schlichting, K. König, O. Bunk, F. Pfeiffer, Ptychographic coherent diffractive imaging of weakly scattering specimens, New J. Phys. 12 (2010) 035017.

[197] M. Dierolf, A. Menzel, P. Thibault, P. Schneider, C.M. Kewish, R. Wepf, O. Bunk, F. Pfeiffer, Ptychographic X-ray computed tomography at the nanoscale, Nature 467 (7314) (2010) 436–439.
[198] A. Schropp, C. Schroer, Dose requirements for resolving a given feature in an object by coherent X-ray diffraction imaging, New J. Phys. 12 (2010) 035016.
[199] E. Garman, S. McSweeney, Progress in research into radiation damage in cryo-cooled macromolecular crystals, J. Synchrotron Radiat. 14 (1) (2006) 1–3.
[200] F. Messina, S. Agnello, M. Cannas, A. Parlato, Room temperature instability of $E'_\gamma$ centers induced by $\gamma$ irradiation in amorphous $SiO_2$, J. Phys. Chem. A 113 (6) (2008) 1026–1032.
[201] P. Levy, Radiation damage studies on non-metals utilizing measurements made during irradiation, J. Phys. Chem. Solids 52 (1) (1991) 319–349.
[202] C.F. Horton, G.D. Richards, T.D. White, A. Macdowell, R.S. Jabbour, J. Nasiatka, Color centers induced in dental enamel during synchrotron microcomputed tomography: Phase I assessment, Am. J. Phys. Anthrop. 141 (S50) (2010) 131. URL: http://dx.doi.org/10.1002/ajpa.21276.
[203] L. Bertrand, D. Vantelon, E. Pantos, Novel interface for cultural heritage at SOLEIL, Appl. Phys. A 83 (2) (2006) 225–228. URL: http://dx.doi.org/10.1007/s00339-006-3514-3.